Ulm University Medical Center
Department of Nuclear Medicine
Head: Professor Dr. med. Ambros J. Beer

Optimization of imaging and therapy for a radioligand targeting the prostate-specific membrane antigen using a physiologically-based pharmacokinetic model

Cumulative dissertation submitted to obtain the doctoral degree of
Human Biology of the Medical Faculty of
Ulm University

M.Sc. Nusrat Jihan Begum
from Pekanbaru, Indonesia
2022

Acting Dean	:	Professor Dr. rer. nat. Thomas Wirth
First Reviewer	:	Professor Dr. rer. nat. Gerhard Glatting
Second Reviewer	:	Professor Dr. rer. nat. Volker Rasche

Date of Graduation : July 8, 2022

Table of contents

Abbreviations ..... **IV**

1 Introduction **1**

1.1 Treatment planning for radionuclide therapy 1

1.1.1 Dosimetry-based individualized treatment planning 2

1.1.2 Radiobiology 5

1.1.3 Theranostics 6

1.1.4 Physiologically-based pharmacokinetic/pharmacodynamic models 7

1.2 Motivation and aims 9

1.3 List of included articles 9

2 Published articles **10**

2.1 The effect of total tumor volume on the biologically effective dose 10

2.1.1 Summary 10

2.1.2 Copyright and own contributions 13

2.1.3 Original paper 14

2.2 The effect of ligand amount, affinity, and internalization on imaging and therapy 19

2.2.1 Summary 19

2.2.2 Copyright and own contributions 23

2.2.3 Original paper 24

2.3 The effect of the radionuclide half-life on PET/CT imaging 32

2.3.1 Summary 32

2.3.2 Copyright and own contributions 34

2.3.3 Original paper 35

3 Discussion **40**

4 Abstract **45**

5 References **47**

Appendix **53**

A.1 Supplementary material 1 53

A.2 Supplementary material 2 94

Acknowledgments **112**

Curriculum Vitae **113**

Abbreviations

ADME	Administration, distribution, metabolism, and excretion
AUC	Area under the curve
BED	Biologically effective dose
CT	Computed tomography
GI	Gastrointestinal tract
mCRPC	Metastatic castration-resistant prostate cancer
MIRD	Medical Internal Radiation Dose
OAR	Organ at risk
p.i.	Post injection
PBPK	Physiologically-based pharmacokinetic
PET	Positron emission tomography
PopKinetic	Population kinetic software
PRRT	Peptide-receptor radionuclide therapy
PSMA	Prostate-specific membrane antigen
RLT	Radioligand therapy
RM	Red marrow
SAAM II	Simulation, analysis, and modeling II software
SE	Standard error
SPECT	Single-photon emission computerized tomography
TAC	Time-activity curve
TIAC	Time-integrated activity coefficient
TTV	Total tumor volume

1 Introduction

Prostate cancer is one of the most common cancers and the leading cause of cancer-related deaths in men worldwide [1]. In the early stages, prostate cancer is initially confined to the prostate gland in patients. It can usually be treated with conventional therapies such as surgery and radiotherapy (e.g., external beam radiotherapy). If the prostate cancer has already metastasized, systemic treatments such as androgen deprivation therapy, chemotherapy, or a combination of these therapies are typical initial treatment options. Despite the initial response to these systemic treatments, many patients eventually develop metastatic castration-resistant cancer (mCRPC), a lethal form of advanced prostate cancer. The prognosis and treatment of mCRPC remain poor. Therefore, efforts to explore alternative therapeutic approaches for mCRPC are urgently needed.

Radioligand therapy (RLT) is a part of molecular radiotherapy or radionuclide therapy. In RLT, radiation is delivered to the patient by administering a radiolabeled ligand (radioligand), usually intravenously. The radioligand targets specific molecules or receptors on the surface of the cancer cells. Prostate-specific membrane antigen (PSMA) is a type II transmembrane glycoprotein receptor that is overexpressed in most prostate cancers [2]. Its expression is even stronger in advanced stages, making it an attractive target for RLT in mCRPC. However, despite its name, PSMA expression is not specific only to the prostate, as PSMA is also found at low levels in normal tissues such as salivary glands, proximal tubule cells in the kidney, and small intestine [3]. Therefore, treatment should be well planned to achieve an optimal therapeutic effect on the tumor with tolerable toxicity to normal tissues. Treatment planning in radionuclide therapy includes determining the therapeutic activity to be administered for each patient [4].

1.1 Treatment planning for radionuclide therapy

Treatment planning can be either cohort-based or patient-based [4]. In cohort-based treatment planning, the administered activity per mass of body weight or surface area is reported in chemotherapy or calculated based on a dose or activity escalation study for a specific patient group, neglecting inter-patient variability [4]. Despite the significant pharmacokinetic differences between patients, standardized administered activity (cohort-based) is often used [5-7]. For example, in patients with a high tumor burden, no effective therapeutic effect would be achieved if the standard amount of injected activity and peptides were administered [8, 9].

Patient-specific treatment planning takes into account the biokinetics of the individual patient (obtained by quantitative imaging, e.g., SPECT/CT or planar scintigraphy) to determine the prescribed activity for therapy. Internal dosimetry, a technique for calculating the absorbed dose of a radioligand in the tumor and organs of an individual patient, is essential for patient-specific treatment planning [4, 10-12]. Although this requires more resources and time, incorporating patient-specific dosimetry (Section 1.1.1) and radiobiological information (Section 1.1.2) into treatment planning can reduce the risk of over-or under-treatment and thus optimize therapy for individual patients [13-17].

1.1.1 Dosimetry-based individualized treatment planning

Accurate and precise individual dosimetry is critical for individualized treatment planning to improve patient safety and therapeutic efficacy [18]. Internal dosimetry aims to increase the dose absorbed in tumor cells without exceeding the recommended limits for absorbed dose in organs at risk (OARs) [4].

The basic methodology for internal dosimetry was developed by the Medical Internal Radiation Dose (MIRD) Committee [19] and is described by the following equation:

$$D_t = \sum_s \tilde{A}_s \cdot S_{t \leftarrow s} = A_0 \cdot \sum_s \tilde{a}_s \cdot S_{t \leftarrow s}\,, \tag{1}$$

where

- D_t is the mean absorbed dose to a target organ *t* delivered by the cumulated activity in the source organs *s*.
- $\tilde{A}_s$ is the total number of radioactive decays in the source organ *s*, denoted as time-integrated activity, is calculated as the area under the curve (AUC).
- A_0 is the administered activity.
- $\tilde{a}_s$ are the time-integrated activity coefficients (TIACs) or formerly referred to as the residence times of the source organ *s* (equation (2)).
- $S_{t \leftarrow s}$ are the S-values or the radionuclide-specific quantity representing the mean absorbed dose to target organ *t* per radioactive decay in the source organ *s* (equation (3)).

The TIACs $\tilde{a}_s$ describe the time-integrated activities, i.e., the total number of radioactive decays $\tilde{A}_s$ per unit of administered activity A_0 is calculated as follows:

$$\tilde{a}_s = \frac{\tilde{A}_s}{A_0} = \frac{1}{A_0}\int_0^{\infty} A_s(t)\, dt\,, \tag{2}$$

where $A_s(t)$ is the activity within the source organ *s* at time t. The total number of radioactive decays $\tilde{A}_s$ is determined by integrating the time-activity curve (TAC) A_s from 0 to infinity equation (2).

Several steps are required to calculate the individual absorbed dose in organs.

The first step is quantitative imaging at several time points after administration of the radiopharmaceutical to determine the activity in the organs of interest over time $A_s(t)$. Quantitative imaging for dosimetry can be performed by serial planar gamma-camera scans and/or tomographic measurements, e.g., single-photon emission computed tomography (SPECT) or positron emission tomography (PET) [4]. However, fully planar dosimetry tends to overestimate renal dose compared with SPECT-based methods, e.g., due to activity overlap with surrounding tissue [20]. Quantitative accuracy requires precise calibration and careful adjustment of camera and reconstruction settings. Activity quantification with 3D tomographic imaging modalities increases quantitative accuracy compared with planar images [21, 22]. Organ or tumor dosimetry requires the determination of individual organ or lesion volumes, e.g., by CT. The use of standard organ volumes may lead to a significant under-or overestimation of the absorbed dose [23, 24]. SPECT/CT in combination with whole-body and red marrow information from planar images [25-27] increases dosimetry accuracy.

The second step is to generate the TAC $A_s(t)$ for organs and tumor lesions to obtain the total number of decays occurring in the initial organs *s*. The TAC $A_s(t)$ generated for each organ and tumor can be fitted with a mathematical model, e.g., represented by a sum of exponential functions [28], to estimate the TIACs $\tilde{a}_s$. The shape of the fitted curve can be strongly influenced by the number and timing of the activity measurement. Therefore, it is important to select the optimal time points [27, 29-31] and the optimal fitting function [32]. The selection of the optimal time points depends, for example, on the biokinetics. Therefore, the choice affects the accuracy of the determined TIACs $\tilde{a}_s$.

The final step is the selection of the S-value $S_{t\leftarrow s}$. The S-value $S_{t\leftarrow s}$ considers the energy released during each radioactive decay and the anatomy of the patient or the relative geometry of the organ (equation (3)) [19]. Thus, cumulative activity is determined by biological characteristics, whereas the S-factor considers the physical components of the absorbed dose:

$$S_{t\leftarrow s} = \frac{1}{M_t}\sum_i E_i \cdot Y_i \cdot \Phi_{t\leftarrow s}\,(E_i), \tag{3}$$

where M_t denotes the mass of the target organ *t*, E_i is the mean radiation energy of the ith transition and Y_i is the fraction of the ith transition per nuclear transformation, and $\Phi_{t\leftarrow s}\,(E_i)$ is the absorbed dose fraction in the target organ *t* delivered by the source organ *s* per decay.

The calculation of the S-value strongly depends on the chosen model, e.g., analytical phantoms or voxel-based phantoms. If analytical phantoms or mathematical anthropomorphic are used, organ masses should be corrected to patient organ weights. For patient-specific dose estimates, voxel-based S-values are often used. Voxel-based phantoms provide the ability to create more detailed models of anatomy. The NUKDOS software is an example of a calculation that uses voxel-based S-values [33]. S-values have already been calculated using Monte Carlo simulations for various therapeutically relevant radionuclides, and pairs of reference organ phantoms (e.g., female and male adults) and are already implemented in dedicated software packages [18, 33-38].

It is assumed that the activity distribution within the source and target organs is homogeneous and that only self-dose is to be considered because of the short range of the emitted particles. Therefore, equation (1) can be simplified to

$$D_{self,t} = \tilde{A}_t \cdot S_{t\leftarrow t} = A_0 \cdot \tilde{a}_t \cdot S_{t\leftarrow t}\,, \tag{4}$$

Absorbed dose-response models for deterministic effects should be used for treatment planning. Several studies in radiation oncology have demonstrated a relationship between absorbed dose to radiation and tissue toxicity or tumor response. Therefore, the maximum tolerable absorbed dose is often used in molecular radiotherapy, assuming an equivalent biological effect to radiotherapy. However, in contrast to external irradiation in radiotherapy, internal irradiation in molecular radiotherapy delivers lower absorbed dose rates. It continuously irradiates cells and organs with a constantly changing absorbed dose rate, allowing cell damage to be repaired during therapy, affecting the biological response. These differences can be accounted for, for example, by applying the concept of biologically effective dose (BED), which is based on a linear-quadratic model (parameters α and β) and the constant μ for sublethal damage repair.

1.1.2 Radiobiology

BED was proposed to allow comparison of therapies with different dose rates and fractionation systems, e.g., the targeted radionuclide treatment with external beam treatments [39-41]:

$$BED_t = D_t \cdot RE_t , \tag{5}$$

where BED_t is the biologically effective dose for the absorbed dose to the target organ *t*, D_t is the mean absorbed dose to the target organ *t* and RE_t is the relative effectiveness, which considers repairing sublethal damage during therapy.

$$RE(D_t) = 1 + \frac{G}{\alpha/\beta} \cdot D_t , \tag{6}$$

where G is the Lea–Catcheside factor [42]. The biologically effective dose BED_t of the target organ *t* is thus calculated according to

$$BED_t = D_t \cdot (1 + \frac{G}{\alpha/\beta} \cdot D_t), \tag{7}$$

Assuming a monoexponential decay of dose rate, G can be written as follows:

$$G = \frac{\lambda}{\lambda + \mu}, \tag{8}$$

with

$$\lambda = \frac{\ln(2)}{t_{1/2}}, \tag{9}$$

where λ is the effective rate in the organ of interest, $t_{1/2}$ is the effective half-life, and μ is the rate of sublethal damage repair (assuming an exponential repair rate).

The α and β parameters in equations (6) and (7) are tissue-specific constants that indicate cell survival curves, such as for prostate tumors α/β = 1.49 Gy [43] and a repair half-life μ of

1.9 h [43] from radiotherapy and brachytherapy. The linear-quadratic model is commonly used to represent cell survival after ionizing radiation exposure [41]:

$$F_s = \exp(-\alpha \cdot D - \beta \cdot D^2), \quad (10)$$

where F_s is the cell survival fraction, D is the absorbed dose, α describes lethal cell damage that requires only one sublethal event, and β describes lethal cell damage that requires two sublethal events [39].

The α/β ratio describes the absorbed dose for which the cell-killing represented by the linear and quadratic parts of equation (10) are equal. For therapies with more than one therapy cycle, the BEDs can be summed, given that there is no activity left and the sublethal damage is repaired between the cycles.

In addition to dosimetry and radiobiology, theranostics in treatment planning can further improve and optimize the prediction of treatment outcomes for individual patients, enabling more individualized treatments [44].

1.1.3 Theranostics

Theranostics or theragnostics, composed of the words therapy or therapeutic and diagnostics, refers to the close relationship between diagnostics and treatment. Information from imaging is used to determine the optimal therapeutic regimen for an individual patient [45]. Molecular imaging can detect metastases, localize tumors, select patients eligible for RLT, and monitor response to treatment. In nuclear medicine, theranostics in RLT refers to tracers to predict the absorbed dose in therapy. The biodistribution of diagnostic and therapeutic agents should be similar to predict the absorbed dose during treatment accurately. Thus, the same ligand or a very identical ligand labeled with different radionuclides (γ-emitter for imaging and β- or α-emitter for therapy) is usually used to avoid different pharmacokinetics between imaging and therapy.

Theranostics treatment planning requires careful consideration of radionuclide selection, ligand properties, injected activity, and ligand amount for both imaging and therapy. The choice can be challenging because radioligands must be optimized for both imaging and treatment, and different measures are of interest (activity concentration for imaging and absorbed dose for therapy) [45].

1.1.4 Physiologically-based pharmacokinetic/pharmacodynamic models

Treatment planning should accurately predict individual biodistribution of the radiopharmaceutical to ensure patient safety and treatment efficacy. Computational approaches using mathematical models are essential tools for developing precise and individualized treatments that are both cost- and time-efficient [46]. TIACs can also be estimated by compartmental modeling. Physiologically-based pharmacokinetic (PBPK) models describe the behavior of radiolabeled compounds based on vital physiological processes, i.e., administration, distribution, metabolism, and excretion (ADME) [47]. PBPK models are best suited for the systematic and quantitative study of key pharmacokinetic parameters. They account for and describe physiological processes in the tumor and the individual patient's organs [16, 48-50].

In this thesis, a whole-body PBPK model for PSMA radioligand therapy initially developed by Kletting et al. [16] was improved, e.g., including tumors growth between PET/CT imaging and therapy and the assignment data to the specific compartments. The global structure of the whole-body PBPK model is shown in Fig. 1. The model was implemented using dedicated software, such as Simulation, Analysis, and Modeling II (SAAM II) [51] and MATLAB®-based tools (Simulink and SimBiology) [52]. The PSMA-positive tissues in the model are tumors, kidneys, liver, and gastrointestinal tract. The different organs are interconnected via the blood circulatory system. Each organ consists of subcompartments to account for all relevant physical and physiological mechanisms such as blood flow, specific binding of radioligands to surface receptors, internalization, degradation, release, and physical decay [16, 48-50]. The pharmacokinetics of labeled and unlabeled ligands were modeled separately, assuming the same physiological parameters and linked by physical decay. General physiological parameters (e.g., radioligand properties) were taken from the literature and cell studies [53] to reduce the number of unknown parameters. Physical information of the individual patient, e.g., weight and measured organ masses, was included in the whole-body PBPK model. Other important pharmacokinetic parameters (e.g., perfusion or blood flow density and receptor density) were fitted to the time-activity data of the patients in a Bayesian framework with mean and standard deviation obtained from population studies. The remaining individual unknown parameters of the PBPK model were fitted to time-activity data of the relevant organs obtained, for example, from planar scintigraphy, SPECT, or PET images. The fitted PBPK model (i.e., the model and the individual parameters) define a virtual patient. The virtual patient can be utilized to predict and analyze the biodistribution of various radioligands by simply changing the relevant specific parameters within the PBPK model, e.g., radionuclide

and ligand properties [54-58]. Internal individual dosimetry, i.e., calculation of absorbed and biologically effective doses (BED), is integrated into the PBPK model.

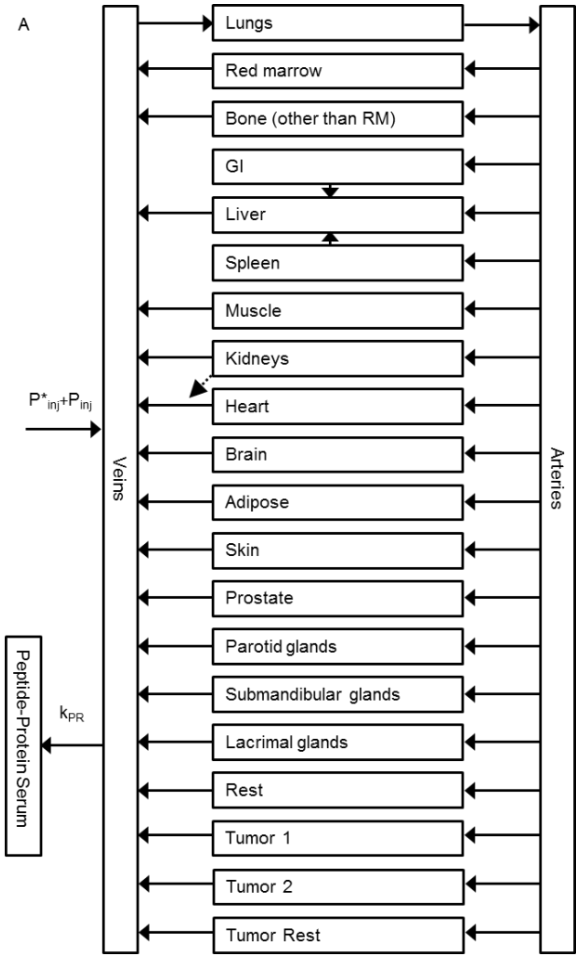

Fig. 1. Global structure of a whole-body physiologically-based pharmacokinetic (PBPK) model. (RM: red marrow; GI: gastrointestinal tract; k_{PR}: Binding rate of a peptide to serum proteins).
Original figure from the supplemental material published in P. Kletting et al. PloS One 2016;11(9):e0162303. DOI:10.1371/journal.pone.0162303. Adapted from Ref. [16], CC BY 4.0, https://creativecommons.org/licenses/by/4.0/

1.2 Motivation and aims

Although PSMA-targeted RLT is a promising treatment alternative for mCRPC, many patients still do not benefit optimally from this therapy. Efforts need to be made to optimize imaging and therapy of PSMA-targeted RLT, which may depend on the ligand properties, e.g., affinity and internalization, the radionuclide, e.g., half-life, measurement time points after injection, the amount of activity and ligand to be administered. In addition, inter-patient pharmacokinetic variability must be considered as it affects biodistribution in the patient, e.g., total tumor volume (TTV). Therefore, the objectives of the thesis were to systematically and quantitatively investigate the impact of a *priori* knowledge for optimizing PSMA imaging and therapy *in silico* (computationally). For this purpose, PBPK models are the most appropriate because they take into account a *priori* knowledge of human physiology and anatomy and allow the simulation and analysis of the biodistribution of the individual patient. The studies include the investigation of:

1. The effect of TTV on BEDs of tumors and OARs (the activity and amount of ligands to be administered leading to an optimal tumor-to-kidneys ratio were also investigated).
2. The effect of ligand amounts, affinities, and internalization on imaging and therapy.
3. The effect of radionuclide half-lives, ligand affinities, and measurement time points after injection on tumor and background activity concentrations.

1.3 List of included articles

Begum NJ, Thieme A, Eberhardt N, Tauber R, D'Alessandria C, Beer AJ, Glatting G, Eiber M, Kletting P. The Effect of Total Tumor Volume on the Biologically Effective Dose to Tumor and Kidneys for ^{177}Lu-Labeled PSMA Peptides. J Nucl Med. 2018;59(6):929-933. DOI: 10.2967/jnumed.117.203505; Ref . [59]

Begum NJ, Glatting G, Wester HJ, Eiber M, Beer AJ, Kletting P. The effect of ligand amount, affinity and internalization on PSMA-targeted imaging and therapy: A simulation study using a PBPK model. Sci Rep. 2019;9(1):20041. DOI: 10.1038/s41598-019-56603-8; Ref. [60]

Begum NJ, Glatting G, Eiber M, Beer AJ, Kletting P. An in silico study on the effect of the radionuclide half-life on PET/CT imaging with PSMA-targeting radioligands. Nuklearmedizin. 2021;60(1):33-37. DOI: 10.1055/a-1253-1535; Ref. [61]

2 Published articles

2.1 The effect of total tumor volume on the biologically effective dose

2.1.1 Summary

PSMA-targeted RLT is a promising treatment option for mCRPC [62-65]. A fixed or empirical amount of administered activity is often used. However, many patients still do not benefit optimally from this therapy. The significant pharmacokinetic differences between patients (e.g., tumor volume and renal function) may compromise therapeutic efficacy. For example, when a typical amount of activity and ligand is administered to patients with a large tumor volume, the dose absorbed by the tumor may be insufficient due to the sink effect [8, 66]. Considering the high variability between patients when determining the activity to be administered for an individual patient may improve RLT. This article [59] systematically and quantitatively investigated the effects of different TTVs and different amounts of administered activity and ligand on BED for tumors and OARs. For this purpose, PBPK models are best suited to study important parameters because they take into account the physiology of tumors and OARs of a single patient.

The study included 13 patients (age 70 ± 6 years) with mCRPC (median prostate-specific antigen of 133 ng/L (range 0.23-2.905 ng/L)) treated with ^{177}Lu-PSMA I&T in the first cycle [62]. The Institutional Review Board of the Technical University of Munich approved the retrospective analysis (approval 115/18 S). Informed written consent was obtained from all patients. Patients were administered a mean activity of (7.3 ± 0.3) GBq ^{177}Lu- PSMA I&T with a ligand amount of (91 ± 5) nmol. Planar whole-body gamma camera scans were performed 30-120 min, 24 h, 168 h p.i. In some patients, an additional 48 h and 72 h p.i. Inclusion criteria were at least three planar whole-body scintigraphies, including one late scintigraphy (6-8 days p.i.). Amino acids were administered to block non-specific uptake. Before therapy, a mean activity of (115 ± 16) MBq ^{68}Ga- PSMA-11 with a ligand amount of (1.6 ± 0.3) nmol was administered. PET/CT was performed to determine the volume and activity concentration of the tumor lesions, kidneys, salivary glands, and lacrimal glands. Two tumor lesions were selected based on high uptake and no significant overlap with other PSMA-positive tissues. The other tumor lesions were grouped in the model as tumor REST.

To investigate the effect of TTV on BED, a whole-body PBPK model for PSMA-specific ligands originally developed by Kletting et al. [16] was improved. The general structure

of the whole-body PBPK model has already been described in Section 1.1.4. The PBPK model was fitted to the biokinetic data of 13 patients. The PBPK model with the estimated individual parameters (virtual patients) was used for simulation. The BED for each tumor lesion and the OARs were calculated using equation (7) in Section 1.1.2. For the simulations, the PBPK model and the method for calculating BED were implemented in MATLAB®/Simulink, version 2015b (The MathWorks, Inc., Natick, Massachusetts, United States). The goodness of fit was determined based on visual inspection of the graphs, standard error (SE) of the fitted parameters, and coefficient of determination [32]. The PET/CT information and PBPK model were also used to correct for overlapping non-tumor tissue activity on the planar images. A correction factor was introduced and estimated when fitting the PBPK model to correct the over-or underestimation of tumor volume. All detailed information about the PBPK model and the patient used can be found in the supplementary reference material [59], also included in Appendix A.1.

Based on the fitted parameters, pharmacokinetics were simulated for 1) a TTV (i.e., the volume of tumor REST plus the two tumor lesions) of 0.1, 0.3, 1, 3, and 10 L and 2) different combinations of ligand amount (2-2^{10} nmol). The limit of tolerable dose for the kidneys was assumed to be 5 $Gy_{2.5}$, allowing multiple cycles, e.g., 8 with a maximum cumulative dose of 40 $Gy_{2.5}$ for a patient without additional risk factors. BEDs were determined for two tumor lesions, tumor REST, salivary glands, and kidneys. The BED ratio of the tumor to the kidney was also calculated. Mean values were determined for all patients and patients with a TTV of 0.3-3 L. The dosimetry models for the salivary glands and bone marrow (especially for heavily metastasized bone and diffuse infiltration of the red marrow) contain significant uncertainties. Despite the known uncertainties, simulations were performed for these organs to see the potential impact of TTV on the BED of the red marrow and salivary glands.

Tumor parameters were broadly distributed, e.g., total tumor volume of 0.02-5 L (median: 0.4 L), receptor densities of 4-124 nmol/L (median: 50 nmol/L), blood flow of 0.02-1.6 mL/min/g (median: 0.2 mL/min/g). Simulated BEDs decreased by 58.2% for tumor lesions and 58.4% for kidneys when TTV was increased from 0.3 to 3 L. For all patients, the change in BED ratio between tumor and kidney was a maximum of 12% with standard ligand amounts and activities. An increase in TTV from 0.3 to 3 l also resulted in BED changes in the submandibular glands (59%), parotid glands (59%), and red bone marrow (185%). At a TTV of 10 L, the average BED for the bone marrow increased to 0.39 Gy_{15}. Patients with a high tumor load (>0.3 L) could be administered higher activities (10.4 ± 4.4 GBq) and ligand amounts (273 ± 136 nmol) without exceeding the tolerable BED for the kidneys.

It can be concluded that tumor burden significantly affects BEDs for tumors and OARs. Based on the results, higher activities and peptide amounts could be safely administered to patients with a large PSMA ligand-positive tumor mass to maximize tumor BEDs without exceeding critical absorbed doses for OARs.

2.1.2 Copyright and own contributions

This article [59] is published as

> **Begum NJ**, Thieme A, Eberhardt N, Tauber R, D'Alessandria C, Beer AJ, Glatting G, Eiber M, Kletting P. The Effect of Total Tumor Volume on the Biologically Effective Dose to Tumor and Kidneys for ^{177}Lu-Labeled PSMA Peptides. J Nucl Med. 2018;59(6):929-933. DOI: 10.2967/jnumed.117.203505.

The supplemental material of this publication is provided in appendix A.1 and available online at https://jnm.snmjournals.org/content/59/6/929/tab-supplemental.

Copyright

Copyright © 2018 by the Society of Nuclear Medicine and Molecular Imaging.

Reprinted (whole article) with permission.

Own contributions:

I contributed to the conception and design of the study. I developed and implemented the MATLAB®/Simulink script (version 2015b) and the PBPK model for the total tumor volume simulations and the BED calculation. I performed the data analyses and graphical representation of the results. I wrote, edited, and reviewed the manuscript with all co-authors.

The Effect of Total Tumor Volume on the Biologically Effective Dose to Tumor and Kidneys for ^{177}Lu-Labeled PSMA Peptides

Nusrat J. Begum*[1], Anne Thieme*[2], Nina Eberhardt[2], Robert Tauber[3], Calogero D'Alessandria[2], Ambros J. Beer[1], Gerhard Glatting[1], Matthias Eiber†[2], and Peter Kletting†[1]

[1]*Department of Nuclear Medicine, Universität Ulm, Ulm, Germany;* [2]*Department of Nuclear Medicine, Klinikum Rechts der Isar, Technische Universität München, Munich, Germany; and* [3]*Department of Urology, Klinikum Rechts der Isar, Technische Universität München, Munich, Germany*

The aim of this work was to simulate the effect of prostate-specific membrane antigen (PSMA)–positive total tumor volume (TTV) on the biologically effective doses (BEDs) to tumors and organs at risk in patients with metastatic castration-resistant prostate cancer who are undergoing ^{177}Lu-PSMA radioligand therapy. **Methods:** A physiologically based pharmacokinetic model was fitted to the data of 13 patients treated with ^{177}Lu-PSMA I&T (a PSMA inhibitor for imaging and therapy). The tumor, kidney, and salivary gland BEDs were simulated for TTVs of 0.1–10 L. The activity and peptide amounts leading to an optimal tumor-to-kidneys BED ratio were also investigated. **Results:** When the TTV was increased from 0.3 to 3 L, the simulated BEDs to tumors, kidneys, parotid glands, and submandibular glands decreased from 22 ± 15 to 11.0 ± 6.0 $Gy_{1.49}$, 6.5 ± 2.3 to 3.7 ± 1.4 $Gy_{2.5}$, 11.0 ± 2.7 to 6.4 ± 1.9 $Gy_{4.5}$, and 10.9 ± 2.7 to 6.3 ± 1.9 $Gy_{4.5}$, respectively (where the subscripts denote that an α/β of 1.49, 2.5, or 4.5 Gy was used to calculate the BED). The BED to the red marrow increased from 0.17 ± 0.05 to 0.32 ± 0.11 Gy_{15}. For patients with a TTV of more than 0.3 L, the optimal amount of peptide was 273 ± 136 nmol and the optimal activity was 10.4 ± 4.4 GBq. **Conclusion:** This simulation study suggests that in patients with large PSMA-positive tumor volumes, higher activities and peptide amounts can be safely administered to maximize tumor BEDs without exceeding the tolerable BED to the organs at risk.

Key Words: prostate-specific membrane antigen (PSMA); biologically effective dose (BED); total tumor volume (TTV); physiologically based pharmacokinetic (PBPK) modeling

J Nucl Med 2018; 59:929–933
DOI: 10.2967/jnumed.117.203505

Radioligand therapy (RLT) using radiolabeled prostate-specific membrane antigen (PSMA)–specific peptides has been proven to be a safe, effective, and thus promising method for the treatment of metastatic castration-resistant prostate cancer (*1–4*). A one-activity-fits-all approach is widely used. However, RLT might be improved by considering the high interpatient pharmacokinetic variability reported in several dosimetry studies (*5–8*). In RLT with somatostatin receptor type 2–specific peptides, it has been shown that tumor burden, body size, and renal function significantly affect the activity concentration in organs at risk (OARs) and tumor tissue (*9*). However, so far, in patients with metastatic castration-resistant prostate cancer, a standard activity and peptide amount is usually injected, although the tumor burden varies considerably (from milliliters to several liters). In a recent study, it was shown that large tumor loads lead to a considerably lower SUV_{mean} in dose-limiting organs (*10*). Therefore, the biologically effective doses (BEDs) to normal tissues and tumor tissue might also vary considerably (*9*). For example, large tumor burdens most presumably lead to a less effective treatment when a standard activity and amount of peptide are used (*9*). Physiologically based pharmacokinetic (PBPK) models are most suitable to systematically and quantitatively investigate important pharmacokinetic parameters, because they take into account the individual patient physiology of the OARs and the pathophysiology of the tumor (*8,11,12*).

The aims of this study were to quantitatively investigate, for ^{177}Lu-labeled PSMA-specific peptides, the effects of different total tumor volumes (TTVs) and varying activities and peptide amounts on the BEDs to tumors and OARs. Therefore, the parameters of a recently developed PBPK model (*8*) were simultaneously fitted to the PET/CT and planar imaging data of 13 patients treated with RLT with ^{177}Lu-PSMA I&T (*1*). On the basis of the estimated parameters, simulations were conducted for a range of tumor volumes (0.1–10 L) and different peptide amounts and activities.

MATERIALS AND METHODS

Patients and Therapeutic Measurements

The data of 13 patients with metastatic castration-resistant prostate cancer treated with ^{177}Lu-PSMA I&T RLT were included (Table 1 and Supplemental Table B1; supplemental materials are available at http://jnm.snmjournals.org). These patients were also part of a recently published study (*1*). The inclusion criteria were at least 3 whole-body planar scintigraphs, including 1 late scintigraph (6–8 d after injection) (Supplemental Table B2). Only the first cycle of RLT was used. The patients received an average (±SD) of 91 ± 5.0 nmol of ^{177}Lu-PSMA I&T labeled with 7.3 ± 0.34 GBq of ^{177}Lu (*1*). Amino acids were coinfused as applied in peptide receptor radionuclide therapy. Quantification

Received Oct. 10, 2017; revision accepted Jan. 20, 2018.
For correspondence or reprints contact: Peter Kletting, Klinik für Nuklearmedizin, Universität Ulm, D-89081 Ulm, Germany.
E-mail: peter.kletting@uniklinik-ulm.de
*Contributed equally to this work.
†Contributed equally to this work.
Published online Feb. 1, 2018.
COPYRIGHT © 2018 by the Society of Nuclear Medicine and Molecular Imaging.

TABLE 1
Patient Data

Patient no.	Age (y)	BSA (m^2)	PSA (ng/L)	Measured volumes (mL)					
				Kidneys	SM glands	Parotid glands	Tumor lesion 1	Tumor lesion 2	Tumor REST
1	66	2.0	513	372	17	39	9.4	19	201
2	75	1.8	49	273	17	46	2.1	4.2	130
3	72	2.0	31	304	13	43	14	52	156
4	66	1.9	97	282	14	26	14	31	370
5	74	1.9	47	281	19	44	26	17	686
6	58	2.2	2,905	400	13	36	81	92	5,620
7	64	1.9	0.23	278	16	21	48	37	17
8	73	2.0	1,193	233	18	45	5.7	19	429
9	77	1.8	2,547	256	12	41	15	8.7	1,481
10	63	2.0	2,471	392	13	40	1.9	5.3	252
11	73	1.8	7	305	21	39	0.33	1.2	10
12	74	2.0	161	297	13	59	9.9	8.7	217
13	74	2.1	133	348	13	48	6.1	2.0	17
Mean	70	2.0	781	309	15.2	40.6	18	23	737
SD	5.8	0.1	1,112	53	3.0	9.7	23	26	1,519

BSA = body surface area; PSA = prostate-specific antigen; SM = submandibular.

was performed as previously described (*1*). The time–activity data of the kidneys, 2 tumor lesions showing no significant overlap with other PSMA-ligand–positive tissues, and the total body were used, and the activities in underlying tissue (muscle and adipose) were corrected within the PBPK model (Supplemental Eq. B1). The institutional review board of the Technische Universität München approved the compassionate use of ^{177}Lu-PSMA I&T in metastatic castration-resistant prostate cancer patients who had no other therapeutic options. All subjects signed a written informed consent form.

Pretherapy Measurements

The ^{68}Ga-PSMA HBED-CC (1.6 ± 0.3 nmol labeled with 115 ± 16 MBq) PET/CT images before therapy (1–9 wk) were used to determine the volumes for tumors, kidneys, salivary glands, and lacrimal glands (*1*) with SyngoVia (Siemens Healthcare). TrueD (Siemens Healthcare) was used to estimate the activity concentration. Correction for background activity in the tumor lesion region of interest was performed (Supplemental Eq. B2). To estimate the volume of a single tumor lesion, the volume of interest was defined with an isocontour of 20%–50% of SUV_{max}, with adjustment of the volume of interest to the anatomic configuration of the lesion based on the CT scan (*1*). The cumulated activity and volume of all tumor lesions other than lesions 1 and 2 were obtained by adding all lesions slice by slice using isocontours of 15%–20%. This cumulated volume, which consisted of hundreds of lesions, is given the term *tumor REST* here. For this tumor REST mass, CT was not used. In PBPK models, measured data can be linked to several compartments (Supplemental Eqs. B1–B4). The PET/CT data of the kidney and the 2 tumor lesions were corrected for background using 2 different volumes of interest (Supplemental Eqs. B2 and B4). The PET/CT data of the tumor REST were assigned to the pertaining compartments, with a correction factor considering potential over- or underestimation (Supplemental Eq. B3; Supplemental Table C1).

Therefore, to correct for the overestimation or underestimation of the tumor volume, a correction factor was introduced and estimated in the fitting process (Supplemental Eq. B3).

For the kidneys, the activity concentration was derived using the postprocessing software Syngo TrueD (Siemens Healthcare) with 15% or 20% of SUV_{max} and correction of background activity (Supplemental Eq. B4).

PBPK Modeling

To investigate the influence of the TTV on the BED, the application of PBPK modeling is required, as the tumor volume and all parameters that determine the biokinetics are explicitly modeled. A whole-body PBPK model for PSMA-specific ligands was recently developed (*8*). To account for tumor growth between the PET/CT imaging and the therapy, the PBPK model was modified to include exponential tumor growth (Supplemental Table A1). The assignment of data to the specific compartments was also improved (part B of the supplemental materials). The model includes all physiologically and physically relevant mechanisms such as blood flow, PSMA-specific binding, internalization and release of ^{177}Lu from the cells, excretion, and physical decay. The model and parameters are described in detail in part A of the supplemental materials.

The simulation analysis and modeling software (SAAM II and Popkinetics, version 2.2; The Epsilon Group) was used for fitting (*8*). For the 2 investigated tumor lesions, the receptor density, $R_{TU,0}$, and the blood flow density, f_{TU}, were estimated for each patient. The cell release rates of all tumor lesions, $\lambda_{TU,release}$, were assumed to be equal within one patient. For the kidneys, the blood flow density, f_K; receptor density, $[R_{K,0}]$; and release rate, $\lambda_{K,release}$, were also fitted. Because differences in salivary and lacrimal gland uptake do not considerably alter the tumor and kidney biokinetics, and planar imaging is inaccurate for these small organs, we assumed the literature values for the receptor densities and flows (*8*). The fitting was conducted in a Bayesian framework. Goodness of fit was evaluated using visual inspection,

the SE of the fitted parameters, the correlation matrix, and the coefficient of determination (*13*).

BEDs

The BEDs to each lesion were calculated (Supplemental Eqs. A14–A18) on the basis of the determined parameters and the radiobiologic parameters (for tumors, $\alpha/\beta = 1.49$ Gy (*14*) and a repair half-life μ of 1.9 h (*14*)) from radiotherapy and brachytherapy. For calculation of the absorbed dose to the kidneys, salivary glands, and tumors, only the self-dose was considered. Determination of the S values for each tumor lesion and the salivary glands was based on the data of OLINDA/EXM for ^{177}Lu for spheres (Supplemental Table A2). The BED model for red marrow was implemented according to Hindorf et al. (*15*) and calculated as described in part C of the supplemental materials.

Simulations

For the simulations and BED calculations, MATLAB/Simulink, version 2015b (The MathWorks, Inc.), was used. On the basis of the fitted parameters, the pharmacokinetics were simulated for, first, a TTV (i.e., the volume of the tumor REST plus the 2 tumor lesions) of 0.1, 0.3, 1, 3, and 10 L and, second, varying combinations of peptide amount (2–2^{10} nmol) and activity leading to a kidney dose of 5 $Gy_{2.5}$ (where the subscript denotes that an α/β of 2.5 Gy was used to calculate the BED). The limit of 5 $Gy_{2.5}$ was chosen because it is a commonly assumed tolerable dose to the kidneys allowing multiple cycles—for example, 8 when assuming a maximal cumulative dose of 40 $Gy_{2.5}$ and no additional risk factors. With these simulations, the BEDs were obtained for 2 tumor lesions, the tumor REST, the salivary glands, and the kidneys. The ratio of tumor BED to kidney BED was also determined. Mean values were derived for all patients and for just patients with a TTV of 0.3–3 L.

Dosimetry models for the salivary glands and the bone marrow (especially for highly metastasized bones and diffuse red marrow infiltration) include large uncertainties. However, to see the potential influence of the TTV (despite the known uncertainties) on the red marrow BED and salivary gland BED, the simulations were also conducted for these organs.

RESULTS

The goodness of fits was excellent for all patients as ascertained by visual inspection and the coefficient of determination ($R^2 > 0.9$) (Supplemental Fig. C1). All elements of the correlation matrix were within −0.8 and 0.8 in all patients. The relative SD for all fitted parameters in all patients was less than 28%. All estimated parameter values (Supplemental Table C2) were in a physiologically reasonable range.

The dependence of BED on TTV is shown in Figure 1 for a typical patient (patient 4) with high tumor receptor densities (~80 nmol/L). The results for all patients are provided in Supplemental Table C3A for BED and in Supplemental Table C3B for absorbed dose. The decreases in BED within a TTV of 0.3–3 L were considered most relevant, because the median of the patients' TTV was 0.22 L; 10 of 13 patients had a TTV of more than 0.1 L and only one a TTV of more than 3 L. The simulated BEDs to the tumor lesions and kidneys decreased by 58.2% and 58.4%, respectively, from a TTV of 0.3 L to a TTV of 3 L (Table 2). For all patients, the changes in the tumor-to-kidney BED ratio for standard amounts of peptide and activities were maximally 12%. The BEDs to the submandibular glands, parotid glands, and red marrow changed by 59%, 59%, and 185%, respectively, from a TTV of 0.3 L to a TTV of 3 L (Table 2). For a TTV of 10 L, the average BED to the bone marrow increased to 0.39 Gy_{15}.

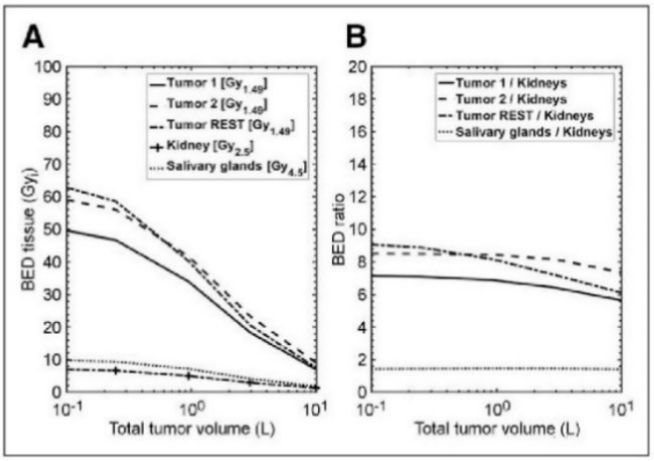

FIGURE 1. (A) Dependence of BED on TTV is shown for patient 4. (B) Tumor-to-kidney and salivary gland–to–kidney ratios with increasing TTV show that despite large absolute reduction in BEDs, ratios are only minimally influenced. Submandibular and parotid glands are depicted in single line as salivary glands because the values of the two are very similar to each other.

Figure 2 shows the optimal amount of peptide and pertaining activity for patient 4 with the maximal BED to the kidneys fixed to 5 $Gy_{2.5}$. The individual results for all patients are provided in Supplemental Table C4. Patients with a high tumor burden (>0.3 L) could be administered higher activities (10.4 ± 4.4 GBq) and peptide amounts (273 ± 136 nmol) without exceeding the tolerable BED to the kidneys.

DISCUSSION

The influence of larger tumor masses on pharmacokinetics is known as the tumor sink effect (*9*). This may lead to decreased activity concentrations in healthy tissue (*10*) but also in the tumor, with the risk of underdosing the tumor. In this work, we have quantitatively investigated the influence of TTV on the pharmacokinetics and thus on the BED to the OARs and tumors for PSMA-specific peptides. We used a recently developed PBPK model (*8*) that was simultaneously fitted to PET/CT and planar images to determine the pharmacokinetic parameters for each patient. The PET/CT information and the PBPK model were used to correct for nontumor activity in the tumor regions of interest on the planar images. However, SPECT/CT imaging during therapy, assuming a well-calibrated measurement system, would improve the accuracy of the individual pharmacokinetic parameters. An approximately 50-fold higher amount of peptide was used for therapeutic applications than for PET imaging. The parameters therefore describe the pharmacokinetics of smaller amounts and larger amounts, thus improving the reliability of the simulations. Within the PBPK model, the molecular weight, affinity, activity, physical decay, and peptide amount of the ^{68}Ga-PSMA HBED-CC and ^{177}Lu-PSMA I&T injections were considered. The fitted parameters were in a physiologically reasonable range. On the basis of these parameters (e.g., receptor densities), simulations with TTVs of between 0.1 and 10 L were conducted. The BED to the kidneys and tumors decreased considerably. Our results are remarkably similar to the SUV_{mean} decline in kidneys (55%), submandibular glands

TABLE 2
Changes in BED by TTV

Organ	BED for TTV of…		
	0.3 L	1 L	3 L
Tumor lesion ($Gy_{1.49}$)	22 ± 15	18 ± 11 (84.2% ± 8.8%)	11.0 ± 6.0 (58.2% ± 17.5%)
Tumor REST ($Gy_{1.49}$)	26 ± 16	20 ± 10 (81% ± 10%)	11.4 ± 4.7 (53% ± 19%)
Kidneys ($Gy_{2.5}$)	6.5 ± 2.3	5.4 ± 1.8 (84.3% ± 8.4%)	3.7 ± 1.4 (58.4% ± 16.6%)
Submandibular glands ($Gy_{4.5}$)	10.9 ± 2.7	9.2 ± 2.1 (84.6% ± 8.0%)	6.3 ± 1.9 (59% ± 16%)
Parotid glands ($Gy_{4.5}$)	11.0 ± 2.7	9.2 ± 2.1 (84.6% ± 8.1%)	6.4 ± 1.9 (59% ± 16%)
Red marrow (Gy_{15})	0.17 ± 0.05	0.23 ± 0.08 (136% ± 15%)	0.3 ± 0.1 (185% ± 29%)

Data in parentheses are relative to 0.3 L.

(64%), and parotid glands (57%) between patients with a low tumor load and patients who were classified as having a "high tumor load" in a study by Gaertner et al. (*10*). The increase in red marrow BED with increasing tumor burden occurs because of higher total-body retention.

Garske et al., in a case report on ^{177}Lu DOTA-octreotate therapy, noted that one lesson learned was the relevance of the amount of peptide relative to the number of receptors (*16*). With increasing tumor load (using the same activity and peptide amount), the tumor-to-kidney BED ratio slightly decreased as the saturation effects of the kidneys were reduced with less available peptide. However, the ratio can be improved by applying higher amounts of peptide with adapted activity. For antibodies (*17–19*) and peptides (*8,11,20*), it has been shown that an optimal tumor-to-OAR ratio exists for each patient. Using an algorithm developed by Kletting et al. (*11*), we determined, for each individual patient, the optimal activity and peptide amount for a maximal kidney BED of 5 $Gy_{2.5}$ for 1 cycle. The tumor radiobiologic parameters from Fowler et al. (*14*) were used, although there is ongoing controversy about the actual range (*21*) and its applicability to RLT. Therefore, the absorbed doses and the BED for an α/β of 1.8, reported by Dearnaley et al. (*21*), are also provided in Supplemental Tables C3B and C3C. The maximal deviation for the tumor BED was 5% over the range of α/β values. The results indicate that through individualized dosimetry based on our PBPK model, the BED to the tumors could be safely maximized by optimizing the tumor-to-kidney BED ratio for a given limiting BED. This holds especially true for patients with a high tumor burden. However, because the number of possible cycles could also be limited by the bone marrow BED (Supplemental Table C4) (*22*) or the salivary gland BED, an overall optimization approach simultaneously taking into account all OARs and treatment effects is desirable. Future studies with quantitative 3-dimensional imaging (during therapy) are required to accurately estimate the parameters for the salivary (and lacrimal) glands. In addition, improved models for red marrow dosimetry are needed to accurately estimate the red marrow dose. The Simulink model and the algorithm can easily be modified to consider more than one OAR or limiting dose.

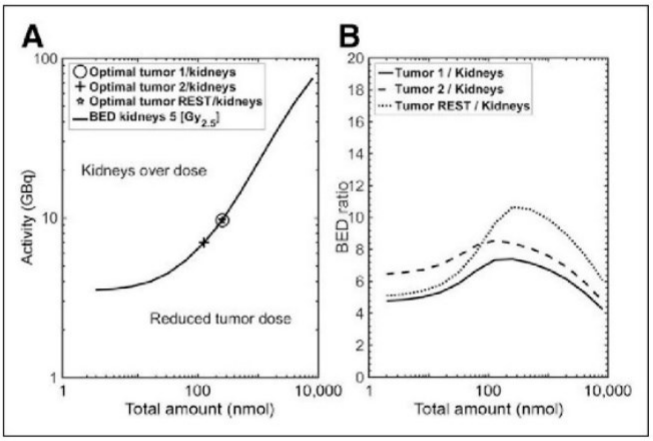

FIGURE 2. Optimal combination of peptide amount and activity for tumor lesions and tumor REST with maximal BED to kidneys of 5 $Gy_{2.5}$ is shown for patient 4 (high receptor density and TTV of 0.37 L). (A) All combinations of activity and peptide amount that lead to BED of 5 $Gy_{2.5}$ are shown. (B) Most favorable combination is maximal graphed point.

The idea of using the diagnostic PET/CT scan for treatment planning (*23*) is intriguing but requires several elements: a PPBK model that considers different affinities, peptide amounts, and half-lives of the PET and therapeutic agents; population parameters with an acceptably low SD for the release rates and the receptor densities; modeling of tumor growth and potential changes in salivary gland function due to cooling or candies; and an algorithm that objectively determines the PSMA-positive tumor volume without information on the therapeutic planar total-body time–activity data. Then, future clinical management could be changed by adapting the activity and peptide amount individually before the first therapeutic cycle. Individual adaptation is also relevant for early phases of the disease with a low tumor burden, as the optimal combination of activity and peptide amount might be considerably different from that in the patient population with a high tumor burden.

CONCLUSION

This modeling and simulation study indicated that the tumor burden considerably affects the BEDs to tumors and OARs. Our data suggest that patients with a large PSMA-ligand–positive tumor mass might be safely administered higher activities and peptide amounts to maximize the tumor BED without exceeding the critical dose to the OARs.

DISCLOSURE

This work was supported by LPDP-Lembaga Pengelola Dana Pendidikan (the Indonesia Endowment Fund for Education,

Ministry of Finance, Indonesia) (s-2512/LPDP.3/2016) and the Deutsche Forschungsgemeinschaft (the German Research Foundation) (KL2742/2-1, BE4393/1-1, GL236/11-1, and SFB824 project B11). No other potential conflict of interest relevant to this article was reported.

REFERENCES

1. Okamoto S, Thieme A, Allmann J, et al. Radiation dosimetry for Lu-177-PSMA I&T in metastatic castration-resistant prostate cancer: absorbed dose in normal organs and tumor lesions. *J Nucl Med.* 2017;58:445–450.
2. Rahbar K, Ahmadzadehfar H, Kratochwil C, et al. German multicenter study investigating ^{177}Lu-PSMA-617 radioligand therapy in advanced prostate cancer patients. *J Nucl Med.* 2017;58:85–90.
3. Baum RP, Kulkarni HR, Schuchardt C, et al. ^{177}Lu-labeled prostate-specific membrane antigen radioligand therapy of metastatic castration-resistant prostate cancer: safety and efficacy. *J Nucl Med.* 2016;57:1006–1013.
4. Kratochwil C, Giesel FL, Stefanova M, et al. PSMA-targeted radionuclide therapy of metastatic castration-resistant prostate cancer with ^{177}Lu-labeled PSMA-617. *J Nucl Med.* 2016;57:1170–1176.
5. Delker A, Fendler WP, Kratochwil C, et al. Dosimetry for ^{177}Lu-DKFZ-PSMA-617: a new radiopharmaceutical for the treatment of metastatic prostate cancer. *Eur J Nucl Med Mol Imaging.* 2016;43:42–51.
6. Kabasakal L, AbuQbeitah M, Aygun A, et al. Pre-therapeutic dosimetry of normal organs and tissues of ^{177}Lu-PSMA-617 prostate-specific membrane antigen (PSMA) inhibitor in patients with castration-resistant prostate cancer. *Eur J Nucl Med Mol Imaging.* 2015;42:1976–1983.
7. Scarpa L, Buxbaum S, Kendler D, et al. The ^{68}Ga/^{177}Lu theragnostic concept in PSMA targeting of castration-resistant prostate cancer: correlation of SUVmax values and absorbed dose estimates. *Eur J Nucl Med Mol Imaging.* 2017;44:788–800.
8. Kletting P, Schuchardt C, Kulkarni HR, et al. Investigating the effect of ligand amount and injected therapeutic activity: a simulation study for ^{177}Lu-labeled PSMA-targeting peptides. *PLoS One.* 2016;11:e0162303.
9. Beauregard JM, Hofman MS, Kong G, Hicks RJ. The tumour sink effect on the biodistribution of ^{68}Ga-DOTA-octreotate: implications for peptide receptor radionuclide therapy. *Eur J Nucl Med Mol Imaging.* 2012;39:50–56.
10. Gaertner FC, Halabi K, Ahmadzadehfar H, et al. Uptake of PSMA-ligands in normal tissues is dependent on tumor load in patients with prostate cancer. *Oncotarget.* 2017;8:55094–55103.
11. Kletting P, Kull T, Maass C, et al. Optimized peptide amount and activity for ^{90}Y-labeled DOTATATE therapy. *J Nucl Med.* 2016;57:503–508.
12. Nestorov I. Whole-body physiologically based pharmacokinetic models. *Expert Opin Drug Metab Toxicol.* 2007;3:235–249.
13. Kletting P, Schimmel S, Kestler HA, et al. Molecular radiotherapy: the NUKFIT software for calculating the time-integrated activity coefficient. *Med Phys.* 2013; 40:102504.
14. Fowler J, Chappell R, Ritter M. Is alpha/beta for prostate tumors really low? *Int J Radiat Oncol Biol Phys.* 2001;50:1021–1031.
15. Hindorf C, Glatting G, Chiesa C, Lindén O, Flux G. EANM Dosimetry Committee guidelines for bone marrow and whole-body dosimetry. *Eur J Nucl Med Mol Imaging.* 2010;37:1238–1250.
16. Garske U, Sandström M, Johansson S, et al. Lessons on tumour response: imaging during therapy with ^{177}Lu-DOTA-octreotate: a case report on a patient with a large volume of poorly differentiated neuroendocrine carcinoma. *Theranostics.* 2012;2:459–471.
17. Kletting P, Bunjes D, Reske SN, Glatting G. Improving anti-CD45 antibody radioimmunotherapy using a physiologically based pharmacokinetic model. *J Nucl Med.* 2009;50:296–302.
18. Kletting P, Kull T, Bunjes D, Luster M, Reske SN, Glatting G. Optimal preloading in radioimmunotherapy with anti-cD45 antibody. *Med Phys.* 2011;38:2572–2578.
19. Pandit-Taskar N, O'Donoghue JA, Divgi CR, et al. Indium 111-labeled J591 anti-PSMA antibody for vascular targeted imaging in progressive solid tumors. *EJNMMI Res.* 2015;5:28.
20. Kletting P, Muller B, Erentok B, et al. Differences in predicted and actually absorbed doses in peptide receptor radionuclide therapy. *Med Phys.* 2012;39:5708–5717.
21. Dearnaley D, Syndikus I, Mossop H, et al. Conventional versus hypofractionated high-dose intensity-modulated radiotherapy for prostate cancer: 5-year outcomes of the randomised, non-inferiority, phase 3 CHHiP trial. *Lancet Oncol.* 2016;17: 1047–1060.
22. Rathke H, Giesel FL, Flechsig P, et al. Repeated Lu-177-PSMA-617 radioligand therapy using treatment activities up to 9.3 GBq. *J Nucl Med.* August 10, 2017 [Epub ahead of print].
23. Hardiansyah D, Maass C, Attarwala AA, et al. The role of patient-based treatment planning in peptide receptor radionuclide therapy. *Eur J Nucl Med Mol Imaging.* 2016;43:871–880.

2.2 The effect of ligand amount, affinity, and internalization on imaging and therapy

2.2.1 Summary

In the previous publication [59], the effect of TTV on BED was investigated. In addition to variability between patients, pharmacokinetic changes may also be caused by differences in the ligands' properties (e.g., molecular size and ligand affinity) [67]. Therefore, the same ligand with different labeling (e.g., ^{68}Ga for imaging and ^{177}Lu for therapy) has generally been used in theranostics to minimize changes in pharmacokinetics [17]. The development and optimization of theranostics are challenging because a high tumor-to-kidney ratio is desired for imaging, while a high tumor-to-kidney absorbed dose for therapy. Fundamental work on the influence of affinity and ligand amount has been performed [16]. In this work, the study was conducted for both imaging and therapy while considering different ligand properties, quantities of interest (activity concentrations versus absorbed doses), and administered amounts of ligand. The aim was to investigate the interaction between affinity, internalization, and injected ligand amount of PSMA-specific ligands using a PBPK modeling and simulation approach.

The 13 patients and PBPK model in the previous publication [59] were included in this work. The PBPK model includes *prior* knowledge of the individual patient, the ligand properties and the amount of administered activity, and the ligand of the ^{68}Ga-PSMA-11 and ^{177}Lu-PSMA I&T injections. The published PBPK model and related calculation of activity concentration and absorbed dose were implemented in MATLAB®/Simbiology (version 2018a The MathWorks, Inc., Natick, Massachusetts, United States). The binding affinity is the inverse of the dissociation constant K_D, the ratio between the dissociation rate k_{off} and the association rate k_{on} ($K_D = k_{off}/k_{on}$) [68]. The higher the affinity, the lower the K_D value. Simulations were performed for K_D values (1, 0.1 and 0.01 nM) with different combinations of k_{on} (0.1–0.01 L/nmol/min) and k_{off} (0.1–0.0001 min^{-1}). These amounts were assayed for various combinations of ligand amounts (1–1000 nmol inr of 10) with an injected mean activity of (7.3±0.3) GBq ^{177}Lu-PSMA. The range of the k_{on} and k_{off} values used was taken from in-house surface plasmon resonance measurements (e.g., K_D of PSMA-617 was 0.06 nM [53, 69]). Different combinations of k_{on} and k_{off} for the same K_D value were studied. To limit the number of possible combinations of k_{on} and k_{off} to a reasonable number, two combinations for each K_D value were investigated for three different internalization rate λ_{int} values (0.01, 0.001, and 0.0001 min^{-1}). An effective internalization rate was assumed as reported for pharmacokinetic modeling of antibodies [53]. The number of PSMA receptors was estimated in previous work using PSMA-11 and PSMA I&T data and also represents effective values encompassing all receptor subtypes.

For imaging, the activity concentrations of each relevant organ *i* were normalized to the volume V_i of organ *i* and the administered activity A_0 (hereafter referred to as "normalized" activity concentrations $C_i(t)$) without decay correction 1 h after injection of ^{68}Ga-PSMA (equation (11)). The relevant organs *i* were two tumor lesions, tumor REST, background (including muscle and fat), OARs (e.g., kidneys, liver, red marrow), gastrointestinal tract, and lung.

$$C_i(t) = \frac{A_i(t)}{A_0 \cdot V_i}, \tag{11}$$

For therapy, the absorbed doses of ^{177}Lu-PSMA radioligand therapy (Injected activity: (7.3±0.3) GBq) were calculated for therapeutically relevant organs *i*, i.e., the two tumor lesions, the tumor REST, the kidneys, and red marrow, based on the MIRD formalism using equation (7) in Section 1.1.1.

Imaging

Effect of association and dissociation rate k_{on} and k_{off}

The impact of the investigated combinations of k_{on} and k_{off} on the normalized activity concentration at 1 h p.i. is small for tumors and OARs. However, k_{on} has a more substantial effect on normalized activity concentration in tumors and OARs than k_{off}.

Effect of ligand amount

The influence of the amount of ligand (1-32 nmol) is small for tumors and OARs. However, for the dissociation constant K_D <1 nM, the higher the association rate k_{on}, the more important the ligand injected is. The maximum improvements were obtained when the ligand amount of 32 nmol was administered.

Effect of the internalization rate λ_{int}

The parameter λ_{int} had no significant effect on the normalized activity concentration in the tumor, all organs, and background. The influence of the dissociation constant K_D, association and dissociation rates k_{on} and k_{off} on the normalized activity concentration in tumor, OARs, and background showed similar results for different internalization rates λ_{int}.

Therapy

Effect of association and dissociation rate k_{on} and k_{off}.

The effect of k_{on} and k_{off} on the absorbed dose is considerable, especially for the tumor lesions with moderate blood flow and receptor density. The impact of different k_{on} and k_{off} for the same K_D is less prominent. A decrease of the dissociation constant K_D resulted in increased absorbed dose to tumors and other PSMA-positive organs, e.g., kidneys.

Effect of ligand amount

For all combinations of association and dissociation rates, k_{on} and $k_{off,}$ the highest absorbed doses were simulated for 32 nmol. Increasing the ligand amount led to a decrease in the tumor (especially in highly perfused tissue for high affinities) and the kidneys. For dissociation constants K_D<1 nM with an association rate k_{on}=0.1 L/nmol/min, the kidneys' absorbed dose decreased stronger than larger dissociation constant K_D values. The ligand amount had a minor effect on the absorbed dose in red marrow.

Effect of the internalization rate λ_{int}

The effect of the internalization rate λ_{int} on the absorbed dose in the tumor varied considerably depending on the dissociation constant K_D and the ligand amount. For the dissociation constant K_D=1 nM, the higher the internalization rate λ_{int} and ligand amount, the higher the absorbed dose in the tumor. For affinities K_D<1 nM and with an internalization rate λ_{int} =0.01min^{-1}, a ligand amount >32 nmol is required to achieve a sufficiently high absorbed dose in the tumor. Conversely, for the internalization rate λ_{int}=0.0001 min^{-1}, higher ligand amount led to a lower absorbed dose in the tumor. The absorbed dose in kidneys was higher for the internalization rate λ_{int}=0.01 min^{-1} compared to λ_{int} =0.001 min^{-1} for all dissociation constants K_D using a ligand amount ≥32 nmol. The ligand amount affected the absorbed dose in the kidneys for the internalization rate λ_{int}=0.01 min^{-1}; however, only minor for the internalization rate λ_{int}=0.0001 min^{-1}. The absorbed dose in kidneys increased by a factor of 3.0±0.3 with an internalization rate λ_{int}=0.01 min^{-1} compared to the λ_{int}=0.001 min^{-1} using a ligand amount of 32 nmol and the dissociation constant K_D=1 nM (k_{off}=0.01min−1; k_{on}=0.01L/nmol/min). The internalization rate λ_{int} only slightly affects the absorbed dose in red marrow regardless of the ligand amount.

Effects on tumor-to-kidneys absorbed dose ratio

The parameter values leading to the highest tumor-to-kidney absorbed dose ratio for different λ_{int} were:

- For λ_{int}= 0.01 min^{-1}: k_{on}=0.01 L/nmol/min, k_{off}=0.01 min^{-1} with ligand amount of 316 nmol (ratio of 3.0±2.2 for tumor lesions and 3.0±2.1 for tumor REST),
- For λ_{int}= 0.001 min^{-1}: k_{on} = 0.1 L/nmol/min, k_{off}=0.1 min^{-1} with ligand amount of 316 nmol (ratio of 3.8±2.6 for tumor lesions and 4.9±3.2 for tumor REST) and

- For λ_{int} =0.0001 min^{-1}: k_{on}=0.1 L/nmol/min, k_{off}=0.01 min^{-1} with ligand amount of 100 nmol (ratio of 3.8±2.6 for tumor lesions and 5.1±3.3 for tumor REST).

In conclusion, the impact of the characteristics evaluated on therapy was more substantial than imaging. For imaging, the properties that resulted in the highest tumor uptake were k_{on}=0.1 L/nmol/min, k_{off}=0.01 min^{-1} for typical amounts of ligand (1-10 nmol). For therapy, the higher the internalization rate, the greater the amount of ligand required for an optimal tumor-to-kidney ratio. The higher the affinity, the more decisive was the right amount of ligand (i.e., the lower the K_D).

2.2.2 Copyright and own contributions

This included article is published by Springer Nature under the terms of the Creative Commons Attribution CC BY 4.0 International license (http://creativecommons.org/licenses/by/4.0) as [60]:

> **Begum NJ,** Glatting G, Wester HJ, Eiber M, Beer AJ, Kletting P. The effect of ligand amount, affinity and internalization on PSMA-targeted imaging and therapy: A simulation study using a PBPK model. Sci Rep. 2019;9(1):20041. DOI: 10.1038/s41598-019-56603-8.

The supplemental material of this publication is provided in appendix A.2 and available online at https://doi.org/10.1038/s41598-019-56603-8.

Copyright
Copyright © 2019 by Begum NJ, Glatting G, Wester HJ, Eiber M, Beer AJ, Kletting P.

Own contributions:
I contributed to the conception and design of the study. I developed and implemented the MATLAB®/Simbiology script (version 2018a) and the PBPK model to simulate ligand amount, affinity, and internalization on activity concentration and absorbed dose. I performed the data analyses and graphical representation of the results. I wrote, edited, and reviewed the manuscript with all co-authors.

SCIENTIFIC REPORTS
nature research

OPEN

The effect of ligand amount, affinity and internalization on PSMA-targeted imaging and therapy: A simulation study using a PBPK model

Nusrat J. Begum[1*], Gerhard Glatting[1,2], Hans-Jürgen Wester[3], Matthias Eiber[4], Ambros J. Beer[2] & Peter Kletting[1,2]

The aim of this work was to investigate the effect of ligand amount, affinity and internalization of prostate-specific membrane antigen (PSMA)-specific ligands on the activity concentrations for PET/CT imaging and on the absorbed doses for therapy. A physiologically-based pharmacokinetic (PBPK) model for PSMA-specific ligands was implemented. Thirteen virtual patients with metastatic castration-resistant prostate cancer were analysed. Simulations were performed for different combinations of association rates k_{on} (0.1–0.01 L/nmol/min), dissociation rates k_{off} (0.1–0.0001 min^{-1}), internalization rates λ_{int} (0.01–0.0001 min^{-1}) and ligand amounts (1–1000 nmol). For imaging the activity was normalized to volume and injected activity (^{68}Ga-PSMA at 1 h). For therapy the absorbed dose was calculated for 7.3 ± 0.3 GBq ^{177}Lu-PSMA. The effect of the investigated parameters on therapy were larger compared to imaging. For imaging, the combination of properties leading to the highest tumour uptake was k_{on} = 0.1 L/nmol/min, k_{off} = 0.01 min^{-1} for typical ligand amounts (1–10 nmol). For therapy, the higher the internalization rate, the larger was the required ligand amount for optimal tumour-to-kidney ratios. The higher the affinity, the more important was the choice of the optimal ligand amount. PBPK modelling provides insight into the pharmacokinetics of PSMA-specific ligands. Further *in silico* and *in vivo* studies are required to verify the influence of the analysed parameters.

Theranostics refers to the use of individual patient-level biological information from imaging to determine an optimal therapy for an individual patient[1,2]. Thus, ideally, theranostic agents can be used for both, imaging and therapy to minimize changes in pharmacokinetics due to different chemical structures. The prostate-specific membrane antigen (PSMA) has received increasing interest for theranostic approaches in prostate cancer[3,4]. PSMA-specific ligands are predominantly labelled with ^{68}Ga/^{177}Lu or ^{18}F/^{177}Lu for imaging and therapy[5].

Beside important ligand properties like molecular size or lipophilicity, the association and dissociation rate k_{on} and k_{off} and the internalization rate λ_{int} influence the pharmacokinetics[6]. The binding affinity is described by the dissociation constant $K_D = k_{off}/k_{on}$[7]. High affinity (i.e. low K_D) is a prerequisite for imaging and therapy especially for small molecules with fast clearance[8]. However, it is unclear whether ligands optimized for imaging are also ideal candidates for radionuclide therapy, because of different quantities of interest (activity concentrations vs absorbed doses) and different administered ligand amounts[9]. Basic work on the influence of affinity and ligand amount has been conducted[10,11]. However up to now no investigation considering PSMA-targeting small molecules, internalization, different combinations of the association and dissociation rate k_{on} and k_{off} and various tissues for both imaging and therapy concurrently has been performed.

In silico investigations, e.g. by means of simulation and modelling, assist in the development and optimization of theranostics[12]. Computational approaches, e.g. using physiologically based pharmacokinetic (PBPK)

[1]Medical Radiation Physics, Department of Nuclear Medicine, Ulm University, Ulm, Germany. [2]Department of Nuclear Medicine, Ulm University, Ulm, Germany. [3]Technical University of Munich, Pharmaceutical Radiochemistry, Munich, Germany. [4]Technical University of Munich, School of Medicine, Klinikum rechts der Isar, Department of Nuclear Medicine, Munich, Germany. *email: nusrat.begum@uni-ulm.de

K_D[a] [nM]	k_{off}[b] [min^{-1}]	k_{on}[c] [L/nmol/min]
0.01	0.0001	0.01
0.01	0.001	0.1
0.1	0.001	0.01
0.1	0.01	0.1
1	0.01	0.01
1	0.1	0.1

Table 1. Investigated combinations of k_{on} and k_{off}. [a]K_D = Dissociation constant ($K_D = k_{off}/k_{on}$); [b]k_{off} = Dissociation rate; [c]k_{on} = Association rate.

models are important tools for the development of accurate and personalized treatments that are both cost- and time-effective[12]. PBPK models are increasingly used to systematically investigate pharmacokinetic parameters and absorbed doses[13–16]. PBPK models consider the individual patient biokinetics in the organs at risk (OARs) and in tumours[17]. Recently a whole-body PBPK model has been developed for PSMA radioligand therapy[15] based on data from PET/CT imaging with ^{68}Ga-PSMA-11 and peri-therapeutic measurements with ^{177}Lu-PSMA I&T.

The aim of this work was, to investigate the interconnected effect of affinity, internalization and injected ligand amount of PSMA-specific ligands using a PBPK modelling and simulation approach. For imaging the normalized activity concentrations in tumour, background, and OARs and for therapy the absorbed doses of tumours and the OARs were determined. These quantities were investigated for different combinations of ligand amounts (1–1000 nmol), internalization rates λ_{int} (0.01, 0.001 and 0.0001 min^{-1}) and dissociation constant K_D values (1, 0.1 and 0.01 nM).

Materials and Methods

Patient individualized PBPK model. A recently published PBPK model based on data from PET/CT imaging with PSMA-11 and peri-therapeutic measurements with PSMA I&T[15] was implemented in Simbiology/MATLAB (MATLAB R2018a, The MathWorks, Inc). The model includes all physiologically and physically relevant mechanisms such as blood flow, plasma protein binding, PSMA-specific binding, internalization and release from the cells, excretion, and physical decay. An effective internalization rate as reported for antibody pharmacokinetic modelling[18,19] was assumed. The number of PSMA receptors (which were estimated in previous work using PSMA-11 and PSMA I&T data) also represent effective values including all receptor subtypes.

The competition of labelled and unlabelled peptide (with the same affinity) is described by two separate circulation systems for binding to PSMA and by physical decay. The tumours, kidneys, liver, and the gastrointestinal tract were considered as PSMA-positive tissues. Two tumour lesions were explicitly modelled showing highest uptake and no overlap with other PSMA-positive tissues. All other tumour lesions were merged into tumour REST. The cumulated activity and volume of the tumour REST were obtained by adding all lesions slice by slice using isocontours of 15–20%. To correct the overestimation or underestimation of tumour volume, a correction factor was estimated in the fitting process[15].

For the kidney model, PSMA-specific binding, internalization, release and all mechanisms pertaining to clearance were included. Amino acids were administered to block unspecific uptake as applied in PRRT. Therefore, unspecific uptake in kidney was assumed to be low. The model, its parameters and the fitting methods are described in detail elsewhere[15,16]. In brief, the model parameters were fitted to time-activity data of thirteen patients including covariates such as age and body weight[15]. These 13 patient-individualized models (virtual patients) were used in this work as a basis for all simulations. The parameter distributions of the tumour were wide, e.g. total tumour volume (Median: 0.4, Range: 0.02–5) l, receptor densities (Median: 50, Range: 4–124) nmol/l, blood flows (Median: 0.2, Range: 0.02–1.6) ml/min/g. Receptor densities in tumour REST were higher and perfusion lower on average compared to the single lesions. The virtual patients account for all these differences. The institutional review board of the Technische Universität München approved all procedures and the compassionate use of ^{177}Lu-PSMA I&T in metastatic castration-resistant prostate cancer patients who had no other therapeutic options. All procedures in this study were performed in accordance with relevant guidelines and regulations. All subjects signed a written informed consent form.

Simulations. The simulations were conducted for dissociation constant K_D values of 1, 0.1 and 0.01 nM and ligand amounts of 1–1000 nmol inr of $\sqrt{10}$ with an injected mean activity (±SD) of (7.3 ± 0.3) GBq ^{177}Lu-PSMA. The range of the herein used association and dissociation rate k_{on} and k_{off} values were taken from in-house surface plasmon resonance measurements[20,21]. For example, for the ligand PSMA-617 dissociation constant K_D (k_{off}/k_{on}) was determined to be 0.06 nM. The dissociation rate k_{off} value of 0.0001 min^{-1} (not measured) was added for a more systematic investigation. Different combinations of association and dissociation rates k_{on} and k_{off} for the same dissociation constant K_D value were investigated. To limit the number of possible combinations of association and dissociation rates k_{on} and k_{off} to a reasonable number, two combinations for each dissociation constant K_D were investigated for 3 different internalization rate λ_{int} values (0.01, 0.001 and 0.0001) min^{-1} (Table 1).

Imaging. The normalized activity concentrations without decay correction 1 h after injections of ^{68}Ga-PSMA were investigated for two tumour lesions, tumour REST, background (including muscle and fat), organs at risk OARs (kidneys, liver, red marrow), gastrointestinal tract and lung. The normalized activity concentrations $c_i(t)$ of

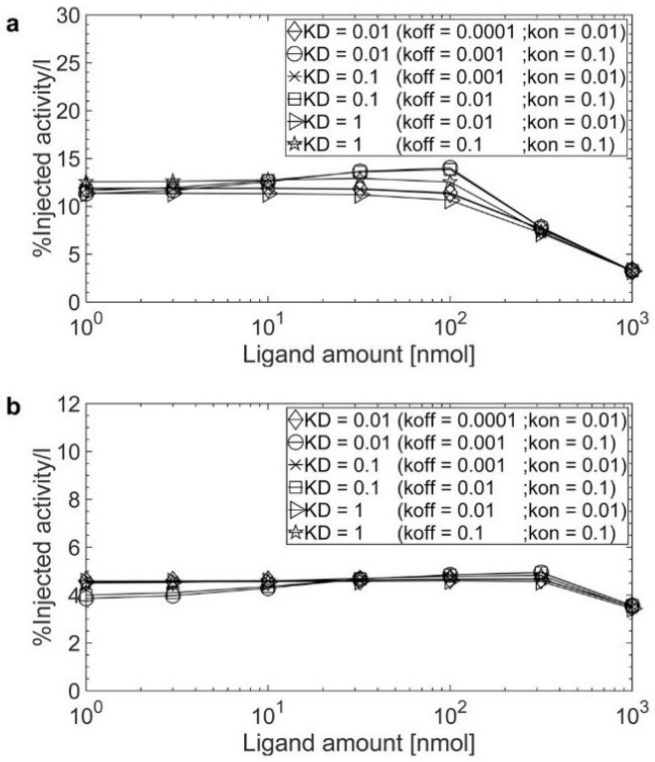

Figure 1. Normalized activity concentrations for ^{68}Ga-labelled PSMA-specific ligands (1 h p.i.) for the internalization rate $\lambda_{int} = 0.001\ min^{-1}$ in (**a**) a tumour lesion (receptor density 33 nmol/l and perfusion 0.08 ml/g/min) and (**b**) tumour REST (receptor density 66 nmol/l and perfusion 0.04 ml/g/min) of patient 5.

each relevant organ i were calculated using (Eq. 1), where $A_i(t)$ is the activity in organ i, A_0 is the injected activity and V_i is the volume of organ i:

$$c_i(t) = \frac{A_i(t)}{A_0 \cdot V_i} \tag{1}$$

Therapy. The absorbed doses of ^{177}Lu-PSMA radioligand therapy (Activity: (7.3 ± 0.3) GBq) were calculated for therapeutically relevant organs i, i.e. the two tumour lesions, the tumour REST, the kidneys and red marrow, based on the MIRD formalism as follows:

$$D_i(T) = A_0 \cdot \tilde{a}_i(T) \cdot S_{i \leftarrow i} \tag{2}$$

with the dose $D_i(T)$ to organ i (where $T = 30000$ min), the injected activity A_0, the time-integrated activity coefficient $\tilde{a}_i(T)$ and the dose factor organ i to organ i $S_{i \leftarrow i}$. For tumours and kidneys, only the self-dose was considered. The S-values for each tumour lesion and OARs were determined based on the data of OLINDA/EXM for ^{177}Lu for spheres[15]. For bone marrow the absorbed dose calculation includes other relevant organs and tumours[15].

Results

Imaging. The results for imaging considering all patients, different ligand amounts, association and dissociation rates k_{on} and k_{off}, and internalization rates λ_{int} are presented in the supplement (Table S1 for tumour and Table S2 and S3 for organs at risk OARs and background). Figure 1a,b show the normalized activity concentration in a tumour lesion and tumour REST depending on association and dissociation rates k_{on} and k_{off}, and the applied ligand amount for a typical patient. The figure for the background is provided in the supplement (Fig. S1). All results described in the sections below refer to the internalization rate $\lambda_{int} = 0.001\ min^{-1}$ which is used in the published model[15].

Effect of association and dissociation rate k_{on} and k_{off}. Tumours. In general the effect of the investigated combinations of association and dissociation rates k_{on} and k_{off} on the normalized activity concentration 1 h p.i. is low (Fig. 1). However, varying the association rate k_{on} seems to have a larger effect than varying the dissociation rate k_{off}. Changing the association rate k_{on} from 0.01 to 0.1 L/nmol/min (with a fixed dissociation rate k_{off} of 0.01 min^{-1}) increased the normalized concentration by a factor of 1.2 ± 0.3 for tumour lesions and 1.1 ± 0.1 for tumour REST using the commonly used ligand amount of 10 nmol for imaging (Supplement, Table S4).

Organs at risk and background. Similar to the tumour, the association rate k_{on} has a more pronounced effect on the normalized activity concentrations in OARs than the dissociation rate k_{off}. Decreasing the dissociation

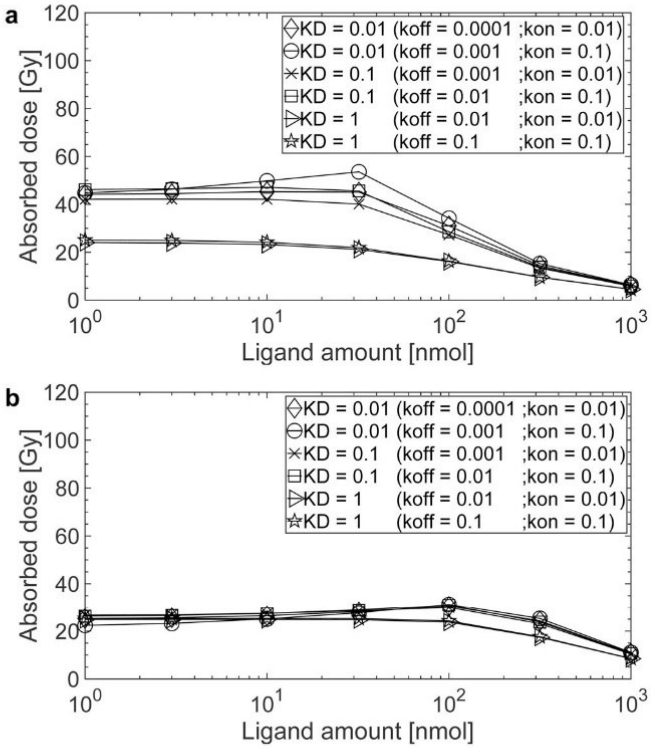

Figure 2. The absorbed doses for ^{177}Lu-labelled (7.5 GBq) PSMA-specific ligands for the internalization rate $\lambda_{int} = 0.001\ min^{-1}$ in (**a**) a tumour lesion (receptor density 33 nmol/l and perfusion 0.08 ml/g/min) and (**b**) tumour REST (receptor density 66 nmol/l and perfusion 0.04 ml/g/min) of patient 5.

constant K_D by increasing the association rate k_{on} led to an increase of the normalized activity concentration in the kidneys and liver, and to a decrease in the lung, gastrointestinal tract, red marrow and background (Supplement, Tables S2 and S3).

Effect of ligand amount. Tumours. Overall the effect of ligand amount (1–32 nmol) is low. However, the effect of the ligand amount is more pronounced for the dissociation constant $K_D < 1$ nM with an association rate $k_{on} = 0.1$ L/nmol/min. For combinations of association and dissociation rates k_{on} and k_{off} leading to the same dissociation constant K_D, the higher the association rate k_{on} the more important is the injected ligand amount (Fig. 1a,b). The maximal improvements were achieved if the ligand amount of 32 nmol is administered. The highest improvement was obtained with a dissociation constant $K_D = 0.01$ nM ($k_{on} = 0.1$ L/nmol/min; $k_{off} = 0.001\ min^{-1}$): using 32 nmol compared to 1 nmol the normalized activity concentrations increased by a factor of 1.2 ± 0.1 for tumour lesions and 1.18 ± 0.03 for tumour REST (Supplement, Table S1). For the dissociation constant $K_D = 1$, the normalized activity concentrations were similar regardless of the administered ligand amount (1–32 nmol).

Organs at risk and background. Only for the dissociation constant $K_D < 1$ nM with an association rate $k_{on} = 0.1$ L/nmol/min the normalized activity concentrations varied considerably depending on the ligand amount. Otherwise the normalized activity concentrations in OARs and background were similar regardless of the ligand amounts (1–32 nmol) (Supplement, Tables S2 and S3).

Effect of the internalization rate λ_{int}. Tumours, organs at risk and background. The parameter λ_{int} did not considerably affect the normalized activity concentration in tumour, all organs and background. The influence of the dissociation constant K_D, association and dissociation rates k_{on} and k_{off} on the normalized activity concentration in tumour, OARs and background showed similar results for different internalization rates λ_{int} (Supplement, Tables S1–S3).

Therapy. The results for therapy considering all patients, different ligand amounts, association and dissociation rates k_{on} and k_{off} and internalization rates λ_{int} are presented in the supplement (Table S5 for tumour, Table S6 for OARs and Table S7 for tumour-to-kidneys absorbed dose ratio). Figures 2a,b and 3 show the absorbed dose of the tumour lesions, the tumour REST and the kidneys depending on the association and dissociation rates k_{on} and k_{off} and on the applied ligand amount for a typical patient. The corresponding Figure for the red marrow is provided in the supplement (Fig. S2). All results described in the sections below refer to the internalization rate $\lambda_{int} = 0.001\ min^{-1}$, which is used in the published model[15] and to ligand amounts relevant for therapy, i.e. 32–316 nmol.

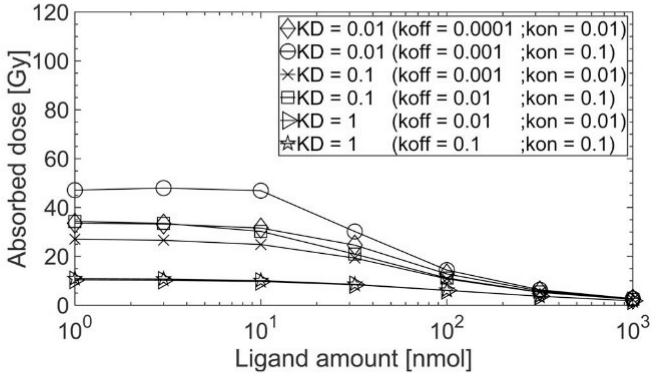

Figure 3. The absorbed dose for ^{177}Lu-labelled (7.5 GBq) PSMA-specific ligands for the internalization rate $\lambda_{int} = 0.001\ min^{-1}$ in kidneys (receptor density 19 nmol/l and age adjusted perfusion 1.7 ml/g/min) of patient 5.

Effect of association and dissociation rates k_{on} and k_{off}. Tumours. Figure 2a,b show the dependence of the absorbed dose on the amount of ligand, association and dissociation rate k_{on} and k_{off}, for tumour lesions and tumour REST, respectively. For the single tumour lesion with moderate blood flow and receptor density the effect of decreasing the dissociation constant K_D is considerable. The effect of different association and dissociation rates k_{on} and k_{off} for the same dissociation constant K_D is less prominent. Using a commonly applied ligand amount for therapy of 100 nmol, decreasing the dissociation constant K_D from 1 nM to 0.1 nM either by decreasing the dissociation rate k_{off} from 0.1 to 0.01 min^{-1} (with a fixed association rate $k_{on} = 0.1$ L/nmol/min) or by increasing association rate k_{on} from 0.01 to 0.1 min^{-1} (with a fixed dissociation rate $k_{off} = 0.01$ L/nmol/min) led to same results: the absorbed dose in tumour increased by a factor of 1.9 ± 0.2 for tumour lesions and 1.7 ± 0.4 for tumour REST (Supplement, Table S5).

For the tumour REST, which has a lower perfusion and a higher receptor density, association and dissociation rate k_{on} and k_{off} have only minimal influence for the investigated range. Figure 2a,b show that although the receptor density of tumour REST is two-fold larger, the two-fold lower perfusion diminishes the effect of higher affinity for the dissociation constant $K_D < 1$ nM.

Organs at risk. A decrease of the dissociation constant K_D resulted in an increase of the absorbed dose to other PSMA-positive organs in all patients (e.g. kidneys, Fig. 3). The absorbed doses increased by a factor of 2.1 ± 0.2 for kidneys when the dissociation constant K_D changed from 1 to 0.1 nM by decreasing the dissociation rate k_{off} from 0.1 to 0.01 min^{-1} (with a fixed association rate $k_{on} = 0.1$ L/nmol/min and a ligand amount of 100 nmol) (Supplement, Table S6). The absorbed doses in red marrow varied in the range of 0.06–0.23 Gy for all dissociation constant K_D values and ligand amounts in all patients (Supplement, Table S6).

Effect of ligand amount. Tumours. For all combinations of association and dissociation rate k_{on} and k_{off} the highest absorbed dose was simulated for 32 nmol. The decrease in the tumour absorbed dose with increasing ligand amount was more pronounced in highly perfused tissue for high affinities (Fig. 2a,b).

Organs at risk. The absorbed dose in the kidneys in general decreased with increasing ligand amount. For dissociation constant $K_D < 1$ nM with an association rate $k_{on} = 0.1$ L/nmol/min the absorbed dose in kidneys decreased stronger compared to larger dissociation constant K_D values. The ligand amount had a minor effect on the absorbed dose in red marrow.

Effect of the internalization rate λ_{int}. Tumours. The effect of the internalization rate λ_{int} on the absorbed dose in the tumour varied considerably depending on the dissociation constant K_D and the ligand amount. For the dissociation constant $K_D = 1$ nM, the higher the internalization rate λ_{int} and ligand amount, the higher the absorbed dose in the tumour. The tumour absorbed dose increased by a factor of 2.0 ± 0.6 for the tumour lesions and 1.5 ± 0.6 for the tumour REST with an internalization rate $\lambda_{int} = 0.01\ min^{-1}$ compared to $\lambda_{int} = 0.001\ min^{-1}$ using a ligand amount of 32 nmol and the dissociation constant $K_D = 1$ nM ($k_{off} = 0.01\ min^{-1}$; $k_{on} = 0.01$ L/nmol/min). For affinities $K_D < 1$ nM and with an internalization rate $\lambda_{in} = 0.01\ min^{-1}$, a ligand amount > 32 nmol is required to achieve sufficient absorbed dose in the tumour. Conversely, for the internalization rate $\lambda_{int} = 0.0001\ min^{-1}$, a higher ligand amount led to a lower absorbed dose in the tumour (Supplement, Table S5).

Organs at risk. The absorbed dose in kidneys was higher for the internalization rate $\lambda_{int} = 0.01\ min^{-1}$ compared to $\lambda_{int} = 0.001\ min^{-1}$ for the all dissociation constant K_D using a ligand amount ≥ 32 nmol. The ligand amount affected the absorbed dose in the kidneys for the internalization rate $\lambda_{int} = 0.01\ min^{-1}$, however, only minor for the internalization rate $\lambda_{int} = 0.0001\ min^{-1}$. The absorbed dose in kidneys increased by a factor of 3.0 ± 0.3 with an internalization rate $\lambda_{int} = 0.01\ min^{-1}$ compared to the $\lambda_{int} = 0.001\ min^{-1}$ using ligand amount of 32 nmol and the dissociation constant $K_D = 1$ nM ($k_{off} = 0.01\ min^{-1}$; $k_{on} = 0.01$ L/nmol/min). The internalization rate λ_{int} only slightly affects the absorbed dose in red marrow regardless of the ligand amount (Supplement, Table S6).

Effects on tumour-to-kidneys absorbed dose ratio. The parameter values leading to the highest tumour-to-kidney absorbed dose ratio for different internalization rates λ_{int} (Table 2, Supplement, Table S7) were:

K_D[a] [nM]	k_{off}[b] [1/ min]	k_{on}[c] [L/ nmol/min]	Ligand amount [nmol]	Tumour-to-kidneys absorbed dose ratio of…					
				Tumour 1 and 2 for λ_{int}[d] of…			Tumour REST for λ_{int}[d] of…		
				0.01 [min^{-1}]	0.001 [min^{-1}]	0.0001 [min^{-1}]	0.01 [min^{-1}]	0.001 [min^{-1}]	0.0001 [min^{-1}]
0.01	0.0001	0.01	32	1.8 ± 1.3	2.3 ± 1.7	2.4 ± 1.7	1.3 ± 1.0	1.8 ± 1.4	2.2 ± 1.6
			100	2.2 ± 1.6	3.1 ± 2.3	3.1 ± 2.2	1.7 ± 1.4	3.1 ± 2.2	3.7 ± 2.6
			316	2.9 ± 2.1	3.5 ± 2.4	3.2 ± 2.1	2.7 ± 2.0	4.2 ± 2.8	4.2 ± 2.6
0.01	0.001	0.1	32	1.2 ± 0.9	2.2 ± 1.7	3.0 ± 2.3	0.8 ± 0.6	1.6 ± 1.4	2.7 ± 2.1
			100	1.8 ± 1.4	3.1 ± 2.3	3.4 ± 2.4	1.3 ± 1.1	3.1 ± 2.2	4.2 ± 3.0
			316	2.6 ± 1.9	3.4 ± 2.4	3.4 ± 2.3	2.3 ± 1.7	4.1 ± 2.8	4.6 ± 2.9
0.1	0.001	0.01	32	1.8 ± 1.3	2.6 ± 1.9	3.2 ± 2.3	1.4 ± 1.1	2.3 ± 1.7	3.6 ± 2.4
			100	2.2 ± 1.7	3.4 ± 2.5	3.5 ± 2.4	1.8 ± 1.4	3.5 ± 2.5	4.7 ± 3.1
			316	2.9 ± 2.1	3.6 ± 2.5	3.4 ± 2.3	2.7 ± 2.0	4.5 ± 3.0	4.8 ± 3.0
0.1	0.01	0.1	32	1.3 ± 1.0	2.8 ± 2.1	3.7 ± 2.6	0.9 ± 0.7	2.3 ± 1.8	4.2 ± 2.9
			100	1.9 ± 1.4	3.5 ± 2.6	**3.8 ± 2.6**	1.4 ± 1.2	3.7 ± 2.7	**5.1 ± 3.3**
			316	2.7 ± 1.9	3.7 ± 2.6	3.5 ± 2.4	2.4 ± 1.8	4.6 ± 3.1	5.0 ± 3.1
1	0.01	0.01	32	2.1 ± 1.6	3.4 ± 2.4	3.3 ± 2.2	1.7 ± 1.3	3.7 ± 2.5	4.3 ± 2.7
			100	2.5 ± 1.9	3.7 ± 2.6	3.3 ± 2.2	2.1 ± 1.6	4.4 ± 3.0	4.6 ± 2.9
			316	**3.0 ± 2.2**	3.7 ± 2.6	3.1 ± 2.0	**3.0 ± 2.1**	4.9 ± 3.2	4.4 ± 2.7
1	0.1	0.1	32	1.8 ± 1.4	3.5 ± 2.5	3.4 ± 2.3	1.4 ± 1.1	3.7 ± 2.6	4.4 ± 2.8
			100	2.3 ± 1.7	3.8 ± 2.7	3.3 ± 2.3	1.9 ± 1.5	4.5 ± 3.1	4.7 ± 2.9
			316	2.9 ± 2.1	**3.8 ± 2.6**	3.1 ± 2.0	2.8 ± 2.0	**4.9 ± 3.2**	4.4 ± 2.7

Table 2. The average of tumour-to-kidneys absorbed dose ratios considering different combinations k_{on} and k_{off}, ligand amounts and λ_{int}. [a]K_D = Dissociation constant ($K_D = k_{off}/k_{on}$); [b]k_{off} = Dissociation rate; [c]k_{on} = Association rate; [d]λ_{int} = Internalization rate. The values in bold are the maximum tumour-to-kidneys absorbed dose ratio.

- For $\lambda_{int} = 0.01\ min^{-1}$: $k_{on} = 0.01$ L/nmol/min, $k_{off} = 0.01\ min^{-1}$ with ligand amount of 316 nmol (ratio of 3.0 ± 2.2 for tumour lesions and 3.0 ± 2.1 for tumour REST),
- For $\lambda_{int} = 0.001\ min^{-1}$: $k_{on} = 0.1$ L/nmol/min, $k_{off} = 0.1\ min^{-1}$ with ligand amount of 316 nmol (ratio of 3.8 ± 2.6 for tumour lesions and 4.9 ± 3.2 for tumour REST) and
- For $\lambda_{int} = 0.0001\ min^{-1}$: $k_{on} = 0.1$ L/nmol/min, $k_{off} = 0.01\ min^{-1}$ with ligand amount of 100 nmol (ratio of 3.8 ± 2.6 for tumour lesions and 5.1 ± 3.3 for tumour REST).

Discussion

Currently used ^{68}Ga-labeled PSMA-specific ligands are effective in the detection of prostate cancer and ^{177}Lu-labeled ligands show great potential in the treatment of metastatic prostate cancer[5]. For theranostic approaches, efforts are directed to use the same molecule for imaging and therapy with different labelling. This is challenging, as the ligands must be optimized for both at the same time, high tumour activity concentration with low background for imaging and a high tumour-to-OAR absorbed doses ratio. The influence of affinity, internalization and ligand amount on these quantities was investigated in this work based on a validated PBPK model[15]. The influence of the total tumour volume (tumour sink effect) and normal tissue uptake might be different for varying affinities and ligand amounts[15,22]. Different release rates (factor 2) and perfusion (factor 10) of kidneys and of tumour tissue might affect imaging and therapy differently.

A suitable method to systematically and quantitatively investigate these effects in various tissues concurrently is PBPK modelling[14,15]. A simulation study was therefore conducted using a recently developed PBPK model[15] (based on data from PSMA-11 and PSMA I&T) for dissociation constant K_D values of 1, 0.1 and 0.01 nM (for each dissociation constant K_D two combinations of association and dissociation rates k_{on} and k_{off} were investigated), different internalization rates λ_{int} (0.01, 0.001 and 0.0001 min^{-1}) and ligand amounts (1–1000 nmol). The simulation study yielded three major findings:

(1) For imaging, ligands with $K_D < 1$ nM do not substantially increase the uptake in the tumour for commonly used ligand amounts compared to $K_D = 1$ nM as a) a considerable fraction is accumulated in highly perfused PSMA positive normal tissue and b) within one hour post injection differences might be considerably smaller compared to later time points. Therefore higher affinity might have a stronger effect on tumour activity concentration using nuclides with longer half-lives (^{18}F or even ^{64}Cu).
(2) For therapy, a decreasing K_D considerably increases the absorbed dose in all PSMA positive tissue. The differences are the more prominent the higher the perfusion of the tissue and the lower the amount of ligand applied. Higher ligand amounts improve tumour-to-OAR absorbed dose ratios but result in lower absolute values. These results suggest that it is important to optimize the ligand amount and the pertaining activity to maximize efficacy within the dose limits of the OARs.
(3) The simulations indicate that the combinations of association and dissociation rates k_{on} and k_{off} and ligand amount leading to the most favourable tumour-to-kidney ratios are:

a. For $\lambda_{int} = 0.01\ min^{-1}$: $k_{on} = 0.01$ L/nmol/min, $k_{off} = 0.01\ min^{-1}$ with ligand amount of 316 nmol
b. For $\lambda_{int} = 0.001\ min^{-1}$: $k_{on} = 0.1$ L/nmol/min, $k_{off} = 0.1\ min^{-1}$ with ligand amount of 316 nmol
c. For $\lambda_{int} = 0.0001\ min^{-1}$: $k_{on} = 0.1$ L/nmol/min, $k_{off} = 0.01\ min^{-1}$ with ligand amount of 100 nmol

The optimal ligand amounts are a consequence of the more rapid saturation of highly perfused PSMA positive normal tissue where PSMA-specific binding is the dominant mechanism in our model.

In our model, all physiologically and physically relevant mechanisms such as perfusion, diffusion, internalization, serum protein binding, PSMA-specific binding are included. The PBPK structure is a trade-off between parsimony and biological reality. For some mechanisms and parameter values detailed knowledge is not available and thus was lumped or fitted. For example, the number of PSMA receptors (which were estimated in previous work using PSMA-11 and PSMA I&T data[15]) represent effective values including all receptor subtypes. In addition, complex internalization and recycling of the ligand and receptor was modelled with one single rate constant as reported for antibody pharmacokinetic modelling[18,19]. Although we have recently developed a more complex model for internalization of ^{68}Ga-PSMA-11[21], further experiments with different ligands and nuclides are required to integrate this model into the whole-body PBPK structure. The same holds true for salivary gland uptake. More experiments are required to identify the nature of the uptake mechanisms.

The unspecific uptake is assumed to be low given that the specific uptake affinity is high and amino acids were given to block unspecific uptake. For the kidneys, unspecific uptake is reported (and included in the model) but further research is needed to find the non-specific uptake mechanism[23]. If the unspecific uptake is larger than assumed (not blocked by amino acids and not saturable for high ligand amounts) the ligand amount leading to the optimal tumour-to-kidney absorbed dose ratio will tend to be smaller.

In the PBPK model it is assumed that the ligand which is transported over the capillary wall is instantaneously diffused and has access to binding sites. This is a good approximation for flow-limited small molecules as PSMA-11 and PSMA I&T and a maximal, diffusion-limited association rate k_{on} of 10^8–$10^9\ M^{-1}{\cdot}s^{-1}$[7]. However, simply using association rate k_{on} from surface plasmon resonance measurements in this PBPK model might overestimate the actual binding because diffusion in the interstitial space is neglected.

In general, the translation of experimental values to *in vivo* systems is challenging. This is especially true for studies where K_D is derived at equilibrium whereas in the in vivo system with rapid clearance, binding equilibrium might not be reached. Our results nevertheless confirm that the separate experimental estimation of association and dissociation rates k_{on} and k_{off} and internalization rate λ_{int} is important[7].

Incorporating further information of cell and animal experiments in this whole-body PBPK model is ongoing. In addition, for imaging the effect of using nuclides with a different half-life will be investigated.

Conclusions

PBPK modelling proved to be a useful method for theoretically identifying ranges of ligand properties suitable for both imaging and therapy for theranostic applications. For the first time the interplay of important pharmacokinetic parameters for PSMA-specific ligands were investigated *in silico*. According to the simulations, association and dissociation rates that are optimal for therapy also lead to high tumour-to-background activity ratios for imaging. The results indicate that the properties of the ligands currently used are well chosen. Additionally, the simulations suggest that therapy might be considerably improved by choosing optimal activities *and* pertaining ligand amounts to achieve the highest tumour-to-OAR ratios. Further *in silico* and *in vivo* studies are required to verify the influence of the analysed parameters.

Data availability

All data generated or analysed during this study are included in this article.

Received: 1 October 2019; Accepted: 13 December 2019;
Published online: 27 December 2019

References

1. Verburg, F. A. *et al.* Nothing new under the nuclear sun: towards 80 years of theranostics in nuclear medicine. *Eur J Nucl Med Mol Imaging* **41**, 199–201, https://doi.org/10.1007/s00259-013-2609-2 (2014).
2. Herrmann, K., Larson, S. M. & Weber, W. A. Theranostic Concepts: More Than Just a Fashion Trend—Introduction and Overview. *J Nucl Med* **58**, 1S–2S, https://doi.org/10.2967/jnumed.117.199570 (2017).
3. Lütje, S. *et al.* PSMA Ligands for Radionuclide Imaging and Therapy of Prostate Cancer: Clinical Status. *Theranostics* **5**, 1388–1401, https://doi.org/10.7150/thno.13348 (2015).
4. Chatalic, K. L. *et al.* Towards Personalized Treatment of Prostate Cancer: PSMA I&T, a Promising Prostate-Specific Membrane Antigen-Targeted Theranostic Agent. *Theranostics* **6**, 849–861, https://doi.org/10.7150/thno.14744 (2016).
5. Scarpa, L. *et al.* The ^{68}Ga/^{177}Lu theragnostic concept in PSMA targeting of castration-resistant prostate cancer: correlation of SUV_{max} values and absorbed dose estimates. *Eur J Nucl Med Mol Imaging* **44**, 788–800, https://doi.org/10.1007/s00259-016-3609-9 (2017).
6. Barrett, J. A. *et al.* First-in-Man Evaluation of Two High-Affinity PSMA-Avid Small Molecules for Imaging Prostate Cancer. *J Nucl Med* **54**, 380–387, https://doi.org/10.2967/jnumed.112.111203 (2013).
7. Pan, A. C., Borhani, D. W., Dror, R. O. & Shaw, D. E. Molecular determinants of drug-receptor binding kinetics. *Drug Discov Today* **18**, 667–673, https://doi.org/10.1016/j.drudis.2013.02.007 (2013).
8. Wüstemann, T. *et al.* Design of Internalizing PSMA-specific Glu-ureido-based Radiotherapeuticals. *Theranostics* **6**, 1085–1095, https://doi.org/10.7150/thno.13448 (2016).
9. Kletting, P. *et al.* Optimized Peptide Amount and Activity for ^{90}Y-Labeled DOTATATE Therapy. *J. Nucl. Med.* **57**, 503–508, https://doi.org/10.2967/jnumed.115.164699 (2016).
10. Eckelman, W. C. In *Diagnostic nuclear medicine* Vol. 1 (eds. M. P. Sandler *et al.*) 255–262 (Williams & Wilkins).
11. Thomas, G. D. *et al.* Effect of dose, molecular size, affinity, and protein binding on tumor uptake of antibody or ligand: a biomathematical model. *Cancer Res* **49**, 3290–3296 (1989).

12. Cova, T. F. G. G., Bento, D. J. & Nunes, S. C. C. Computational Approaches in Theranostics: Mining and Predicting Cancer Data. *Pharmaceutics* **11**, 119, https://doi.org/10.3390/pharmaceutics11030119 (2019).
13. Zhang, L. *et al.* Tumor Chemo-Radiotherapy with Rod-Shaped and Spherical Gold Nano Probes: Shape and Active Targeting Both Matter. *Theranostics* **9**, 1893–1908, https://doi.org/10.7150/thno.30523 (2019).
14. Kletting, P. *et al.* Modeling and Predicting Tumor Response in Radioligand Therapy. *J Nucl Med* **60**, 65–70, https://doi.org/10.2967/jnumed.118.210377 (2019).
15. Begum, N. J. *et al.* The effect of total tumor volume on the biologically effective dose of tumor and kidneys for ^{177}Lu-labelled PSMA peptides. *J Nucl Med* **6**, 929–933, https://doi.org/10.2967/jnumed.117.203505 (2018).
16. Kletting, P. *et al.* Investigating the Effect of Ligand Amount and Injected Therapeutic Activity: A Simulation Study for ^{177}Lu-Labeled PSMA-Targeting Peptides. *PLoS ONE* **11**, e0162303, https://doi.org/10.1371/journal.pone.0162303 (2016).
17. Ferl, G. Z., Theil, F.-P. & Wong, H. Physiologically based pharmacokinetic models of small molecules and therapeutic antibodies: a mini-review on fundamental concepts and applications. *Biopharm Drug Dispos* **37**, 75–92, https://doi.org/10.1002/bdd.1994 (2016).
18. Thurber, G. M. & Weissleder, R. A Systems Approach for Tumor Pharmacokinetics. *PLoS ONE* **6**, e24696, https://doi.org/10.1371/journal.pone.0024696 (2011).
19. Fung, E. K. *et al.* Targeting of radiolabeled J591 antibody to PSMA-expressing tumors: optimization of imaging and therapy based on non-linear compartmental modeling. *EJNMMI Res* **6**, 7, https://doi.org/10.1186/s13550-016-0164-0 (2016).
20. Winter, G. *et al.* Comparative analysis of chelator-modified peptides for imaging of prostate carcinoma. *Eur J Nucl Med Mol Imaging* **41**(S414), P200 (2014).
21. Winter, G. *et al.* Modelling the internalisation process of prostate cancer cells for PSMA-specific ligands. *Nucl Med Biol* **72-73**, 20–25, https://doi.org/10.1016/j.nucmedbio.2019.05.003 (2019).
22. Jiménez-Franco, L. D., Kletting, P., Beer, A. J. & Glatting, G. Treatment planning algorithm for peptide receptor radionuclide therapy considering multiple tumor lesions and organs at risk. *Med Phys* **45**, 3516–3523, https://doi.org/10.1002/mp.13049 (2018).
23. Kratochwil, C. *et al.* PMPA for Nephroprotection in PSMA-Targeted Radionuclide Therapy of Prostate Cancer. *Journal of Nuclear Medicine* **56**, 293–298, https://doi.org/10.2967/jnumed.114.147181 (2015).

Acknowledgements

The authors gratefully acknowledge grants by "LPDP-Lembaga Pengelola Dana Pendidikan" (Indonesia Endowment Fund for Education, Ministry of Finance, Indonesia for NJB Ref: s-2512/LPDP.3/2016) and the "Deutsche Forschungsgemeinschaft" (German Research Foundation, KL2742/2-1, BE4393/1-1, GL236/11-1, SFB824 Project B11).

Author contributions

N.J.B.: Implemented the model, performed simulations, and wrote the manuscript. P.K.: Implemented the model, coordinated the investigations and wrote the manuscript. G.G., H.J.W., M.E., and A.J.B.: Evaluated the model and wrote the manuscript. All authors reviewed and approved the final manuscript.

Competing interests

The authors declare no competing interests.

Additional information

Supplementary information is available for this paper at https://doi.org/10.1038/s41598-019-56603-8.

Correspondence and requests for materials should be addressed to N.J.B.

Reprints and permissions information is available at www.nature.com/reprints.

Publisher's note Springer Nature remains neutral with regard to jurisdictional claims in published maps and institutional affiliations.

Open Access This article is licensed under a Creative Commons Attribution 4.0 International License, which permits use, sharing, adaptation, distribution and reproduction in any medium or format, as long as you give appropriate credit to the original author(s) and the source, provide a link to the Creative Commons license, and indicate if changes were made. The images or other third party material in this article are included in the article's Creative Commons license, unless indicated otherwise in a credit line to the material. If material is not included in the article's Creative Commons license and your intended use is not permitted by statutory regulation or exceeds the permitted use, you will need to obtain permission directly from the copyright holder. To view a copy of this license, visit http://creativecommons.org/licenses/by/4.0/.

© The Author(s) 2019

2.3 The effect of the radionuclide half-life on PET/CT imaging

2.3.1 Summary

PET/CT is becoming increasingly crucial for imaging tumor distribution, monitoring tumor progression, and selecting patients eligible for PSMA-RLT [70, 71]. In PET/CT imaging, efforts to improve accuracy aim to increase the tumor-to-background ratio. The ligand amount and properties can affect the tumor-to-background ratio and the radionuclide used. The effects of ligand amount for different ligand properties were studied in a previous publication [60]. The choice of the radionuclide in terms of half-life is also essential for different ligand affinities, as some studies indicate improvements when radioligands with longer half-lives than ^{68}Ga are used [72-75]. In this included article [61], the effects of different radionuclide half-lives on PET/CT imaging were investigated.

Tumor and background activity concentrations for PSMA targeting ligands were systematically studied for three radionuclides ^{68}Ga, ^{18}F, and ^{64}Cu (half-lives $t_{1/2}$ of 1.13 h, 1.83 h, and 12.7 h, respectively) and different ligand affinities (K_D of 1, 0.1 and 0.01 nM). Normalized activity concentration was calculated using equation (11) in the previous publication [60] for 1, 2, 3, 4, 8, 12, and 16 h after injection for all radionuclides. The highest activity concentration in the tumor was determined for each radionuclide and affinity. The results may provide information on the selection of radionuclides with suitable ligand affinity for PET/CT imaging. The 13 patients and PBPK models from the previous publication [60] were utilized. The association and dissociation rates k_{on} and k_{off} are part of the combinations studied in the last publication [60]. The affinities with dissociation constants K_D of 1, 0.1, and 0.01 nM and a ligand amount of 3 nmol were studied for all radionuclides. The included tumor lesions showed high uptake, and no significant overlap with other enriching tissue was selected, and other tumors were grouped as tumor REST.

The maximum activity concentrations in all tumors were reached for ^{68}Ga-PSMA at 1 h p. i. for all affinities and patients. For ^{18}F-PSMA, the maximum activity concentration was at 2 h p. i. for the dissociation constant K_D of 0.1-0.01 nM. For ^{18}F-PSMA with dissociation constant K_D=1 nM, the activity concentration in tumor lesions 1 h p. i. was slightly higher than 2 h p. i. For ^{64}Cu-PSMA and all affinities, the maximum tumor activity concentration averaged across all patients was 4 h p. i. However, for four patients, the activity concentrations at 8 h p. i. were slightly higher than at 4 h p. i. for higher affinities (K_D of 0.1-0.01 nM). The effect of longer half-lives on tumor activity concentrations was more pronounced at higher affinities. Compared with ^{68}Ga-PSMA (1 h p. i.), activity concentrations increased 1.3-fold for ^{18}F-PSMA (2 h p. i.) and all affinities for tumor lesions and tumor REST. Using ^{64}Cu-PSMA (4 h p. i.) compared with ^{68}Ga-PSMA (1 h p. i.), the improvements were in the range of 2.8- to 3.2-fold for tumor

lesions and 3.0- to 3.2-fold for tumor REST. Background activity concentration decreased with a longer half-life for all affinities. Compared with ^{68}Ga-PSMA (1 h p. i.), the decreases were in the range of 0.59- to 0.62-fold for ^{18}F-PSMA (2 h p. i.) and 0.50- to 0.62-fold for ^{64}Cu-PSMA (4 h p. i.). The results for all 13 patients are shown in the supplement of the article [61].

It can be concluded that longer half-lives of the radionuclide substantially increase activity concentration in the tumor (3-fold from ^{68}Ga to ^{64}Cu). The optimal imaging times for (^{68}Ga, ^{18}F, and ^{64}Cu) were about 1 h, 2 h, and 4 h p.i. for high-affinity ligands (dissociation constants K_D of 0.1–0.01 nM), respectively. The higher the affinity, the stronger the effect for radionuclides with longer half-lives, as high-affinity results in continuous ligand uptake into the tumor tissue. Therefore, the highest tumor-to-background ratio was achieved after four hours using ^{64}Cu-PSMA with high affinity.

2.3.2 Copyright and own contributions

This article [61] was published as

> **Begum NJ**, Glatting G, Eiber M, Beer AJ, Kletting P. An in silico study on the effect of the radionuclide half-life on PET/CT imaging with PSMA-targeting radioligands. Nuklearmedizin. 2021;60(1):33-37. DOI: 10.1055/a-1253-1535.

Copyright

Copyright © 2020 by Georg Thieme Verlag KG.
Reprinted (whole article) with permission.

Own contributions

I contributed to the conception and design of the study. I developed and implemented the MATLAB®/Simbiology script (version 2018a) and PBPK model for the radionuclide half-life and ligand simulations for PET/CT. I performed the data analyses and graphical representation of the results. I wrote, edited, and reviewed the manuscript with all co-authors.

An in silico study on the effect of the radionuclide half-life on PET/CT imaging with PSMA-targeting radioligands

Eine In-Silico-Studie über die Auswirkung der Halbwertszeit des Radionuklids auf die PET/CT-Bildgebung mit PSMA-adressierenden Radioliganden

Authors
Nusrat Jihan Begum[1], Gerhard Glatting[1], Matthias Eiber[2], Ambros J. Beer[3], Peter Kletting[1]

Affiliations
1 Medical Radiation Physics, Department of Nuclear Medicine, Ulm University, Ulm, Germany
2 Klinikum rechts der Isar, Department of Nuclear Medicine, Technical University of Munich School of Medicine, München, Germany
3 Department of Nuclear Medicine, Ulm University, Ulm, Germany

Key words
PET, half-life, PSMA Affinity, PBPK model

Schlüsselwörter
PET, Halbwertszeit, PSMA-Affinität, PBPK-Modell

received 10.06.2020
accepted 02.09.2020
published online 16.10.2020

Bibliography
Nuklearmedizin 2021; 60: 33–37
DOI 10.1055/a-1253-1535
ISSN 0029-5566
© 2020. Thieme. All rights reserved.
Georg Thieme Verlag KG, Rüdigerstraße 14, 70469 Stuttgart, Germany

Correspondence
Nusrat Jihan Begum
Department of Nuclear Medicine, Universität Ulm, Albert-Einstein-Allee 23, 89081 Ulm, Germany
Tel.: +49/7 31/50 06 13 72
nusrat.begum@uni-ulm.de

ABSTRACT

Aim The aim of this work was to systematically investigate the influence of the radionuclide half-life and affinity of prostate-specific membrane antigen (PSMA)-targeting ligands on the activity concentration for PET/CT imaging.

Methods A whole-body physiologically-based pharmacokinetic (PBPK) model with individually estimated parameters of 13 patients with metastatic castration-resistant prostate cancer (mCRPC) was used to simulate the pharmacokinetics of PSMA-targeting radioligands. The simulations were performed with ^{68}Ga (T1/2 = 1.13 h), ^{18}F (T1/2 = 1.83 h), ^{64}Cu (T1/2 = 12.7 h) and for different affinities (dissociation constants K_D of 1–0.01 nM) and a commonly used ligand amount of 3 nmol. The activity concentrations were calculated at 1, 2, 3, 4, 8, 12, and 16 h after injection.

Results The highest tumor uptake was achieved 1 h p. i. for ^{68}Ga-PSMA. For ^{18}F-PSMA, the highest tumor uptake was at 1 h p. i. and 2 h p.i for dissociation constants K_D = 1 nM and K_D = 0.1–0.01 nM, respectively. For ^{64}Cu-PSMA, the highest tumor uptake was at 4 h p. i. for dissociation constant K_D = 1 nM and at 4 h p. i. (9 patients) and 8 h p. i. (4 patients) for higher affinities. Compared to ^{68}Ga-PSMA (1 h p. i.), the activity concentrations in the tumor for ^{18}F-PSMA (2 h p. i.) increased maximum 1.3-fold with minor differences for all affinities. For ^{64}Cu-PSMA (4 h p. i.), the improvements were in the range of 2.8 to 3.2-fold for all affinities.

Conclusions The simulations indicate that the highest tumor-to-background ratio can be achieved after 4 hours in PET/CT using high-affinity ^{64}Cu-PSMA.

ZUSAMMENFASSUNG

Ziel Ziel dieser Arbeit war es, den Einfluss der Radionuklid-Halbwertszeit und der Affinität von Prostata-spezifischen Membranantigen (PSMA)-adressierten Radioliganden auf die Aktivitätskonzentration für die PET/CT-Bildgebung systematisch zu untersuchen.

Material und Methoden Ein physiologisch-basiertes pharmakokinetisches Ganzkörpermodell (PBPK) mit individuell geschätzten Parametern von 13 Patienten mit metastasiertem, kastrationsresistentem Prostatakarzinom (mCRPC) wurde verwendet, um die Pharmakokinetik von PSMA-adressierten Radioliganden zu simulieren. Die Simulationen wurden mit ^{68}Ga (T1/2 = 1,13 h), ^{18}F (T1/2 = 1,83 h), ^{64}Cu (T1/2 = 12,7 h) und für verschiedene Affinitäten (Dissoziationskonstanten K_D von 1–0,01 nM) und einer gebräuchlichen Ligandenmenge von 3 nmol durchgeführt. Die Aktivitätskonzentrationen wurden 1, 2, 3, 4, 8, 12 und 16 h nach Injektion berechnet.

Ergebnisse Die höchste Tumoraufnahme wurde 1 h p. i. für ^{68}Ga-PSMA erzielt. Für ^{18}F-PSMA war die höchste Tumoraufnahme 1 h p. i. für die Dissoziationskonstanten K_D = 1 nM

bzw. 2 h p. i. für K_D = 0,1–0,01 nM. Für ^{64}Cu-PSMA war die höchste Tumoraufnahme 4 h p. i. für die Dissoziationskonstante K_D = 1 nM und 4 h p. i. (9 Patienten) bzw. 8 h p. i. (4 Patienten) für höhere Affinitäten. Im Vergleich zu ^{68}Ga -PSMA (1 h p. i.) erhöhten sich die Aktivitätskonzentrationen im Tumor für ^{18}F-PSMA (2 h p. i.) maximal um das 1,3-fache mit geringen Unterschieden für alle Affinitäten. Bei ^{64}Cu-PSMA (4 Std. p. i.) lagen die Verbesserungen bei allen Affinitäten im Bereich des 2,8- bis 3,2-fachen.

Schlussfolgerung Die Simulationen zeigen, dass die höchste Tumor-to-Background-Ratio nach 4 Stunden im PET/CT mit hochaffinem ^{64}Cu-PSMA erreicht werden kann.

Introduction

In oncology the role of positron emission tomography (PET) imaging has become increasingly important for the visualization of tumour distribution, monitoring of disease progression and selection of the appropriate treatment [1]. In prostate cancer management, prostate-specific membrane antigen (PSMA) targeting ligands such as ^{68}Ga-PSMA-11 are successfully used in detecting tumour lesions of prostate cancer even at low PSA levels [2]. Novel PSMA-targeting PET tracers are developed by modifying molecular structures, linker design or different labeling, aiming at further increasing the tumour-to-background ratio. The effect of ligand amount for different affinities has already been determined for PSMA-targeting ligands using a physiologically-based pharmacokinetic (PBPK) model [3]. However, the influence of the half-life of the radionuclide on the activity concentration for different affinities is also of great interest as several studies show improvements using radioligands with longer half-lives than ^{68}Ga [4–7]. PBPK modeling and simulation is ideally suited to study different scenarios in a patient taking into account individual patient characteristics like filtration rate, total tumour volume or PSMA expression.

Therefore, the aim of this study was to systematically investigate the tumour and background activity concentration for PSMA-targeting ligands using a PBPK model for different 1) half-lives of the radionuclides (^{68}Ga, ^{18}F and ^{64}Cu) 2) affinities (K_D of 1, 0.1 and 0.01 nM) and 3) measurement times 1,2,3,4,8,12 and 16 h post injection.

Materials and Methods

Patients and PBPK Model

In this study, a recently published PBPK model for PSMA-targeting radioligands using Simbiology/MATLAB (MATLAB 2018a, The MathWorks, Inc) was employed [3, 8]. The patients and the model have been described in more detail elsewhere [8, 9]. In brief, the data of 13 patients (age 70 ± 6y) with metastatic castration-resistant prostate cancer (mCRPC) with a median total tumour volume of 236 ml (range 12–5800 ml) and a median PSA 133 ng/l (range 0.23–2.905 ng/l) were included. Pre- and peri-therapeutic imaging of the first cycle were performed. The patients received an average of 91 ± 5 nmol of ^{177}Lu-PSMA I&T RLT labelled with 7.3 ± 0.3 GBq of ^{177}Lu. The PET/CT measurement prior to therapy with ^{68}Ga-PSMA-11 (1.6 ± 0.3 nmol labelled with 115 ± 16 MBq) was employed to determine the activity concentration of tumour as well as normal tissues and the volume of single lesions and the total tumour volume. Data of two tumour lesions showing high uptake and no significant overlap with other PSMA-positive tissues were derived. For the estimation of the volume of a single tumour lesion, the volume of interest was determined by using an isocontour of 20 %–50 % SUV_{max}. The cumulated activity and volume of all tumour lesions other than the 2 tumour lesions (defined as tumour REST) were calculated by adding all lesions slice by slice using isocontours of 15 %–20 % SUV_{max}. To correct the overestimation or underestimation of tumour REST volume, a correction factor was estimated in the fitting process.

All relevant mechanisms such as perfusion, diffusion, plasma protein binding, PSMA-specific binding, internalization and physical decay are incorporated in the PBPK model. The pharmacokinetics of labelled and unlabelled ligands were modelled separately but are connected by physical decay and nonlinear binding. Tumour uptake was modelled with perfusion, diffusion, nonlinear binding to PSMA positive cells, internalisation and release of free nuclide. The background is defined as all compartments pertaining to muscle and fat. Important pharmacokinetic parameters (e. g. perfusion and receptor density) were fitted to the time-activity data of the 13 patients in a Bayesian framework by using simulation analysis and modelling software (SAAM II version 2.3 and PopKinetics, version 2.2, The Epsilon Group). The objective function contains the weighted sums of squares and a Bayesian term of the mean values and standard deviations of the fit parameters. The Rosenbrock integrator was selected. The variance model was set to "data based" and "absolute".

All procedures were performed in accordance with relevant guidelines and ethical standards. Informed consent form was obtained from all patients and the retrospective analysis of the data was approved by the institutional review board of the Technische Universität München.

Simulations

The simulations were performed for the virtual patients defined in section 2.1, i. e. the PBPK model together with the individually fitted parameters for every patient. The simulations were adapted with respect to 1) the radionuclides ^{68}Ga ($T_{1/2}$ = 1.13 h), ^{18}F ($T_{1/2}$ = 1.83 h), ^{64}Cu ($T_{1/2}$ = 12.7 h), and 2) the different affinities of the PSMA-targeting radioligands. The binding affinity is described by the dissociation constant K_D, the ratio of the dissociation rate k_{off} and association rate k_{on} ($K_D = k_{off}/k_{on}$). The affinity is the inverse of the dissociation constant K_D. The combinations of association and dissociation rates k_{on} and k_{off} are part of the combinations that have been investigated in the previous study [3]. The affinities with dissociation constants K_D of 1, 0.1 and 0.01 nM and a ligand amount of 3 nmol were investigated for all radionuclides (▶ **Table 1**).

▶ **Table 1** Activity concentrations in all tumours for different radionuclides, dissociation constants K_D with different combinations of association and dissociation rates k_{on} and k_{off} (with a ligand amount = 3 nmol) for all patients.

K_D[a] [nM]	k_{off}[b] [1/min]	k_{on}[c] [L/nmol/min]	Normalized activity concentration [%Injected Activity/l]							
			Tumour 1 and 2				Tumour REST			
			^{68}Ga	^{18}F	^{64}Cu		^{68}Ga	^{18}F	^{64}Cu	
			1 h p. i.	2 h p. i.	4 h p. i.	8 h p. i.	1 h p. i.	2 h p. i.	4 h p. i.	8 h p. i.
0.01	0.0001	0.01	17 ± 13	23 ± 17	55 ± 39	54 ± 37	7 ± 5	10 ± 7	24 ± 16	23 ± 15
0.1	0.001	0.01	17 ± 12	23 ± 16	54 ± 38	52 ± 35	7 ± 5	10 ± 7	23 ± 16	23 ± 15
1	0.01	0.01	16 ± 11	20 ± 14	44 ± 28	37 ± 22	7 ± 5	9 ± 6	21 ± 13	19 ± 11

[a] K_D – Dissociation constant ($K_D = k_{off}/k_{on}$); [b] k_{off} – Dissociation rate; [c] k_{on} – Association rate.

Normalized activity concentration and time points

The activity concentrations $A_i(t)$ were normalized for volume V_i and injected activity A_0 without decay correction. The normalized activity concentrations $c_i(t)$, where i – two tumour lesions, the tumour REST and the background (defined as muscle and fat in the model)

$$c_i(t) - \frac{A_i(t)}{A_0 \cdot V_i} \qquad (1)$$

were calculated for at 1, 2, 3, 4, 8, 12, and 16 h after injection for all radionuclides. The optimal acquisition time with the highest activity concentration in the tumour was determined for each radionuclide and affinity.

Results

Optimal time points for different radionuclides

The maximum activity concentrations in all tumours were obtained at 1 h p. i. for ^{68}Ga-labelled PSMA-targeting ligands (^{68}Ga-PSMA) for all affinities and patients. For ^{18}F-labelled PSMA-targeting ligands (^{18}F-PSMA), the maximum activity concentration was at 2 h p. i. for the dissociation constant K_D of 0.1–0.01 nM. For ^{18}F-PSMA with dissociation constant K_D – 1 nM the activity concentration in tumour lesions 1 h p. i. was slightly higher than 2 h p. i.. For ^{64}Cu-labelled PSMA-targeting ligands (^{64}Cu-PSMA) and for all affinities, the maximum tumour activity concentrations averaged over all patients was at 4 h p. i. (▶ **Table 1**). However, in 4 patients the activity concentrations at 8 h p. i. were slightly higher than at 4 h p. i. for higher affinities (K_D of 0.1–0.01 nM). As an example, in ▶ **Fig. 1** the optimal time point for a typical patient (Patient 5) is shown. For all 13 patients the results are provided in ▶ **Table 1**.

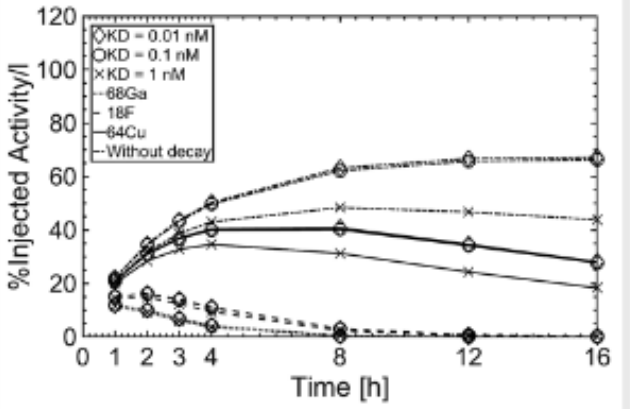

▶ **Fig. 1** The time-activity concentrations in a tumour lesion of patient 5 for 3 different radionuclides with ligand amount of 3 nmol. The maximum activity concentrations were reached at 1 h p. i. for ^{68}Ga and at 2 h p. i. for ^{18}F for all affinities. For this patient the maximum activity concentration of ^{64}Cu was at 4 h p. i. for the dissociation constant K_D = 1 nM. For ^{64}Cu with higher affinities (dissociation constants K_D of 0.1–0.01 nM), the activity concentration at 8 h p. i. was slightly higher than at 4 h p. i..

The effect of the half-life of the radionuclide for different affinities

The influence of the longer half-lives on the tumor activity concentration was more prominent for higher affinity (▶ **Table 1** for all 13 patients and ▶ **Fig. 2A, B** for a typical patient). Compared to ^{68}Ga-PSMA (1 h p. i.), the activity concentrations for ^{18}F-PSMA (2 h p. i.) and all affinities increased 1.3-fold for the tumour lesions and for the tumour REST. For ^{64}Cu-PSMA (4 h p. i.) compared to ^{68}Ga-PSMA (1 h p. i.), the improvements were in the range of 2.8 to 3.2-fold for the tumour lesions and 3.0 to 3.2-fold for the tumour REST (▶ **Table 1**).

The activity concentration in the background decreased with longer half-lives for all affinities. Compared to ^{68}Ga-PSMA (1 h p. i.), the decreases were in the range of 0.59 to 0.62-fold for ^{18}F-PSMA (2 h p. i.) and 0.50 to 0.62-fold for ^{64}Cu-PSMA (4 h p. i.) (▶ **Fig. 3**).

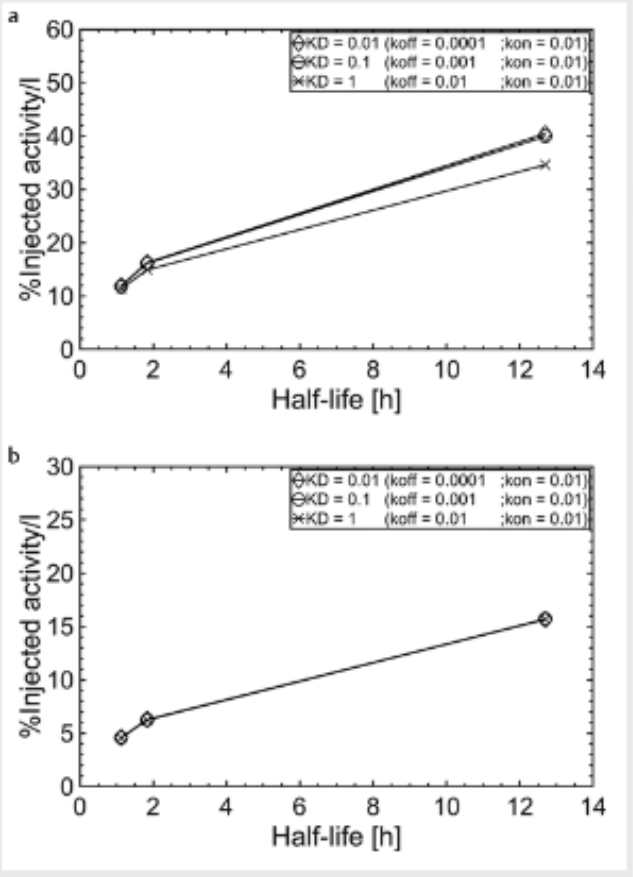

▶ **Fig. 2** Activity concentration of PSMA-targeting radioligand labelled with ^{68}Ga ($T_{1/2}$ = 1.13 h) at 1 h p.i., ^{18}F ($T_{1/2}$ = 1.83 h) at 2 h p.i. and ^{64}Cu ($T_{1/2}$ = 12.7 h) at 4 h p.i. for different affinities (dissociation constants K_D of 1–0.01 nM) and for **A** a tumour lesion (receptor density 33 nmol/l and perfusion 0.08 ml/g/min) and **B** tumour REST (receptor density 66 nmol/l and perfusion 0.04 ml/g/min) of patient 5.

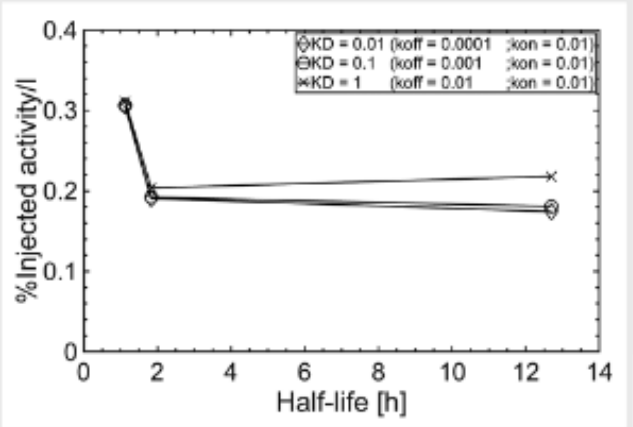

▶ **Fig. 3** . Activity concentration of PSMA-targeting radioligand labelled with ^{68}Ga ($T_{1/2}$ = 1.13 h) at 1 h p.i., ^{18}F ($T_{1/2}$ = 1.83 h) at 2 h p.i., ^{64}Cu ($T_{1/2}$ = 12.7 h) at 4 h p.i. for different affinities (dissociation constants K_D of 1–0.01 nM) and for background of patient 5.

Discussion

Several studies show improvements in tumour-to-background ratio at later imaging times compared to early imaging (3 h vs 1 h after injection) [4] indicating the effect of continuous 1) uptake of radioligand in the tumour, and 2) clearance from the background tissue. PBPK modeling [3, 8, 10] is ideally suited to investigate the influence of radionuclide and ligand properties.

In this simulation study, we systematically investigated the effect of the half-life (^{68}Ga, ^{18}F and ^{64}Cu) and affinities (dissociation constants K_D of 1–0.01 nM) on activity concentration in PET/CT imaging for PSMA-targeting ligands with the commonly used ligand amount (3 nmol). We found that

1. longer half-lives of the radionuclide substantially increase activity concentration in the tumour (3-fold from ^{68}Ga to ^{64}Cu)
2. the optimal imaging times for (^{68}Ga, ^{18}F and ^{64}Cu) were about 1 h, 2 h and 4 h after injection for high affinity ligands (dissociation constants K_D of 0.1–0.01 nM), respectively
3. the higher the affinity, the stronger the effect for radionuclides with longer half-lives, as high affinity results in continues uptake of ligand in tumour tissue (▶ **Fig. 1**). Our model shows (▶ **Fig. 1**) that uptake in tumour tissue peaks later than 8 h p.i. for an infinite half-life. This maximum depends on the affinity, the receptor density, the total tumour volumes, the perfusion and the filtration rate.

These results are in line with general reasoning and the literature. However, the predictions of our model especially for ^{64}Cu need to be further validated in an imaging study.

The current ^{18}F-labelled compounds have demonstrated good imaging performance and would potentially outperform the use of ^{68}Ga-labelled compounds in particular for detection of small tumour lesions. However, as the activity concentration in all PSMA-positive tissues is higher for longer half-lives, increased uptake in benign lesions [11] might lead to wrong interpretations. ^{64}Cu-labelled compounds have shown superior performance in particular in patients with low PSA level [6]. In addition, there is the possibility for a theranostic application using ^{67}Cu [12]. Clearly, the use of imaging agents with longer half-life and high affinity would lead to a higher activity concentration in the tumour. To facilitate higher activity concentration given its longer half-life, higher activities for ^{64}Cu need to be injected as the branching ratio is 5 fold lower for ^{64}Cu compared to ^{68}Ga.

This work might help to design comparative studies with available ^{18}F- or ^{64}Cu-labelled PSMA-targeting ligands and in the development of novel radiopharmaceuticals.

Conclusions

PBPK modeling allowed to quantify potential improvements using nuclides with longer half-life for imaging with the pertaining optimal measurements time points. The highest activity concentration in the tumour with the lowest background activity would probably be achieved after 4 hours in PET/CT using typical ligand amounts of high-affinity ^{64}Cu-labelled PSMA-targeting ligands.

Funding

Deutsche Forschungsgemeinschaft (BE4393/1-1, GL236/11-1, KL2742/2-1), LPDP-Lembaga Pengelola Dana Pendidikan (s-2512/LPDP.3/2016)

Conflict of Interest

The authors declare that they have no conflict of interest.

Acknowledgements

The work was supported by "LPDP-Lembaga Pengelola Dana Pendidikan" (Indonesia Endowment Fund for Education, Ministry of Finance, Indonesia for NJB Ref: s-2512/LPDP.3/2016) and the "Deutsche Forschungsgemeinschaft" (German Research Foundation, KL2742/2–1, BE4393/1–1, GL236/11–1, SFB824 Project B11).

References

[1] Perera M, Papa N, Christidis D et al. Sensitivity, Specificity, and Predictors of Positive ^{68}Ga-Prostate-specific Membrane Antigen Positron Emission Tomography in Advanced Prostate Cancer: A Systematic Review and Meta-analysis. Eur Urol 2016; 70: 926–937. doi:10.1016/j.eururo.2016.06.021

[2] Heinzel A, Boghos D, Mottaghy FM et al. (68)Ga-PSMA PET/CT for monitoring response to ^{177}Lu-PSMA-617 radioligand therapy in patients with metastatic castration-resistant prostate cancer. Eur J Nucl Med Mol Imaging 2019; 46: 1054–1062. doi:10.1007/s00259-019-4258-6

[3] Begum NJ, Glatting G, Wester HJ et al. The effect of ligand amount, affinity and internalization on PSMA-targeted imaging and therapy: A simulation study using a PBPK model. Sci Rep 2019; 9: 20041. doi:10.1038/s41598-019-56603-8

[4] Rahbar K, Afshar-Oromieh A, Bogemann M et al. ^{18}F-PSMA-1007 PET/CT at 60 and 120 minutes in patients with prostate cancer: biodistribution, tumour detection and activity kinetics. Eur J Nucl Med Mol Imaging 2018; 45: 1329–1334. doi:10.1007/s00259-018-3989-0

[5] Afshar-Oromieh A, Sattler LP, Mier W et al. The Clinical Impact of Additional Late PET/CT Imaging with ^{68}Ga-PSMA-11 (HBED-CC) in the Diagnosis of Prostate Cancer. J Nucl Med 2017; 58: 750–755. doi:10.2967/jnumed.116.183483

[6] Cantiello F, Crocerossa F, Russo GI et al. Comparison Between (64)Cu-PSMA-617 PET/CT and ^{18}F-Choline PET/CT Imaging in Early Diagnosis of Prostate Cancer Biochemical Recurrence. Clin Genitourin Cancer 2018; 16: 385–391. doi:10.1016/j.clgc.2018.05.014

[7] Afshar-Oromieh A, Hetzheim H, Kubler W et al. Radiation dosimetry of ^{68}Ga-PSMA-11 (HBED-CC) and preliminary evaluation of optimal imaging timing. Eur J Nucl Med Mol Imaging 2016; 43: 1611–1620. doi:10.1007/s00259-016-3419-0

[8] Begum NJ, Thieme A, Eberhardt N et al. The Effect of Total Tumor Volume on the Biologically Effective Dose to Tumor and Kidneys for ^{177}Lu-Labeled PSMA Peptides. J Nucl Med 2018; 59: 929–933. doi:10.2967/jnumed.117.203505

[9] Kletting P, Schuchardt C, Kulkarni HR et al. Investigating the Effect of Ligand Amount and Injected Therapeutic Activity: A Simulation Study for ^{177}Lu-Labeled PSMA-Targeting Peptides. PLoS One 2016; 11: e0162303. doi:10.1371/journal.pone.0162303

[10] Kletting P, Thieme A, Eberhardt N et al. Modeling and Predicting Tumor Response in Radioligand Therapy. J Nucl Med 2019; 60: 65–70. doi:10.2967/jnumed.118.210377

[11] Rauscher I, Krönke M, König M et al. Matched-Pair Comparison of ^{68}Ga-PSMA-11 PET/CT and ^{18}F-PSMA-1007 PET/CT: Frequency of Pitfalls and Detection Efficacy in Biochemical Recurrence After Radical Prostatectomy. J Nucl Med 2020; 61: 51–57. doi:10.2967/jnumed.119.229187

[12] Carlos Dos Santos J, Beijer B, Bauder-Wust U et al. Development of Novel PSMA Ligands for Imaging and Therapy with Copper Isotopes. J Nucl Med 2020; 61: 70–79. doi:10.2967/jnumed.119.229054

3 Discussion

The importance of a *priori* knowledge for optimizing imaging and therapy of radioligands targeting PSMA has been investigated. The variability in absorbed dose between patients may be due to the sink effect. The tumor sink effect describes the pharmacokinetic effects of a high tumor burden [8]. It can lead to lower activity concentrations in healthy tissues [9] but also in the tumor, resulting in underdosing in the tumor. The choice of ligand properties is crucial as they affect pharmacokinetics. Therefore, in theranostics, the same or similar ligands with different labeling are used for imaging and therapy to avoid pharmacokinetic changes. Optimization in theranostics is challenging because ligands must be matched to both a high tumor activity concentration and minimal imaging background and a high tumor to OAR absorbed dose ratio [2, 45]. Different amounts of ligands used between PET/CT imaging and therapy could affect ligand affinities. In addition, several studies have shown that longer imaging times (at 3 h p.i.) result in better tumor-to-background ratios than earlier imaging times (at 1 h p.i.) [75]. This demonstrates the effect of continuous uptake of radioligand into the tumor and clearance from the background tissue.

PBPK modeling is ideally suited to systematically and quantitatively investigate the important parameters for optimizing imaging and therapy of PSMA-targeted radioligands. Important information about the individual patient, the ligand properties, the radionuclide, and the different ligand amounts used in ^{68}Ga-PSMA-11 PET and ^{177}Lu-PSMA I&T therapy were included in the PBPK model. With the PBPK model, studies were performed by changing the parameters of total tumor volume (TTV), ligand properties, including ligand amount, and radionuclide half-life. The main findings of the thesis are presented below:

1. TTV strongly affects the absorbed dose and BED in tumors and OAR. Patients with a high tumor burden can receive a higher number of activity and amount of ligands without exceeding the tolerable BED for the organs at risk so that the therapeutic effect can be optimized.
2. The higher the ligand affinity, the more critical the optimal amount of ligand was chosen.
3. The highest tumor-to-background ratio can be achieved after 4 h in PET/CT using commonly used ligand amounts of high-affinity ^{64}Cu-PSMA-targeting ligands.

Effect of TTV, administered activity, and amount of ligand on BEDs

The fitted parameters were within a physiologically reasonable range. Based on fitted parameters (e.g., receptor densities), different TTVs from 0.1-10 L were simulated. BED for kidneys and tumors decreased significantly with increasing TTV. The results are consistent with a study by Gaertner et al., which showed that the SUV_{mean} in OAR decreased between patients with low and high tumor burdens [9]. The dose absorbed in the bone marrow can be determined from the dose absorbed in the blood and the whole body. Thus, higher total body retention was responsible for increasing red bone marrow BED with increasing tumor burden. The relevance of the amount of peptide about the number of receptors is reported in ^{177}Lu-DOTA-octreotate therapy [76]. The BED ratio between tumor and kidney decreased slightly, increasing tumor burden with the same activity and amount of ligand. This was due to a reduced saturation effect of the kidney with the less accessible ligand. However, increasing the amount of ligand with adapted activity can improve the tumor to kidney BED ratio. It has been shown that there is an optimal tumor to OAR ratio for each patient, e.g., for antibodies [77-79] and peptides [16, 48, 49]. In RLT, the kidneys are the dose-limiting organ. The kidneys secrete radioligands that are reabsorbed and partially retained in the proximal tubules, resulting in dose-limiting nephrotoxicity. Therefore, a maximum kidneys BED of 5 $Gy_{2.5}$ for one cycle was established to determine the optimal activity and amount of ligand for an individual patient using an algorithm developed by Kletting et al. [48]. The tumor radiobiologic parameters from Fowler et al. [43] were used, although the actual range [80] and its applicability to RLT are still controversial. Therefore, the absorbed doses and BED for an α/β of 1.8 reported by Dearnaley et al. [80] are also provided. The tumor BED had a maximum deviation of 5% when the range of α/β values of Fowler and Dearnaley et al. was used (Supplement of the reference [59] and Appendix A.1).

The results suggest optimizing the ratio of tumor to kidney BED for a given limited kidney BED could safely increase tumor BED using individualized dosimetry based on our PBPK model, especially in patients with a high tumor burden. Because the number of possible cycles may be limited by bone marrow BED or salivary gland BED, an overall optimization strategy that considers all OARs and treatment effects is preferable. As a result, future clinical management could be modified by individualizing activity and ligand amounts before the first cycle of therapy. Individualized adjustment is also crucial for patients with a low tumor burden in early disease stages. The optimal combination of activity and ligand amount may differ significantly from patients with large tumor burdens.

Effect of ligand amounts, affinities, and internalization on PSMA-targeted imaging and therapy

On imaging, ligands with a K_D of less than 1 nM do not significantly increase tumor uptake compared with a K_D of 1 nM for the amounts of ligand commonly used. A substantial fraction accumulates in highly perfused PSMA-positive normal tissue, and differences within one-hour post-injection are likely to be much smaller than differences at a later time. As a result, higher affinity may significantly affect tumor activity concentrations for nuclides with longer half-lives (^{18}F or ^{64}Cu). A lower K_D significantly increases the absorbed dose in all PSMA-positive tissues in therapy. The higher the tissue perfusion and the lower the amount of ligand applied, the more pronounced the differences. Higher amounts of ligand improve the ratio of absorbed dose between tumor and OAR, whereas the absolute values decrease. These results suggest that to enhance efficacy within OAR dose limits, thus it is critical to optimize the amount of ligand to be administered and the associated activity. The optimal ligand amounts result from the faster saturation of the highly perfused PSMA-positive normal tissue in our model because PSMA-specific binding is the primary mechanism.

All physiologically and physically relevant mechanisms are represented in our models, such as perfusion, diffusion, internalization, serum protein binding, and PSMA-specific binding are included in our models. The PBPK framework balances biological realism with simplicity. Some mechanisms and parameter values were lumped or adjusted because complete knowledge was unavailable. For example, the number of PSMA receptors (previously calculated using PSMA-11 and PSMA-I&T data) [59] represents practical values encompassing all receptor subtypes. Furthermore, as in pharmacokinetic antibody modeling [81, 82], the complex internalization and recycling of ligand and receptor were modeled with a single rate constant. Although we have established a more detailed model for ^{68}Ga-PSMA-11 [53], further studies with different ligands and nuclides are needed to fully integrate this model into the whole-body PBPK framework. The same applies to uptake by the salivary glands. The nature of the uptake mechanisms needs further investigation. Since the specific uptake affinity is high and amino acids have been provided to prevent non-specific uptake, non-specific uptake is estimated to be low. Unspecific uptake in the kidneys is included in the model, but further studies are needed to determine the mechanism of unspecific uptake. If unspecific uptake is more significant than expected (not inhibited by amino acids and not saturable at high ligand doses), the amount of ligand required to achieve the ideal tumor-to-kidney absorbed dose ratio will be lower. Ligand delivered across the capillary wall is assumed to diffuse immediately and access binding sites in the PBPK model. This is a reasonable estimate for flow-limited small molecules such as

PSMA-11 and PSMA I&T, and a maximum diffusion-limited association rate k_{on} of 10^8 –10^9 $M^{-1} \cdot s^{-17}$. However, because diffusion in the interstitial region is neglected in this PBPK model, simply using the association rate k_{on} from surface plasmon resonance, data may overestimate the actual binding.

It is challenging to extrapolate experimental results to in *vivo* systems. This is especially true for studies where dissociation constant K_D is calculated at equilibrium. However, binding equilibrium may not be reached in the in vivo system due to fast clearance. However, our results highlight the importance of separately estimating the association and dissociation rates k_{on} and k_{off} and the internalization rate λ_{int} [68]. In addition, the effect of using nuclides with different half-lives on imaging needs to be investigated, which will be addressed in further study.

Effect of radionuclide half-lives, ligand affinities, and measurement time points after injection on the tumor and background activity concentration

The model shows that uptake into tumor tissue peaks later than 8 h p. i. at an infinite half-life. This maximum depends on affinity, receptor density, total tumor volume, perfusion, and filtration rate. These results are consistent with general considerations and the literature. However, the predictions of our model, especially for ^{64}Cu, need to be further validated in an imaging study.

The current ^{18}F-labeled compounds have shown good imaging performance and would potentially outperform the use of ^{68}Ga-labeled compounds, especially in detecting small tumor lesions. However, since activity concentration is higher in all PSMA-positive tissues at longer half-lives, increased uptake in benign lesions [83] could lead to misinterpretation. ^{64}Cu-labeled compounds have shown superior performance, particularly in patients with low PSA levels [74]. In addition, there is the possibility of the theranostic application of ^{67}Cu [84]. The use of contrast agents with a longer half-life and high affinity would result in higher activity concentrations in the tumor. To allow for higher activity concentration given the longer half-life, higher activities for ^{64}Cu need to be injected because the branching ratio for ^{64}Cu is fivefold lower than ^{68}Ga.

Limitations

The number of patients included in this work is small. However, the patient cohort represents the high variability of individual parameters, e.g., tumor parameters were widely distributed, e.g., total tumor volume of 0.02-5 L (median: 0.4 L), receptor densities of 4-124 nmol/L (median: 50 nmol/L), blood flow of 0.02-1.6 mL/min/g (median: 0.2 mL/min/g). The PBPK model also accounts for various imaging and therapeutic parameters, such as ligand amounts, affinities, and radionuclide half-lives of PET and therapeutic agents.

In the PBPK model, the kidneys, salivary and lacrimal glands are the limiting organs. Parameter values such as receptor density and flux for the salivary and lacrimal glands were taken from the literature because planar imaging is inaccurate for these tiny organs. In addition, the differences in salivary and lacrimal gland uptake do not significantly affect tumor and kidney biokinetics. However, it is possible to predict salivary and lacrimal gland parameters more accurately using SPECT/CT imaging during therapy. Further in *silico* and in *vivo* studies are needed to confirm the effects of the parameters studied.

Outlook

Due to its complexity and high time and resource requirements, individual treatment planning based on dosimetry is often not performed. As a result, a standardized treatment approach continues to be used. However, dosimetry-based individualized treatment planning could potentially improve further and optimize the therapeutic efficacy of RLT. The results indicate that it is essential to consider inter-patient variability when determining the activity and ligand amount to be administered to avoid under-or over-treatment. In addition, the use of a PBPK model in individualized treatment planning offers the opportunity to simplify the clinical workflow and improve the prediction of biodistribution in therapy. PBPK modeling provides insights into the pharmacokinetics of PSMA-specific ligands and allows quantification of potential imaging and therapeutic improvements for PSMA-targeted ligands. This information could also be helpful for the development of new agents for imaging and therapy of PSMA-specific radioligands.

Further studies with quantitative 3D imaging during therapy are needed to accurately determine salivary and lacrimal gland parameters. In addition, improved red bone marrow dosimetry models are required to quantify the dose to the red bone marrow accurately. The PBPK model and algorithm can be easily modified to account for multiple OARs or marginal doses.

4 Abstract

Radioligand therapy (RLT) targeting prostate-specific membrane antigen (PSMA) is a promising systemic treatment for metastatic castration-resistant prostate cancer (mCRPC) when conventional treatments are no longer an option. Although PSMA-targeted RLT is a viable treatment option for mCRPC, the effect of therapy varies from patient to patient. The therapeutic effect is generally determined by the absorbed dose and absorbed dose rate in tumors and normal organs, which depend on the choice of radionuclide, ligand properties, and individual patients' biokinetics. Measurement before therapy, e.g., PET/CT, is becoming increasingly essential to accurately estimate the absorbed dose in therapy. Varying ligand amounts, ligand properties, and radionuclides can affect the efficacy of PSMA-targeted imaging and therapy. Inter-patient variability, such as total tumor volume (TTV), must also be considered as it affects the biodistribution of radioligand in the patient. A more detailed understanding of the important parameters affecting imaging and therapy of PSMA-targeted RLT is needed. Therefore, this thesis aimed to investigate 1) the effect of TTV on the biologically effective dose (BED) to tumors and organs at risk (OAR), 2) the effects of ligand amounts, affinities, and internalization on imaging and therapy, and 3) the effects of radionuclide half-lives, ligand affinities, and measurement time points after injection on tumor and background activity.

For this purpose, 13 patients with mCRPC treated with ^{177}Lu-PSMA I&T were included. A physiologically-based whole-body pharmacokinetic (PBPK) model for PSMA-specific ligands was developed based on PSMA-11 and PSMA I&T and implemented in MATLAB® software packages (Simulink and Simbiology). The PBPK model was fitted to biokinetics data of 13 patients to estimate individual patient parameters. The PBPK model with individually estimated parameters (virtual patients) was utilized for the simulations with MATLAB®. The effect of TTV on absorbed dose and BED was investigated by simulating TTVs of 0.1-10 L for tumors and OAR. The activity and amount of ligand to be administered leading to an optimal tumor to kidney ratio were also investigated. The effects of ligand properties on PET/CT imaging and therapy were studied for ligand amounts (1-1000 nmol), association rates k_{on} (0.1-0.01 L/nmol/min), dissociation rates k_{off} (0.1-0.0001 min^{-1}), and internalization rates λ_{int} (0.01-0.0001 min^{-1}). The activity was normalized to volume and administered activity for imaging (^{68}Ga-PSMA at 1 h). The absorbed dose of 7.3 GBq ^{177}Lu-PSMA was calculated for therapy. Three radionuclides with different half-lives ^{68}Ga ($t_{1/2}$ = 1.13 h), ^{18}F ($t_{1/2}$ = 1.83 h), and ^{64}Cu

($t_{1/2}$ = 12.7 h) were simulated for different affinities (dissociation constants K_D of 1-0.01 nM). A common ligand amount of 3 nmol investigated the effects of radionuclide half-life and ligand affinity on activity concentration in PET/CT imaging. Activity concentrations were calculated at various time points (1, 2, 3, 4, 8, 12, and 16 h p.i.).

Simulated BEDs decreased in tumor lesion (58% ± 18%), kidneys (58% ± 17%), parotid glands (59% ± 16%), and submandibular glands (59% ± 16%) when TTV was increased from 0.3 to 3 L. BED for red bone marrow increased (185% ± 29%). The optimal ligand amount and activity were 273 ± 136 nmol and 10.4 ± 4.4 GBq, respectively, in patients with a TTV greater than 0.3 L. The effects of ligand properties on therapy were greater than those of imaging. The combination of ligand properties (k_{on} = 0.1 L/nmol/min, and k_{off} = 0.01 min^{-1}) resulted in the highest tumor uptake for imaging using commonly used ligand amounts (1-10 nmol). The higher the internalization rate, the higher ligand amount is required for an appropriate tumor-to-kidney ratio in therapy. Choosing the optimal amount of ligand became more crucial as the affinity increased. The maximum tumor uptake was achieved 1 h p. i. for ^{68}Ga-PSMA in a simulated study on the effect of the radioactive half-life on PET/CT imaging for varied ligand affinities. The maximum tumor uptake was at 1 h p. i. and 2 h p. i. for ^{18}F-PSMA, for dissociation constants K_D = 1 nM and K_D = 0.1-0.01 nM, respectively. The maximum tumor uptake for ^{64}Cu-PSMA was observed at 4 h p.i. for dissociation constant K_D = 1 nM, and at 4 h p. i. (9 patients) and 8 h p. i. (4 patients) for higher affinities. Activity concentrations in the tumor increased 1.3-fold for ^{18}F-PSMA (2 h p.i.) compared to ^{68}Ga-PSMA (1 h p.i.), with insignificant differences for all affinities. The improvements in ^{64}Cu-PSMA (4 h p. i.) were 2.8 to 3.2-fold for all affinities.

The presented results provide essential information to optimize imaging and therapy of PSMA-targeted RLT. It can be concluded that:

1. The total tumor volume strongly influences the absorbed dose and BED in tumors and OAR. Patients with a high tumor burden can receive more activities and ligands without exceeding the tolerable BED for the OAR to improve the therapeutic effect.
2. The higher the ligand affinity, the more important the optimal amount of ligand was chosen.
3. The highest tumor-to-background ratio can be achieved after 4 h in PET/CT with the commonly used ligand amounts of the high-affinity ^{64}Cu-PSMA target ligands.

5 References

1. Bray F, Ferlay J, Soerjomataram I, Siegel RL, Torre LA, Jemal A. Global cancer statistics 2018: GLOBOCAN estimates of incidence and mortality worldwide for 36 cancers in 185 countries. CA Cancer J Clin. 2018;68(6):394-424.
2. Eiber M, Fendler WP, Rowe SP, Calais J, Hofman MS, Maurer T, Schwarzenboeck SM, Kratowchil C, Herrmann K, Giesel FL. Prostate-Specific Membrane Antigen Ligands for Imaging and Therapy. J Nucl Med. 2017;58(Suppl 2):67s-76s.
3. Silver DA, Pellicer I, Fair WR, Heston WD, Cordon-Cardo C. Prostate-specific membrane antigen expression in normal and malignant human tissues. Clin Cancer Res. 1997;3(1):81-5.
4. Glatting G, Bardies M, Lassmann M. Treatment planning in molecular radiotherapy. Z Med Phys. 2013;23(4):262-9.
5. Dehbi HM, Mallick U, Wadsley J, Newbold K, Harmer C, Hackshaw A. Recurrence after low-dose radioiodine ablation and recombinant human thyroid-stimulating hormone for differentiated thyroid cancer (HiLo): long-term results of an open-label, non-inferiority randomised controlled trial. Lancet Diabetes Endocrinol. 2019;7(1):44-51.
6. Matthay KK, Weiss B, Villablanca JG, Maris JM, Yanik GA, Dubois SG, Stubbs J, Groshen S, Tsao-Wei D, Hawkins R, Jackson H, Goodarzian F, Daldrup-Link H, Panigrahy A, Towbin A, Shimada H, Barrett J, Lafrance N, Babich J. Dose escalation study of no-carrier-added ^{131}I-metaiodobenzylguanidine for relapsed or refractory neuroblastoma: new approaches to neuroblastoma therapy consortium trial. J Nucl Med. 2012;53(7):1155-63.
7. Strosberg J, El-Haddad G, Wolin E, Hendifar A, Yao J, Chasen B, Mittra E, Kunz PL, Kulke MH, Jacene H, Bushnell D, O'Dorisio TM, Baum RP, Kulkarni HR, Caplin M, Lebtahi R, Hobday T, Delpassand E, Van Cutsem E, Benson A, Srirajaskanthan R, Pavel M, Mora J, Berlin J, Grande E, Reed N, Seregni E, Öberg K, Lopera Sierra M, Santoro P, Thevenet T, Erion JL, Ruszniewski P, Kwekkeboom D, Krenning E. Phase 3 Trial of (177)Lu-Dotatate for Midgut Neuroendocrine Tumors. N Engl J Med. 2017;376(2):125-35.
8. Beauregard JM, Hofman MS, Kong G, Hicks RJ. The tumour sink effect on the biodistribution of ^{68}Ga-DOTA-octreotate: implications for peptide receptor radionuclide therapy. Eur J Nucl Med Mol Imaging. 2012;39(1):50-6.
9. Gaertner FC, Halabi K, Ahmadzadehfar H, Kürpig S, Eppard E, Kotsikopoulos C, Liakos N, Bundschuh RA, Strunk H, Essler M. Uptake of PSMA-ligands in normal tissues is dependent on tumor load in patients with prostate cancer. Oncotarget. 2017;8(33):55094-103.
10. Hardiansyah D, Maass C, Attarwala AA, Müller B, Kletting P, Mottaghy FM, Glatting G. The role of patient-based treatment planning in peptide receptor radionuclide therapy. Eur J Nucl Med Mol Imaging. 2016;43(5):871-80.
11. Lassmann M, Chiesa C, Flux G, Bardiès M. EANM Dosimetry Committee guidance document: good practice of clinical dosimetry reporting. Eur J Nucl Med Mol Imaging. 2011;38(1):192-200.
12. Strigari L, Konijnenberg M, Chiesa C, Bardies M, Du Y, Gleisner KS, Lassmann M, Flux G. The evidence base for the use of internal dosimetry in the clinical practice of molecular radiotherapy. Eur J Nucl Med Mol Imaging. 2014;41(10):1976-88.
13. Delker A, Fendler WP, Kratochwil C, Brunegraf A, Gosewisch A, Gildehaus FJ, Tritschler S, Stief CG, Kopka K, Haberkorn U, Bartenstein P, Boning G. Dosimetry for ^{177}Lu-DKFZ-PSMA-617: a new radiopharmaceutical for the treatment of metastatic prostate cancer. Eur J Nucl Med Mol Imaging. 2016;43(1):42-51.

14. Graves SA, Hobbs RF. Dosimetry for Optimized, Personalized Radiopharmaceutical Therapy. Semin Radiat Oncol. 2021;31(1):37-44.
15. Kabasakal L, AbuQbeitah M, Aygun A, Yeyin N, Ocak M, Demirci E, Toklu T. Pre-therapeutic dosimetry of normal organs and tissues of ^{177}Lu-PSMA-617 prostate-specific membrane antigen (PSMA) inhibitor in patients with castration-resistant prostate cancer. Eur J Nucl Med Mol Imaging. 2015;42(13):1976-83.
16. Kletting P, Schuchardt C, Kulkarni HR, Shahinfar M, Singh A, Glatting G, Baum RP, Beer AJ. Investigating the Effect of Ligand Amount and Injected Therapeutic Activity: A Simulation Study for ^{177}Lu-Labeled PSMA-Targeting Peptides. PLoS One. 2016;11(9):e0162303.
17. Scarpa L, Buxbaum S, Kendler D, Fink K, Bektic J, Gruber L, Decristoforo C, Uprimny C, Lukas P, Horninger W, Virgolini I. The ^{68}Ga/^{177}Lu theragnostic concept in PSMA targeting of castration-resistant prostate cancer: correlation of SUVmax values and absorbed dose estimates. Eur J Nucl Med Mol Imaging. 2017;44(5):788-800.
18. Capala J, Graves SA, Scott A, Sgouros G, James SS, Zanzonico P, Zimmerman BE. Dosimetry for Radiopharmaceutical Therapy: Current Practices and Commercial Resources. J Nucl Med. 2021;62(Suppl 3):3s-11s.
19. Bolch WE, Eckerman KF, Sgouros G, Thomas SR. MIRD pamphlet No. 21: a generalized schema for radiopharmaceutical dosimetry--standardization of nomenclature. J Nucl Med. 2009;50(3):477-84.
20. He B, Du Y, Segars WP, Wahl RL, Sgouros G, Jacene H, Frey EC. Evaluation of quantitative imaging methods for organ activity and residence time estimation using a population of phantoms having realistic variations in anatomy and uptake. Med Phys. 2009;36(2):612-9.
21. Dewaraja YK, Frey EC, Sgouros G, Brill AB, Roberson P, Zanzonico PB, Ljungberg M. MIRD pamphlet No. 23: quantitative SPECT for patient-specific 3-dimensional dosimetry in internal radionuclide therapy. J Nucl Med. 2012;53(8):1310-25.
22. Zimmerman BE, Grošev D, Buvat I, Coca Pérez MA, Frey EC, Green A, Krisanachinda A, Lassmann M, Ljungberg M, Pozzo L, Quadir KA, Terán Gretter MA, Van Staden J, Poli GL. Multi-centre evaluation of accuracy and reproducibility of planar and SPECT image quantification: An IAEA phantom study. Z Med Phys. 2017;27(2):98-112.
23. Divoli A, Chiavassa S, Ferrer L, Barbet J, Flux GD, Bardiès M. Effect of patient morphology on dosimetric calculations for internal irradiation as assessed by comparisons of Monte Carlo versus conventional methodologies. J Nucl Med. 2009;50(2):316-23.
24. Kull T, Kletting P, Reske SN, Glatting G. Determination of individual organ masses for (90)Y-anti-CD66 radioimmunotherapy: influence on therapy planning. Z Med Phys. 2011;21(4):305-9.
25. Gosewisch A, Delker A, Tattenberg S, Ilhan H, Todica A, Brosch J, Vomacka L, Brunegraf A, Gildehaus FJ, Ziegler S, Bartenstein P, Böning G. Patient-specific image-based bone marrow dosimetry in ^{177}Lu-[DOTA(0),Tyr(3)]-Octreotate and ^{177}Lu-DKFZ-PSMA-617 therapy: investigation of a new hybrid image approach. EJNMMI Res. 2018;8(1):76.
26. Hindorf C, Glatting G, Chiesa C, Linden O, Flux G, Committee ED. EANM Dosimetry Committee guidelines for bone marrow and whole-body dosimetry. Eur J Nucl Med Mol Imaging. 2010;37(6):1238-50.
27. Zaid A, Kletting P, Eiber M, Beer AJ, Glatting G. Technical Note: Optimal sampling schedules for kidney dosimetry based on the hybrid planar/SPECT method in ^{177}Lu-PSMA therapy. Med Phys. 2019;46(12):5861-6.
28. Glatting G, Landmann M, Kull T, Wunderlich A, Blumstein NM, Buck AK, Reske SN. Internal radionuclide therapy: the ULMDOS software for treatment planning. Med Phys. 2005;32(7):2399-405.

29. Rinscheid A, Kletting P, Eiber M, Beer AJ, Glatting G. Influence of sampling schedules on ^{177}Lu-PSMA dosimetry. EJNMMI Phys. 2020;7(1):41.
30. Rinscheid A, Lee J, Kletting P, Beer AJ, Glatting G. A simulation-based method to determine optimal sampling schedules for dosimetry in radioligand therapy. Z Med Phys. 2019;29(4):314-25.
31. Siegel JA, Thomas SR, Stubbs JB, Stabin MG, Hays MT, Koral KF, Robertson JS, Howell RW, Wessels BW, Fisher DR, Weber DA, Brill AB. MIRD pamphlet no. 16: Techniques for quantitative radiopharmaceutical biodistribution data acquisition and analysis for use in human radiation dose estimates. J Nucl Med. 1999;40(2):37s-61s.
32. Kletting P, Schimmel S, Kestler HA, Hänscheid H, Luster M, Fernández M, Bröer JH, Nosske D, Lassmann M, Glatting G. Molecular radiotherapy: the NUKFIT software for calculating the time-integrated activity coefficient. Med Phys. 2013;40(10):102504.
33. Kletting P, Schimmel S, Hänscheid H, Luster M, Fernández M, Nosske D, Lassmann M, Glatting G. The NUKDOS software for treatment planning in molecular radiotherapy. Z Med Phys. 2015;25(3):264-74.
34. Andersson M, Johansson L, Eckerman K, Mattsson S. IDAC-Dose 2.1, an internal dosimetry program for diagnostic nuclear medicine based on the ICRP adult reference voxel phantoms. EJNMMI Res. 2017;7(1):88.
35. Bolch WE, Jokisch D, Zankl M, Eckerman KF, Fell T, Manger R, Endo A, Hunt J, Kim KP, Petoussi-Henss N. ICRP Publication 133: The ICRP computational framework for internal dose assessment for reference adults: specific absorbed fractions. Ann ICRP. 2016;45(2):5-73.
36. Chauvin M, Borys D, Botta F, Bzowski P, Dabin J, Denis-Bacelar AM, Desbrée A, Falzone N, Lee BQ, Mairani A, Malaroda A, Mathieu G, McKay E, Mora-Ramirez E, Robinson AP, Sarrut D, Struelens L, Gil AV, Bardiès M. OpenDose: Open-Access Resource for Nuclear Medicine Dosimetry. J Nucl Med. 2020;61(10):1514-9.
37. Stabin MG, Siegel JA. RADAR Dose Estimate Report: A Compendium of Radiopharmaceutical Dose Estimates Based on OLINDA/EXM Version 2.0. J Nucl Med. 2018;59(1):154-60.
38. Stabin MG, Sparks RB, Crowe E. OLINDA/EXM: the second-generation personal computer software for internal dose assessment in nuclear medicine. J Nucl Med. 2005;46(6):1023-7.
39. Baechler S, Hobbs RF, Prideaux AR, Wahl RL, Sgouros G. Extension of the biological effective dose to the MIRD schema and possible implications in radionuclide therapy dosimetry. Med Phys. 2008;35(3):1123-34.
40. Dale R, Carabe-Fernandez A. The radiobiology of conventional radiotherapy and its application to radionuclide therapy. Cancer Biother Radiopharm. 2005;20(1):47-51.
41. Wessels BW, Konijnenberg MW, Dale RG, Breitz HB, Cremonesi M, Meredith RF, Green AJ, Bouchet LG, Brill AB, Bolch WE, Sgouros G, Thomas SR. MIRD pamphlet No. 20: the effect of model assumptions on kidney dosimetry and response--implications for radionuclide therapy. J Nucl Med. 2008;49(11):1884-99.
42. Hobbs RF, Sgouros G. Calculation of the biological effective dose for piecewise defined dose-rate fits. Med Phys. 2009;36(3):904-7.
43. Fowler J CR, Ritter M. Is alpha/beta for prostate tumors really low? Int J Radiat Oncol Biol Phys. 2001;50:1021–31.
44. Eberlein U, Cremonesi M, Lassmann M. Individualized Dosimetry for Theranostics: Necessary, Nice to Have, or Counterproductive? J Nucl Med. 2017;58(Suppl 2):97s-103s.
45. Virgolini I, Decristoforo C, Haug A, Fanti S, Uprimny C. Current status of theranostics in prostate cancer. Eur J Nucl Med Mol Imaging. 2018;45(3):471-95.
46. Cova T, Bento DJ, Nunes SCC. Computational Approaches in Theranostics: Mining and Predicting Cancer Data. Pharmaceutics. 2019;11(3).

47. Nestorov I. Whole-body physiologically based pharmacokinetic models. Expert Opin Drug Metab Toxicol. 2007;3(2):235-49.
48. Kletting P, Kull T, Maass C, Malik N, Luster M, Beer AJ, Glatting G. Optimized Peptide Amount and Activity for ^{90}Y-Labeled DOTATATE Therapy. J Nucl Med. 2016;57(4):503-8.
49. Kletting P, Muller B, Erentok B, Schmaljohann J, Behrendt FF, Reske SN, Mottaghy FM, Glatting G. Differences in predicted and actually absorbed doses in peptide receptor radionuclide therapy. Med Phys. 2012;39(9):5708-17.
50. Kletting P, Thieme A, Eberhardt N, Rinscheid A, D'Alessandria C, Allmann J, Wester HJ, Tauber R, Beer AJ, Glatting G, Eiber M. Modeling and Predicting Tumor Response in Radioligand Therapy. J Nucl Med. 2019;60(1):65-70.
51. Barrett PH, Bell BM, Cobelli C, Golde H, Schumitzky A, Vicini P, Foster DM. SAAM II: Simulation, Analysis, and Modeling Software for tracer and pharmacokinetic studies. Metabolism. 1998;47(4):484-92.
52. Inc TMW. *MATLAB* (Version 2018a). [Computer software]. 2018 [Available from: https://www.mathworks.com.
53. Winter G, Vogt A, Jiménez-Franco LD, Rinscheid A, Yousefzadeh-Nowshahr E, Solbach C, Beer AJ, Glatting G, Kletting P. Modelling the internalisation process of prostate cancer cells for PSMA-specific ligands. Nucl Med Biol. 2019;72-73:20-5.
54. Hardiansyah D, Begum NJ, Kletting P, Mottaghy FM, Glatting G. Sensitivity Analysis of a Physiologically Based Pharmacokinetic Model Used for Treatment Planning in Peptide Receptor Radionuclide Therapy. Cancer Biother Radiopharm. 2016;31(6):217-24.
55. Hardiansyah D, Kletting P, Begum NJ, Eiber M, Beer AJ, Pawiro SA, Glatting G. Important pharmacokinetic parameters for individualization of ^{177}Lu-PSMA therapy: A global sensitivity analysis for a physiologically-based pharmacokinetic model. Med Phys. 2021;48(2):556-68.
56. Jiménez-Franco LD, Glatting G, Prasad V, Weber WA, Beer AJ, Kletting P. Effect of Tumor Perfusion and Receptor Density on Tumor Control Probability in ^{177}Lu-DOTATATE Therapy: An In Silico Analysis for Standard and Optimized Treatment. J Nucl Med. 2021;62(1):92-8.
57. Jiménez-Franco LD, Kletting P, Beer AJ, Glatting G. Treatment planning algorithm for peptide receptor radionuclide therapy considering multiple tumor lesions and organs at risk. Med Phys. 2018.
58. Zaid NRR, Kletting P, Winter G, Prasad V, Beer AJ, Glatting G. A Physiologically Based Pharmacokinetic Model for In Vivo Alpha Particle Generators Targeting Neuroendocrine Tumors in Mice. Pharmaceutics. 2021;13(12).
59. Begum NJ, Thieme A, Eberhardt N, Tauber R, D'Alessandria C, Beer AJ, Glatting G, Eiber M, Kletting P. The Effect of Total Tumor Volume on the Biologically Effective Dose to Tumor and Kidneys for ^{177}Lu-Labeled PSMA Peptides. J Nucl Med. 2018;59(6):929-33.
60. Begum NJ, Glatting G, Wester HJ, Eiber M, Beer AJ, Kletting P. The effect of ligand amount, affinity and internalization on PSMA-targeted imaging and therapy: A simulation study using a PBPK model. Sci Rep. 2019;9(1):20041.
61. Begum NJ, Glatting G, Eiber M, Beer AJ, Kletting P. An in silico study on the effect of the radionuclide half-life on PET/CT imaging with PSMA-targeting radioligands. Nuklearmedizin. 2020;60(1):33-7.
62. Okamoto S, Thieme A, Allmann J, D'Alessandria C, Maurer T, Retz M, Tauber R, Heck MM, Wester HJ, Tamaki N, Fendler WP, Herrmann K, Pfob CH, Scheidhauer K, Schwaiger M, Ziegler S, Eiber M. Radiation Dosimetry for ^{177}Lu-PSMA I&T in Metastatic Castration-Resistant Prostate Cancer: Absorbed Dose in Normal Organs and Tumor Lesions. J Nucl Med. 2017;58(3):445-50.

63. Rahbar K, Ahmadzadehfar H, Kratochwil C, Haberkorn U, Schafers M, Essler M, Baum RP, Kulkarni HR, Schmidt M, Drzezga A, Bartenstein P, Pfestroff A, Luster M, Lutzen U, Marx M, Prasad V, Brenner W, Heinzel A, Mottaghy FM, Ruf J, Meyer PT, Heuschkel M, Eveslage M, Bogemann M, Fendler WP, Krause BJ. German Multicenter Study Investigating ^{177}Lu-PSMA-617 Radioligand Therapy in Advanced Prostate Cancer Patients. J Nucl Med. 2017;58(1):85-90.
64. Baum RP, Kulkarni HR, Schuchardt C, Singh A, Wirtz M, Wiessalla S, Schottelius M, Mueller D, Klette I, Wester HJ. ^{177}Lu-Labeled Prostate-Specific Membrane Antigen Radioligand Therapy of Metastatic Castration-Resistant Prostate Cancer: Safety and Efficacy. J Nucl Med. 2016;57(7):1006-13.
65. Kratochwil C, Giesel FL, Stefanova M, Benesova M, Bronzel M, Afshar-Oromieh A, Mier W, Eder M, Kopka K, Haberkorn U. PSMA-Targeted Radionuclide Therapy of Metastatic Castration-Resistant Prostate Cancer with ^{177}Lu-Labeled PSMA-617. J Nucl Med. 2016;57(8):1170-6.
66. Gaertner FC HK, Ahmadzadehfar H. Uptake of PSMA-ligands in normal tissues is dependent on tumor load in patients with prostate cancer. Oncotarget. 2017;8:55094–103.
67. Barrett JA, Coleman RE, Goldsmith SJ, Vallabhajosula S, Petry NA, Cho S, Armor T, Stubbs JB, Maresca KP, Stabin MG, Joyal JL, Eckelman WC, Babich JW. First-in-man evaluation of 2 high-affinity PSMA-avid small molecules for imaging prostate cancer. J Nucl Med. 2013;54(3):380-7.
68. Pan AC, Borhani DW, Dror RO, Shaw DE. Molecular determinants of drug-receptor binding kinetics. Drug Discov Today. 2013;18(13-14):667-73.
69. Vogt A. Quantification of the internalization of PSMA-specific peptides in tumor cells [Master thesis]: Hochschule Furtwangen; 2017.
70. Heinzel A, Boghos D, Mottaghy FM, Gaertner F, Essler M, von Mallek D, Ahmadzadehfar H. ^{68}Ga-PSMA PET/CT for monitoring response to ^{177}Lu-PSMA-617 radioligand therapy in patients with metastatic castration-resistant prostate cancer. Eur J Nucl Med Mol Imaging. 2019;46(5):1054-62.
71. Perera M, Papa N, Christidis D, Wetherell D, Hofman MS, Murphy DG, Bolton D, Lawrentschuk N. Sensitivity, Specificity, and Predictors of Positive ^{68}Ga-Prostate-specific Membrane Antigen Positron Emission Tomography in Advanced Prostate Cancer: A Systematic Review and Meta-analysis. Eur Urol. 2016;70(6):926-37.
72. Afshar-Oromieh A, Hetzheim H, Kübler W, Kratochwil C, Giesel FL, Hope TA, Eder M, Eisenhut M, Kopka K, Haberkorn U. Radiation dosimetry of ^{68}Ga-PSMA-11 (HBED-CC) and preliminary evaluation of optimal imaging timing. Eur J Nucl Med Mol Imaging. 2016;43(9):1611-20.
73. Afshar-Oromieh A, Sattler LP, Mier W, Hadaschik BA, Debus J, Holland-Letz T, Kopka K, Haberkorn U. The Clinical Impact of Additional Late PET/CT Imaging with ^{68}Ga-PSMA-11 (HBED-CC) in the Diagnosis of Prostate Cancer. J Nucl Med. 2017;58(5):750-5.
74. Cantiello F, Crocerossa F, Russo GI, Gangemi V, Ferro M, Vartolomei MD, Lucarelli G, Mirabelli M, Scafuro C, Ucciero G, De Cobelli O, Morgia G, Damiano R, Cascini GL. Comparison Between ^{64}Cu-PSMA-617 PET/CT and ^{18}F-Choline PET/CT Imaging in Early Diagnosis of Prostate Cancer Biochemical Recurrence. Clin Genitourin Cancer. 2018;16(5):385-91.
75. Rahbar K, Afshar-Oromieh A, Bögemann M, Wagner S, Schäfers M, Stegger L, Weckesser M. ^{18}F-PSMA-1007 PET/CT at 60 and 120 minutes in patients with prostate cancer: biodistribution, tumour detection and activity kinetics. Eur J Nucl Med Mol Imaging. 2018;45(8):1329-34.
76. Garske U, Sandstrom M, Johansson S, Granberg D, Lundqvist H, Lubberink M, Sundin A, Eriksson B. Lessons on Tumour Response: Imaging during Therapy with ^{177}Lu-

DOTA-octreotate. A Case Report on a Patient with a Large Volume of Poorly Differentiated Neuroendocrine Carcinoma. Theranostics. 2012;2(5):459-71.
77. Kletting P, Bunjes D, Reske SN, Glatting G. Improving anti-CD45 antibody radioimmunotherapy using a physiologically based pharmacokinetic model. J Nucl Med. 2009;50(2):296-302.
78. Kletting P, Kull T, Bunjes D, Luster M, Reske SN, Glatting G. Optimal preloading in radioimmunotherapy with anti-cD45 antibody. Med Phys. 2011;38(5):2572-8.
79. Pandit-Taskar N, O'Donoghue JA, Divgi CR, Wills EA, Schwartz L, Gönen M, Smith-Jones P, Bander NH, Scher HI, Larson SM, Morris MJ. Indium ^{111}labeled J591 anti-PSMA antibody for vascular targeted imaging in progressive solid tumors. EJNMMI Res. 2015;5:28.
80. Dearnaley D, Syndikus I, Mossop H, Khoo V, Birtle A, Bloomfield D, Graham J, Kirkbride P, Logue J, Malik Z, Money-Kyrle J, O'Sullivan JM, Panades M, Parker C, Patterson H, Scrase C, Staffurth J, Stockdale A, Tremlett J, Bidmead M, Mayles H, Naismith O, South C, Gao A, Cruickshank C, Hassan S, Pugh J, Griffin C, Hall E. Conventional versus hypofractionated high-dose intensity-modulated radiotherapy for prostate cancer: 5-year outcomes of the randomised, non-inferiority, phase 3 CHHiP trial. The Lancet Oncology. 2016;17(8):1047-60.
81. Fung EK, Cheal SM, Fareedy SB, Punzalan B, Beylergil V, Amir J, Chalasani S, Weber WA, Spratt DE, Veach DR, Bander NH, Larson SM, Zanzonico PB, Osborne JR. Targeting of radiolabeled J591 antibody to PSMA-expressing tumors: optimization of imaging and therapy based on non-linear compartmental modeling. EJNMMI Res. 2016;6(1):7.
82. Thurber GM, Weissleder R. A systems approach for tumor pharmacokinetics. PLoS One. 2011;6(9):e24696.
83. Rauscher I, Krönke M, König M, Gafita A, Maurer T, Horn T, Schiller K, Weber W, Eiber M. Matched-Pair Comparison of ^{68}Ga-PSMA-11 PET/CT and ^{18}F-PSMA-1007 PET/CT: Frequency of Pitfalls and Detection Efficacy in Biochemical Recurrence After Radical Prostatectomy. J Nucl Med. 2020;61(1):51-7.
84. Carlos Dos Santos J, Beijer B, Bauder-Wüst U, Schäfer M, Leotta K, Eder M, Benešová M, Kleist C, Giesel F, Kratochwil C, Kopka K, Haberkorn U, Mier W. Development of Novel PSMA Ligands for Imaging and Therapy with Copper Isotopes. J Nucl Med. 2020;61(1):70-9.

Appendix

A.1 Supplementary material 1

The supplementary material of the article "**Begum NJ**, Thieme A, Eberhardt N, Tauber R, D'Alessandria C, Beer AJ, Glatting G, Eiber M, Kletting P. The Effect of Total Tumor Volume on the Biologically Effective Dose to Tumor and Kidneys for ^{177}Lu-Labeled PSMA Peptides. J Nucl Med. 2018;59(6):929-933. DOI: 10.2967/jnumed.117.203505" [59] is copyright © 2018 by the Society of Nuclear Medicine and Molecular Imaging. Supplementary material is reprinted with permission for non-commercial purposes.

Supplemental material for:

The effect of total tumor volume on the biologically effective dose of tumor and kidneys for ^{177}Lu-labelled PSMA peptides

Nusrat J Begum[1]*, Anne Thieme[2*], Nina Eberhardt[2], Robert Tauber[3], Ambros J Beer[1], Gerhard Glatting[1], Matthias Eiber[2*], Peter Kletting[1*†]

[1]Medical Radiation Physics, Department of Nuclear Medicine, Universität Ulm, Ulm, Germany
[2]Department of Nuclear Medicine, Klinikum Rechts der Isar, Technische Universität München, Munich, Germany
[3]Department of Urology, Klinikum Rechts der Isar, Technische Universität München, Munich, Germany
*contributed equally
†**Corresponding author:**
Dr. Peter Kletting
Medical Radiation Physics, Department of Nuclear Medicine, Universität Ulm, Albert-Einstein-Alle 23, 89081 Ulm, Germany
E-mail: peter.kletting@uniklinik-ulm.de

Part A: Equations, Parameters, and Compartments

PBPK model equations

The following equations describe the transport of labeled (indexed with *) and unlabeled peptide via blood flow, extravasation, binding, internalization, degradation and release, excretion, and radioactive decay. For therapy, the peptide was intravenously injected as a 20-min infusion. The PET tracer was injected as a bolus. The variables are defined in Supplemental Table A1.

Bound and internalized peptide

Parotid, submandibular, and lacrimal glands, tumor, kidneys, liver, spleen, GI tract, and prostate

Constraint for total PSMA receptors $R_{0,i}$

$$R_{0,i} = R_i + RP_i + RP_i^* \qquad \text{(Eq. A1)}$$

Internalized peptide

$$\begin{aligned} \frac{d}{dt} P_{\text{intern i}} &= \lambda_{\text{int},i} \cdot RP_i - \lambda_{release,i} \cdot P_{\text{intern } i} + \lambda_{phy} \cdot P^*_{\text{intern } i} \\ \frac{d}{dt} P^*_{\text{intern } i} &= \lambda_{\text{int},i} \cdot RP^*_i - \lambda_{release,i} \cdot P^*_{\text{intern } i} - \lambda_{phy} \cdot P^*_{\text{intern } i} \end{aligned} \qquad \text{(Eq. A2)}$$

Bound peptide on cell surface

$$\begin{aligned} \frac{d}{dt} RP_i &= k_{on} \cdot P_{i,\text{int}} \cdot \frac{R_i}{V_{i,\text{int}}} - (k_{off} + \lambda_{\text{int},i}) \cdot RP_i + \lambda_{phy} \cdot RP_i^* \\ \frac{d}{dt} RP_i^* &= k_{on} \cdot P_{i,\text{int}}^* \cdot \frac{R_i}{V_{i,\text{int}}} - (k_{off} + \lambda_{\text{int},i}) \cdot RP_i^* - \lambda_{phy} \cdot RP_i^* \end{aligned} \qquad \text{(Eq. A3)}$$

Free peptide, vascular

Transcapillary extravasation is described by the permeability surface product (PS_i) and the vascular ($V_{i,v}$) and interstitial volumes ($V_{i,int}$) of the pertaining tissue. Convection from the vascular to the interstitial space is neglected as the used peptide represents a rather small molecule (1).

All tissues except kidneys and lungs

$$\frac{d}{dt}P_{i,v} = PS_i\left(\frac{P_{i,\text{int}}}{V_{i,\text{int}}} - \frac{P_{i,v}}{V_{i,v}}\right) + F_i\left(\frac{P_{ART}}{V_{ART}} - \frac{P_{i,v}}{V_{i,v}}\right) + \lambda_{phy}\cdot P^*_{i,v}$$
$$\frac{d}{dt}P_{i,v}{}^* = PS_i\left(\frac{P^*_{i,\text{int}}}{V_{i,\text{int}}} - \frac{P^*_{i,v}}{V_{i,v}}\right) + F_i\left(\frac{P^*_{ART}}{V_{ART}} - \frac{P^*_{i,v}}{V_{i,v}}\right) - \lambda_{phy}\cdot P^*_{i,v} \quad \text{(Eq. A4)}$$

For brain PS = 0

Lungs

$$\frac{d}{dt}P_{LU,v} = PS_{LU}\left(\frac{P_{LU,\text{int}}}{V_{LU,\text{int}}} - \frac{P_{LU,v}}{V_{LU,v}}\right) + F\left(\frac{P_{VEN}}{V_{VEN}} - \frac{P_{LU,v}}{V_{LU,v}}\right) + \lambda_{phy}\cdot P^*_{LU,v}$$
$$\frac{d}{dt}P_{LU,v}{}^* = PS_{LU}\left(\frac{P_{LU,\text{int}}{}^*}{V_{LU,\text{int}}} - \frac{P_{LU,v}{}^*}{V_{LU,v}}\right) + F\left(\frac{P_{VEN}}{V_{VEN}} - \frac{P_{LU,v}{}^*}{V_{LU,v}}\right) - \lambda_{phy}\cdot P^*_{LU,v} \quad \text{(Eq. A5)}$$

Kidneys

$$\frac{d}{dt}P_{K,v} = -\frac{P_{K,v}}{V_{K,v}}\cdot(F_{fil}+F_K) + \frac{F_K}{V_{ART}}\cdot P_{ART} + \frac{P_{\text{intra,K}}}{V_{\text{intra,K}}}\cdot(F_{fil}-F_{ex}) + \lambda_{phy}\cdot P^*_{K,v}$$
$$\frac{d}{dt}P^*_{K,v} = -\frac{P^*_{K,v}}{V_{K,v}}\cdot(F_{fil}+F_K) + \frac{F_K}{V_{ART}}\cdot P^*_{ART} + \frac{P^*_{\text{intra,K}}}{V_{\text{intra,K}}}\cdot(F_{fil}-F_{ex}) - \lambda_{phy}\cdot P^*_{K,v} \quad \text{(Eq. A6)}$$

Veins

$$\frac{d}{dt}P_{VEN} = -k_{Pr}\cdot P_{VEN} + \sum\frac{F_i}{V_i}P_{i,v} - \frac{F_M}{V_M}P_{M,v} - \frac{F_{GI}}{V_{GI}}P_{GI,v} + \frac{F_M + F_{GI}}{V_L}P_{L,v} + \lambda_{phy}\cdot P^*_{VEN}$$
$$\frac{d}{dt}P^*_{VEN} = -k_{Pr}\cdot P^*_{VEN} + \sum\frac{F_i}{V_i}P^*_{i,v} - \frac{F_M}{V_M}P^*_{M,v} - \frac{F_{GI}}{V_{GI}}P^*_{GI,v} + \frac{F_M + F_{GI}}{V_L}P^*_{L,v} - \lambda_{phy}\cdot P^*_{VEN} \quad \text{(Eq. A7)}$$

Arteries

$$\frac{d}{dt}P_{ART} = -\sum\frac{F_i}{V_{ART}}\cdot P_{i,v} + \frac{F}{V_{LU,v}}\cdot P_{LU,v} + \lambda_{phy}\cdot P^*_{ART}$$
$$\frac{d}{dt}P^*_{ART} = -\sum\frac{F_i}{V_{ART}}\cdot P_{i,v} + \frac{F}{V_{LU,v}}\cdot P_{LU,v} - \lambda_{phy}\cdot P^*_{ART} \quad \text{(Eq. A8)}$$

Free peptide, interstitial spaces

Kidneys

$$\frac{d}{dt}P_{K,int} = -k_{on}\cdot P_{K,int}\cdot\frac{R_K}{V_{K,int}} + k_{off}\cdot RP_K + F_{fil}\left(\frac{P_{K,v}}{V_{K,v}} - \frac{P_{K,int}}{V_{K,int}}\right) + \lambda_{phy}\cdot P^*_{K,int}$$
$$\frac{d}{dt}P^*_{K,int} = -k_{on}\cdot P^*_{K,int}\cdot\frac{R_K}{V_{K,int}} + k_{off}\cdot RP^*_K + F_{fil}\left(\frac{P^*_{K,v}}{V_{K,v}} - \frac{P^*_{K,int}}{V_{K,int}}\right) - \lambda_{phy}\cdot P^*_{K,int} \quad \text{(Eq. A9)}$$

Muscle, red marrow, skin, lungs, adipose tissue, heart, bone, REST, and brain (PS = 0)

$$\frac{d}{dt}P_{i,int} = PS_i\left(\frac{P_{i,v}}{V_{i,v}} - \frac{P_{i,int}}{V_{i,int}}\right) + \lambda_{phy}\cdot P^*_{i,int}$$
$$\frac{d}{dt}P^*_{i,int} = PS_i\left(\frac{P^*_{i,v}}{V_{i,v}} - \frac{P^*_{i,int}}{V_{i,int}}\right) - \lambda_{phy}\cdot P^*_{i,int} \quad \text{(Eq. A10)}$$

Parotid, submandibular and lacrimal glands, tumor, kidneys, liver, spleen, GI tract, and prostate

$$\frac{d}{dt}P_{i,\text{int}} = -k_{on}\cdot P_{i,\text{int}}\cdot\frac{R_i}{V_{i,\text{int}}} + k_{off}\cdot RP_i + PS_i\left(\frac{P_{i,v}}{V_{i,v}} - \frac{P_{i,\text{int}}}{V_{i,\text{int}}}\right) + \lambda_{phy}\cdot P^*_{i,\text{int}}$$
$$\frac{d}{dt}P^*_{i,\text{int}} = -k_{on}\cdot P^*_{i,\text{int}}\cdot\frac{R_i}{V_{i,\text{int}}} + k_{off}\cdot RP_i{}^* + PS_i\left(\frac{P^*_{i,v}}{V_{i,v}} - \frac{P^*_{i,\text{int}}}{V_{i,\text{int}}}\right) - \lambda_{phy}\cdot P^*_{i,\text{int}} \quad \text{(Eq. A11)}$$

Further equations

Peptide in kidney cells (unspecific)

$$\frac{d}{dt}P_{\text{intra,K}} = \frac{P_{\text{int,K}}}{V_{\text{int},K}}\cdot(F_{fil} - F_{ex}) - \frac{P_{\text{intra,K}}}{V_{\text{intra,K}}}\cdot(F_{fil} - F_{ex}) + \lambda_{phy}\cdot P^*_{\text{intra,K}}$$
$$\frac{d}{dt}P^*_{\text{intra,K}} = \frac{P^*_{\text{int,K}}}{V_{\text{int},K}}\cdot(F_{fil} - F_{ex}) - \frac{P^*_{\text{intra,K}}}{V_{\text{intra,K}}}\cdot(F_{fil} - F_{ex}) - \lambda_{phy}\cdot P^*_{\text{intra,K}} \quad \text{(Eq. A12)}$$

Bound to protein

$$\frac{d}{dt}PRP = k_{PR}\cdot P_{VEN} + \lambda_{phy}\cdot PRP^*$$
$$\frac{d}{dt}PRP^* = k_{PR}\cdot P^*_{VEN} - \lambda_{phy}\cdot PRP^* \quad \text{(Eq. A13)}$$

Supplemental Table A1: Parameter definitions

Variable		Value	Unit	Source
k_{on}	association rate	0.046	$l \cdot nmol^{-1}$ min^{-1}	(2)[a]
K_D	dissociation constant	1	$nmol \cdot l^{-1}$	(2)[a]
k_{off}	dissociation rate	$K \cdot k_{on}$	min^{-1}	
λ_{phy}	physical decay ^{177}Lu and ^{68}Ga	$7.15 \cdot 10^{-5}/1.03 \cdot 10^{-2}$	min^{-1}	
BW	body weight	measured	kg	
BH	body height	measured	cm	
H	hematocrit	measured	unity	
F	flow total serum without tumor	$V_P \cdot 1.23/min$[b]	$l \cdot min^{-1}$	(3)
V_P	volume of total body serum	$2.8 \cdot (1\text{-}H) \cdot BSA \cdot (l \cdot m^{-2})$	l	(4)
BSA	body surface area	$0.007184 \cdot BH^{0.725} \cdot BW^{0.425}$	m^2	(4)
ρ	assumed density for all organs and tumor	1 ml ≙ 1 g		
Tumor				
$V_{TU,total}$	total volume of tumor 1 and 2 time start of therapy	$V_{TU,total,0} \cdot e^{(\lambda g \cdot \Delta T)}$ during therapy $\lambda_g = 0$	l	
$V_{TU,total,0}$	total volume of tumor 1 and 2 time of PET	measured	l	
ΔT	time between PET and therapy	measured	min	
λ_g	growth rate for androgen-independent tumor cells	bone: $5.12 \cdot 10^{-6}$ lymph node: $3.85 \cdot 10^{-6}$	min^{-1}	(5)
$V_{TU,REST,total}$	total volume of REST tumor time of therapy	$x_V \cdot V_{VOI,TU,REST} \cdot e^{(\lambda g \cdot \Delta T)}$ λ_g for bone was used	l	
$V_{TU,REST,total,0}$	total volume of REST tumor time of PET	$x_V \cdot V_{VOI,TU,REST}$	l	
$V_{VOI,TU,REST}$	PET/CT volume with 15%–20% SUV max	measured	l	
x_V	ratio between actual volume and PET/CT volume	fitted	unity	
$V_{TU,int}$	interstitial space of tumor	$v_{TU,int} \cdot V_{TU,total}$	l	
$V_{TU,v}$	vascular space of tumor	$v_{TU,v} \cdot V_{TU,total}$	l	
$V_{TU,REST,int}$	interstitial space of tumor remainder	$v_{TU,int}$ $V_{TU,REST,total}$	l	
$V_{TU,REST,v}$	vascular space of tumor remainder	$v_{TU,v} \cdot V_{TU,REST,total}$	l	
$v_{TU,int}$	interstitial space fraction of total tumor	0.38	unity	(6)

$v_{TU,v}$	vascular (serum) fraction of total tumor	$0.05 \cdot (1-H)$	unity	(7)
F_{TU}	serum flow tumor	$f_{TU} \cdot V_{TU,total}$	$l \cdot min^{-1}$	
$F_{TU,REST}$	serum flow tumor remainder	$f_{TU} \cdot V_{TU,REST,total}$	$ml \cdot min^{-1}$	
f_{TU}	serum flow density tumor	fitted	$ml \cdot min^{-1} \cdot g^{-1}$	(7, 8)
$f_{TU,REST}$	serum flow density REST tumor	$x_f \cdot (f_{tu,1}+f_{tu,2})/2$	$ml \cdot min^{-1} \cdot g^{-1}$	
x_f	ratio of actual and assumed flow density tumor remainder	fitted	unity	
PS_{TU}	permeability surface area product tumor	$k_{TU} \cdot V_{TU,total}$	$ml \cdot min^{-1}$	
$PS_{TU,REST}$	permeability surface area product tumor remainder	$k_{TU} \cdot V_{TU_REST,total}$	$ml \cdot min^{-1}$	
k_{TU}	permeability surface area product tumor per unit mass (scaled for molecule size of PSMA I&T)	0.6 (maximal value from (6))	$ml \cdot min^{-1} \cdot g^{-1}$	(7)
$k_{TU,REST}$	permeability surface area product tumor per unit mass (scaled for molecule size of PSMA I&T)	$k_{TU,REST} = k_{TU}$	$ml \cdot min^{-1} \cdot g^{-1}$	
$[R_{TU,0}]$	PSMA receptor density	fitted	$nmol \cdot l^{-1}$	
$[R_{TU,REST,0}]$	PSMA receptor density tumor remainder	$x_r \cdot ([R_{TU,1,0}]+ [R_{TU,2,0}])/2$	$nmol \cdot l^{-1}$	(9)
x_r	ratio between actual and assumed receptor density of tumor remainder	fitted	unity	
$R_{TU,0}$	PSMA receptor number	$[R_{TU,0}] \cdot V_{TU,total}$	nmol	
$R_{TU,REST,0}$	PSMA receptor number tumor remainder[c]	$[R_{TU,REST,0}]\ V_{TU_REST,total}$	nmol	
$\lambda_{TU,int}$	internalization rate tumor	0.001	min^{-1}	(10)
$\lambda_{TU,release}$	release rate tumor	fitted	min^{-1}	
$\lambda_{TU,REST,int}$	internalization rate tumor remainder	0.001	min^{-1}	(10)
$\lambda_{TU,REST,release}$	release rate tumor remainder	$(\lambda_{TU,1,release} + \lambda_{TU,2,release})/2$	min^{-1}	

Liver, spleen, and kidneys

$V_{L,total}$	volume total liver	CT measured	l	(11)
$V_{S,total}$	volume total spleen	CT measured	l	
$V_{K,total}$	volume total kidneys	CT measured	l	
$V_{i,v}$	vascular (serum) volume organ liver, spleen, kidneys	$V_{i,total} \cdot v_{i,v}$	l	
$V_{i,int}$	interstitial volume liver, spleen, kidneys	$V_{i,total} \cdot v_{i,int}$	l	
$V_{K,\ intra}$	volume intracellular kidneys	$(V_{K,total} - V_{K,int} - V_{K,v}) \cdot 2/3$[d]	l	
$v_{L,v}$	vascular (serum) fraction liver	0.085	unity	(12)

$v_{S,v}$	vascular (serum) fraction spleen	0.12	unity	(12)
$v_{K,v}$	vascular (serum) fraction kidneys	0.055	unity	(12)
$v_{L,int}$	interstitial fraction liver	0.2	unity	(12)
$v_{S,int}$	interstitial fraction spleen	0.2	unity	(12)
$v_{K,int}$	interstitial fraction kidneys	0.15	unity	(12)
F_L	serum flow liver arterial	$0.065 \cdot F$	$l \cdot min^{-1}$	(3)
F_S	serum flow spleen	$0.03 \cdot F$	$l \cdot min^{-1}$	(3)
F_K	serum flow kidney	$f_K V_{K,total} \cdot (1\text{-}H)$	$l \cdot min^{-1}$	
f_K	age-dependent blood flow to the kidney	$f_{K,C} - 0.026 \cdot Age$	$ml \cdot min^{-1} \cdot g^{-1}$	(13)
$f_{K,C}$	kidney blood flow, age-independent factor for all ages	fitted	$ml \cdot min^{-1} \cdot g^{-1}$	
$\varphi_{Therapy}$	ratio of sieving coefficients therapy	$\Theta_{PSMA\ I\&T}/\Theta_{Cr\text{-}51\text{-}EDTA} = 0.66$	unity	(14)
φ_{PET}	ratio of sieving coefficients PET/CT	$\Theta_{PET}/\Theta_{Cr\text{-}51\text{-}EDTA} = 0.75$		
GFR	glomerular filtration rate with ^{51}Cr-EDTA	$F_K \cdot x_k$	$l \cdot min^{-1}$	(15)
x_k	filtrated fraction of blood flow	fitted	unity	
F_{fil}	filtration	$GFR \cdot \varphi_i$ [c]	$l \cdot min^{-1}$	
F_{ex}	excretion	$F_{fil} \cdot f_{ex}$	$l \cdot min^{-1}$	
f_{ex}	excretion fraction	0.96	unity	(16)
k_L	permeability surface area product per unit mass for liver	$k_{MUS} \cdot 100$	$ml \cdot min^{-1} \cdot g^{-1}$	(17)
k_S	permeability surface area product per unit mass for spleen	k_L (due to similar capillary structure)	$ml \cdot min^{-1} \cdot g^{-1}$	
$[R_{L,0}]$	receptor density liver	$[R_{PRO,0}] \cdot 0.05$	$nmol \cdot l^{-1}$	(18)
$[R_{S,0}]$	receptor density spleen	$[R_{K,0}] \cdot 0.2$	$nmol \cdot l^{-1}$	(18)
$[R_{K,0}]$	receptor density kidneys	fitted	$nmol \cdot l^{-1}$	
$\lambda_{L,\ int}$	internalization rate PSMA liver	$\lambda_{TU,\ int}$	min^{-1}	(19)
$\lambda_{S,\ int}$	internalization rate PSMA spleen	$\lambda_{TU,\ int}$	min^{-1}	(19)
$\lambda_{K,\ int}$	internalization rate PSMA kidneys	$\lambda_{TU,\ int}$	min^{-1}	(19)
$\lambda_{L,release}$	release rate liver	$\lambda_{K,release}$	min^{-1}	(16, 20)
$\lambda_{S,release}$	release rate spleen	$\lambda_{K,release}$	min^{-1}	(16)
$\lambda_{K,release}$	release rate kidneys	fitted	min^{-1}	

Other organs				
$V_{PRO,total}$	volume total prostate	0.016·BW/71	1	(21)
$V_{LU,total}$	volume total lungs	1·BW/71	1	(21)
$V_{PAR,total}$	volume total parotid gland	CT measured	1	
$V_{LAC,total}$	volume total lacrimal glands	CT measured	1	
$V_{SUB,total}$	volume total submandibular glands	CT measured	1	
$V_{MUS,total}$	volume total muscles	30.078·BW/71	1	(21)
$V_{GI,total}$	volume total GI + pancreas	(0.385+0.548+0.104+ 0.15)·BW/71	1	(21)
$V_{SKIN,total}$	volume total skin	3.408·BW/71	1	(21)
$V_{ADI,total}$	volume total adipose tissue	13.465·BW/71	1	
$V_{RM,total}$	volume total red marrow	1.1·BW/71	1	(21)
$V_{BONE,total}$	volume total bone without red marrow	10.165·BW/71 - $V_{RM,total}$	1	(21)
$V_{HRT,total}$	volume total heart	0.341·BW/71	1	(21)
$V_{BR,total}$	volume total brain	1.45·BW/71	1	(21)
V_{BW}	volume of total body based on BW	1 ml ≙ 1 g	1	
$V_{REST,total}$	volume of REST body, i = all organs except tumor	$V_{BW} - \sum_i V_{i,total}$	1	
$V_{PRO,v}$	vascular volume prostate	0.004·(1-H)·$V_{PRO,total}$	1	(6)
$V_{LU,v}$	vascular (serum) volume lungs	0.105·V_P	1	(3)
$V_{PAR,v}$	vascular (serum) volume parotid glands	0.03·(1-H)·$V_{SAL,total}$	1	(22)
$V_{LAC,v}$	vascular (serum) volume lacrimal glands	0.03·(1-H)·$V_{LAC,total}$		
$V_{SUB,v}$	vascular (serum) volume submandibular glands	0.03·(1-H)·$V_{SUB,total}$		
$V_{MUS,v}$	vascular (serum) volume muscles	0.14·V_P	1	(3)
$V_{GI,v}$	vascular (serum) volume GI + pancreas	0.076·V_P	1	(3)
$V_{SKIN,v}$	vascular (serum) volume skin	0.03·V_P	1	(3)
$V_{ADI,v}$	vascular (serum) volume adipose tissue	0.05·V_P	1	(3)
$V_{RM,v}$	vascular (serum) volume red marrow	0.04·V_P	1	(3)
$V_{BONE,v}$	vascular volume bone without red marrow	0.07·V_P - $V_{RM,v}$	1	(3)
$V_{HRT,v}$	vascular (serum) volume heart (supply)	0.01·V_P	1	(3)
$V_{BR,v}$	vascular (serum) volume brain	0.012·V_P	1	(3)

$V_{REST,v}$	serum volume REST, i = all organs except tumor	$V_P - \sum_i V_{i,v}$	l	
V_{ART}	arterial serum plus ½ serum content of heart	$0.06 \cdot V_P + 0.045 \cdot V_P$	l	(3)
V_{VENES}	venous serum plus ½ serum content of heart	$0.18 \cdot V_P + 0.045 \cdot V_P$	l	(3)
$V_{PRO,int}$	interstitial fraction prostate	$0.25 \cdot V_{PRO,total}$	l	(6)
$V_{LU,int}$	interstitial fraction lungs	$V_{LU,v} \cdot \alpha_{LU}$	l	
$V_{PAR,int}$	interstitial fraction parotid glands	$0.23 \cdot V_{SAL,total}$	l	(22)
$V_{LAC,int}$	interstitial fraction lacrimal glands	$0.23 \cdot V_{LAC,total}$	l	
$V_{SUB,int}$	interstitial fraction submandibular glands	$0.23 \cdot V_{SUB,total}$	l	
$V_{MUS,int}$	interstitial fraction muscles	$V_{MUS,v} \cdot \alpha_{MUS}$	l	
$V_{GI,int}$	interstitial fraction GI + pancreas	$V_{GI,v} \cdot \alpha_{GI}$	l	
$V_{SKIN,int}$	interstitial fraction skin	$V_{SKIN,v} \cdot \alpha_{SKIN}$	l	
$V_{ADI,int}$	interstitial fraction adipose tissue	$V_{ADI,v} \cdot \alpha_{ADI}$	l	
$V_{RM,int}$	interstitial fraction red marrow	$V_{RM,v} \cdot \alpha_{RM}$	l	
$V_{BONE,int}$	interstitial fraction bone without red marrow	$V_{BONE,v} \cdot \alpha_{BONE}$	l	
$V_{HRT,int}$	interstitial fraction heart	$V_{HRT,v} \cdot \alpha_{HRT}$	l	
$V_{REST,int}$	volume of REST body	$V_{REST,v} \cdot \alpha_{REST}$	l	
α_{MUS}	ratio of interstitial to vascular volume average man	$V_{MUS,int}/V_{MUS,v} = 5.9$	unity	(12)
α_{GI}	ratio of interstitial to vascular volume average man	$V_{GI,int}/V_{GI,v} = 8.8$	unity	(12)
α_{SKIN}	ratio of interstitial to vascular volume average man	$V_{SKIN,int}/V_{SKIN,v} = 8.9$	unity	(12)
α_{ADI}	ratio of interstitial to vascular volume average man	$V_{ADI,int}/V_{ADI,v} = 15.5$	unity	(12)
α_{RM}	ratio of interstitial to vascular volume average man	$V_{RM,int}/V_{RM,v} = 3.7$	unity	(12)
α_{HRT}	ratio of interstitial to vascular volume average man	$V_{HRT,int}/V_{HRT,v} = 3.7$	unity	(12)
α_{LU}	ratio of interstitial to vascular volume average man	$V_{LU,int}/V_{LU,v} = 5.5$	unity	(12)
α_{BONE}	ratio of interstitial to vascular volume average man	$V_{BONE,int}/V_{BONE,v} = 8.4$	unity	(12)
α_{REST}	ratio of interstitial to vascular volume average man	$V_{REST,int}/V_{REST,v} = 4.1$	unity	(12)
f_{PRO}	serum flow density prostate	$0.18 \cdot (1\text{-}H)$	$ml \cdot min^{-1} \cdot g^{-1}$	(6)
F_{PRO}	total serum flow to prostate	$f_{PRO} \cdot V_{PRO,total}$	$ml \cdot min^{-1}$	
f_{PAR}	serum flow density parotid glands	0.16	$ml \cdot min^{-1} \cdot g^{-1}$	(23)
F_{SAL}	total serum flow to parotid glands	$f_{SAL} \cdot V_{SAL,total}$	$ml \cdot min^{-1}$	
f_{LAC}	serum flow density lacrimal glands	f_{SAL}	$ml \cdot min^{-1} \cdot g^{-1}$	
F_{LAC}	total serum flow to lacrimal glands	$f_{LAC} \cdot V_{LAC,total}$	$ml \cdot min^{-1}$	

f_{SUB}	serum flow density submandibular glands	f_{SAL}	$ml \cdot min^{-1} \cdot g^{-1}$	
F_{SUB}	total serum flow to submandibular glands	$f_{SUB} \cdot V_{SUB,total}$	$ml \cdot min^{-1}$	
F_{LU}	total serum flow lungs	F_{TOTAL}	$ml \cdot min^{-1}$	(3)
F_{MUS}	total serum flow to muscle	$0.17 \cdot F$	$ml \cdot min^{-1}$	(3)
F_{GI}	total serum flow to GI + pancreas	$0.16 \cdot F$	$ml \cdot min^{-1}$	(3)
F_{SKIN}	total serum flow to skin	$0.05 \cdot F$	$ml \cdot min^{-1}$	(3)
F_{ADI}	total serum flow to adipose	$0.05 \cdot F$	$ml \cdot min^{-1}$	(3)
F_{RM}	total serum flow to red marrow (RM)	$0.03 \cdot F$	$ml \cdot min^{-1}$	(3)
F_{BONE}	total serum flow to bone (without RM)	$0.05 \cdot F$	$ml \cdot min^{-1}$	(3)
F_{HRT}	total serum flow to heart	$0.04 \cdot F$	$ml \cdot min^{-1}$	(3)
F_{BR}	total serum flow to brain	$0.12 \cdot F$	$ml \cdot min^{-1}$	(3)
F_{REST}	i = all organs except tumor	$F - \sum_i F_i$	$ml \cdot min^{-1}$	
F_{TOTAL}	total serum flow including tumor tissue	$F + F_{TU,1} + F_{TU,2} + F_{TU,REST}$	$ml \cdot min^{-1}$	
PS_i	permeability surface area product	$k_i \cdot V_{i,\,total}$	$ml \cdot min^{-1}$	
k_{PRO}	permeability surface area product per unit mass (scaled for molecule size of PSMA I&T) for prostate	0.1	$ml \cdot min^{-1} \cdot g^{-1}$	(6)
k_{LU}	permeability surface area product per unit mass for lungs	$k_{MUS} \cdot 100$	$ml \cdot min^{-1} \cdot g^{-1}$	(17)
k_{PAR}	permeability surface area product per unit mass for parotid glands	0.4	$ml \cdot min^{-1} \cdot g^{-1}$	(24)
k_{LAC}	permeability surface area product per unit mass for lacrimal glands	k_{SAL}	$ml \cdot min^{-1} \cdot g^{-1}$	
k_{SUB}	permeability surface area product per unit mass for submandibular glands	k_{SAL}	$ml \cdot min^{-1} \cdot g^{-1}$	
k_{MUS}	permeability surface area product per unit mass for muscle	0.02	$ml \cdot min^{-1} \cdot g^{-1}$	(17)
k_{GI}	permeability surface area product per unit mass for GI and pancreas	0.02 (assumed similar to muscle)	$ml \cdot min^{-1} \cdot g^{-1}$	
k_{SKIN}	permeability surface area product per unit mass for skin	0.02 (assumed similar to muscle)	$ml \cdot min^{-1} \cdot g^{-1}$	
k_{ADI}	permeability surface area product per unit mass for adipose	0.02 (assumed similar to muscle)	$ml \cdot min^{-1} \cdot g^{-1}$	

k_{RM}	permeability surface area product per unit mass for red marrow	k_L (assumed similar to liver)	$ml \cdot min^{-1} \cdot g^{-1}$	
k_{HRT}	permeability surface area product per unit mass for heart	0.02 (assumed similar to muscle)	$ml \cdot min^{-1} \cdot g^{-1}$	
k_{BONE}	permeability surface area product per unit mass for bone	0.02 (assumed similar to muscle)	$ml \cdot min^{-1} \cdot g^{-1}$	
k_{REST}	permeability surface area product per unit mass for REST	0.02 (assumed similar to muscle)	$ml \cdot min^{-1} \cdot g^{-1}$	
$[R_{PRO,0}]$	receptor density prostate	$[R_{TU,REST,0}]$ 110	$nmol\ l^{-1}$	(23, 25)
$[R_{PAR,0}]$	receptor density parotid glands	42	$nmol\ l^{-1}$	(23)
$[R_{LAC,0}]$	receptor density lacrimal glands	$[R_{SAL,0}]$	$nmol\ l^{-1}$	
$[R_{SUB,0}]$	receptor density submandibular glands	$[R_{SAL,0}]$	$nmol\ l^{-1}$	
$[R_{GI,0}]$	receptor density GI + pancreas	$[R_{PRO,0}] \cdot 0.06$	$nmol\ l^{-1}$	(18)
$\lambda_{NT,int}$	internalization rate for normal tissue	$\lambda_{TU,int}$	min^{-1}	(19)
$\lambda_{PAR,int}$	internalization rate for parotid glands	$\lambda_{TU,int}$	min^{-1}	
$\lambda_{LAC,int}$	internalization rate for lacrimal glands	$\lambda_{TU,int}$	min^{-1}	
$\lambda_{SUB,int}$	internalization rate for submandibular glands	$\lambda_{TU,int}$	min^{-1}	
$\lambda_{NT,release}$	degradation and release normal tissue (except salivary glands)	$\lambda_{K,release}$	min^{-1}	
$\lambda_{PARL,release}$	degradation and release parotid glands	0.00037	min^{-1}	(23)
$\lambda_{LAC,release}$	degradation and release lacrimal glands	$\lambda_{SAL,release}$	min^{-1}	
$\lambda_{SUB,release}$	degradation and release submandibular glands	$\lambda_{SAL,release}$	min^{-1}	
R	receptors free		nmol	
$R_{i,0}$	receptors total number of PSMA positive organ i	$[R_{i,0}] \cdot V_{i,total}$	nmol	
$[R_{i,0}]$	receptor density of PSMA positive organ i		$nmol\ l^{-1}$	
RP_i	peptide bound		nmol	
PRP	peptide bound to serum protein		nmol	
k_{PR}	binding rate peptide to serum	$4.7 \cdot 10^{-4}$	min^{-1}	(10)
$P_{i,intern}$	peptide internalized		nmol	
$P_{i,v}$	peptide free vascular		nmol	
$P_{i,int}$	peptide free interstitial		nmol	
$P_{K,intra}$	peptide interacellular kidneys		nmol	

P_{inj}	injected amount of unlabeled peptide	P1-5: 139;91;81; 67;294	nmol	
P^*_{inj}	injected amount of labeled peptide	P1-5: 8.4;7.5;7.5;7.5;7.8	nmol	

[a]Mean values from all measured (Biacore) ligands. The measured dissociation constant values are considerably lower than reported in the literature but very similar for the therapeutic (26) and PET ligand (27).

[b]For the average normal adult (blood) F = 6500 ml/min and V = 5300 ml. Therefore, a factor of 1.23 was assigned to account for the changes in total serum flow due to volume changes.

[c]Using the assumption of 266 $nmol \cdot l^{-1}$ receptor density (9), 10^{12} cells per liter and 10 ml or 50 ml addition tumor volume.

[d]It is assumed that 2/3 of the total intracellular volume of the kidneys is represented by the proximal tubular cells

[e]Scaling of GFR due to different molecular sizes

Absorbed Dose (D) and Biologically Effective Dose (BED)

To calculate the absorbed dose (only self-dose was considered) and the BED of the kidneys, submandibular glands, parotid glands, and tumor, the following equations and parameter values (Supplemental Table A2) were used:

$$\dot{D}_i(t) = A_i(t) \cdot S_{i \leftarrow i} = A_{inj} \cdot a_i(t) \cdot S_{i \leftarrow i} \qquad \text{(Eq. A14)}$$

$$D_i(T) = \int_0^T \dot{D}_i(t)dt = A_{inj} \cdot \tilde{a}_i(T) \cdot S_{i \leftarrow i} \qquad \text{(Eq. A15)}$$

The BED (28) is defined as

$$BED_i = D_i \cdot (1 + \frac{G_i}{\alpha_i / \beta_i} \cdot D_i) \qquad \text{(Eq. A16)}$$

The factor G_i (Lea–Catcheside factor) (28) is defined as

$$G_i(T) = \frac{2}{D_i^2} \cdot \int_0^T \dot{D}_i(t)dt \cdot \int_0^t \dot{D}_i(\omega) \cdot e^{-\mu_i(t-\omega)} d\omega \qquad \text{(Eq. A17)}$$

Thus, after inserting Eq. A17 in Eq. A16 one obtains

$$BED_i = D_i + \frac{2 \cdot \int_0^T \dot{D}_i(t)dt \cdot \int_0^t \dot{D}_i(\omega) \cdot e^{-\mu_i(t-\omega)} d\omega}{\alpha_i / \beta_i} \qquad \text{(Eq. A18)}$$

Supplemental Table A2: Parameter definitions

Variable		Value	Unit	Source
$S_{K\leftarrow K}$	dose factor kidneys to kidneys	$4.82\cdot10^{-6}\cdot0.299/V_{K,total,measured}$	$Gy\cdot min^{-1}\cdot MBq^{-1}$	(11)
$S_{SUB\leftarrow SUB}$	dose factor submandibular glands to submandibular glands	$S = 82.81/(V_{SUB,total}\cdot1000) + 1.21/(V_{SUB,total}\cdot1000)^{2/3} - 0.11/(V_{SUB,total}\cdot1000)^{1/3}$	$Gy\cdot min^{-1}\cdot MBq^{-1}$	
$S_{PAR\leftarrow PAR}$	dose factor parotid glands to parotid glands	$S = 82.81/(V_{SAL,total}\cdot1000) + 1.21/(V_{SAL,total}\cdot1000)^{2/3} - 0.11/(V_{SAL,total}\cdot1000)^{1/3}$	$Gy\cdot min^{-1}\cdot MBq^{-1}$	
$S_{RM\leftarrow RM}$	dose factor red marrow to red marrow	$S = 82.81/(V_{RM,total}\cdot1000) + 1.21/(V_{RM,total}\cdot1000)^{2/3} - 0.11/(V_{SAL,total}\cdot1000)^{1/3}$	$Gy\cdot min^{-1}\cdot MBq^{-1}$	
$S_{TU\leftarrow TU}$	dose factor tumor to tumor [a]	$S = 82.81/(V_{TU,total}\cdot1000) + 1.21/(V_{TU,total}\cdot1000)^{2/3} - 0.11/(V_{TU,total}\cdot1000)^{1/3}$	$Gy\cdot min^{-1}\cdot MBq^{-1}$	(29)
α/β_K	radiobiological parameters kidneys	2.5	Gy	(30)
μ_K	repair rate kidneys	ln(2)/60/2.8	min^{-1}	(30)
α/β_{SUB}	radiobiological parameters submandibular glands	0.053/0.0118	Gy	
μ_{SUB}	repair rate submandibular glands	0.0077	min^{-1}	
α/β_{PAR}	radiobiological parameters parotid glands	0.053/0.0118	Gy	
μ_{PAR}	repair rate parotid glands	0.0077	min^{-1}	
α/β_{RM}	radiobiological parameters red marrow	15	Gy	
μ_{RM}	repair rate red marrow	ln(2)/60/1.5	min^{-1}	
α/β_{TU}	radiobiological parameters tumor	1.49	Gy	(31)
μ_{TU}	repair rate tumor	ln(2)/60/1.9	min^{-1}	
$\tilde{a}_i$	time-integrated activity coefficient of organ i		h	
a_i	fraction of administered activity of organ i		unity	
D_i	dose to organ i		Gy	
$\dot{D}_i$	dose rate to organ i		$Gy\cdot min^{-1}$	
T	integration time	30000	min	

G_i	Lea–Catcheside factor of organ i		unity	(32)
BED_i	biologically effective dose to organ i		Gy	(32)

[a]The function $S = A/(V_{TU,total}\cdot 1000) + B/(V_{TU,total}\cdot 1000)^{2/3} - C/(V_{TU,total}\cdot 1000)^{1/3}$ (valid for tumors > 1 ml) was fitted to the OLINDA data for Lu^{177} spheres.

PBPK Model Compartments

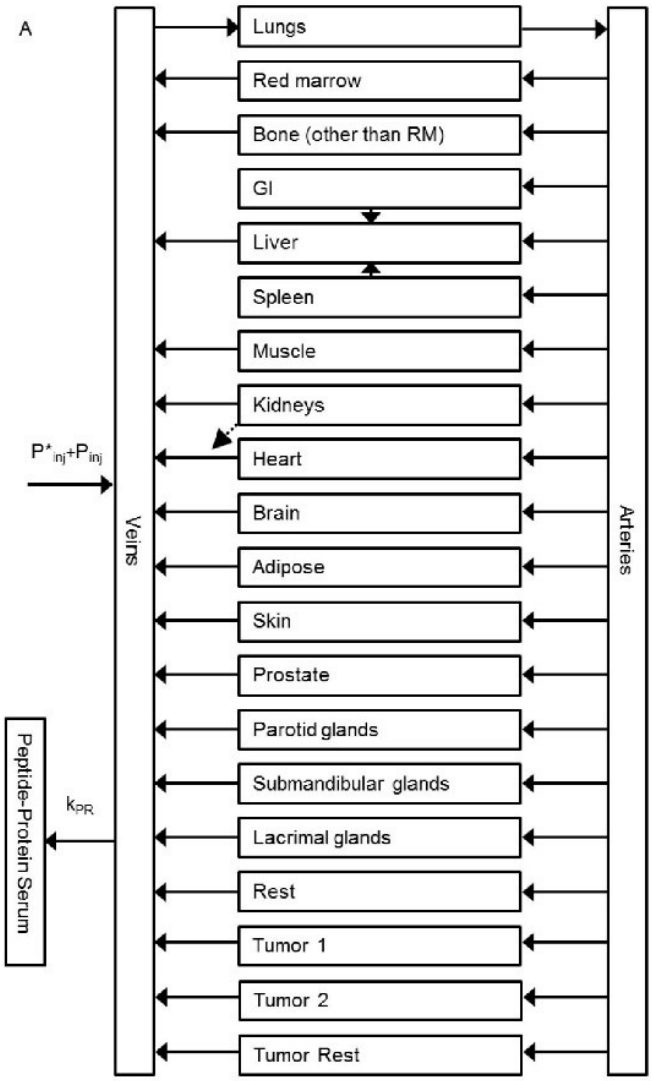

Supplemental Figure A1: Main model structure. All organs are represented by a rectangular compartment and connected via the serum flow. Each organ within this model, except arteries, veins, brain, and protein serum, is divided into subcompartments. The substance is cleared via the kidney. The compartment "Peptide-Protein serum" contains peptide bound to serum protein. As the fraction of bound peptide to proteins is small compared to the total amount and to reduce complexity, only the "veins" were connected to this compartment. The corresponding fraction for each specific organ is considered in the fitting process by assigning the data to the specific compartments.

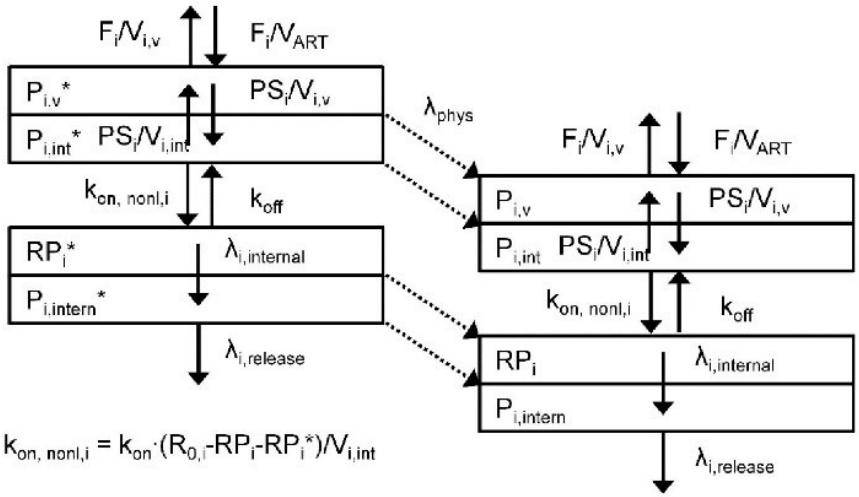

Supplemental Figure A2: GI tract; spleen; prostate; submandibular, lacrimal, and parotid glands; and tumor. The entire model consists of three systems, one for labeled (with *) and one for unlabeled peptide. The systems are connected by the competition for free receptors ($k_{on,nonl,i} = k_{on} \cdot (R_{0,i} - RP_i - RP_i^*)/V_{i,int}$) and by physical decay (λ_{phys}). All physiological parameters are assumed to be equal for the labeled and unlabeled substance. k_{off} is the dissociation rate. The transport of peptide via serum flow to organ i is described by F_i/V_{ART} (where F_i is serum flow and V_{ART} is serum volume of the arteries). $F_i/V_{i,v}$ describes the transport of peptide via serum flow out of organ (where F_i is serum flow and $V_{i,v}$ is serum volume of the respective organ). RP_i is PSMA specific bound peptide to the cell surface. $P_{i,v}$ and $P_{i,int}$ are free peptide of the vascular ($V_{i,v}$) and interstitial spaces ($V_{i,int}$), respectively. PS_i is the permeability surface area product. $\lambda_{i,\ internal}$ is the internalisation rate of bound peptide. $\lambda_{i,\ release}$ is the release rate of ^{177}Lu from the cell.

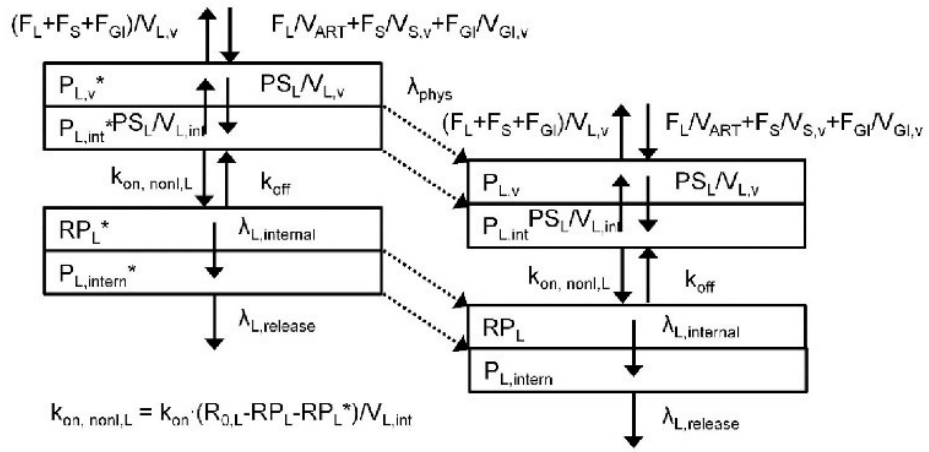

Supplemental Figure A3: Liver. For the liver the model description of Supplemental Figure A2 applies but the serum flow is composed of liver arterial, GI, and spleen flow.

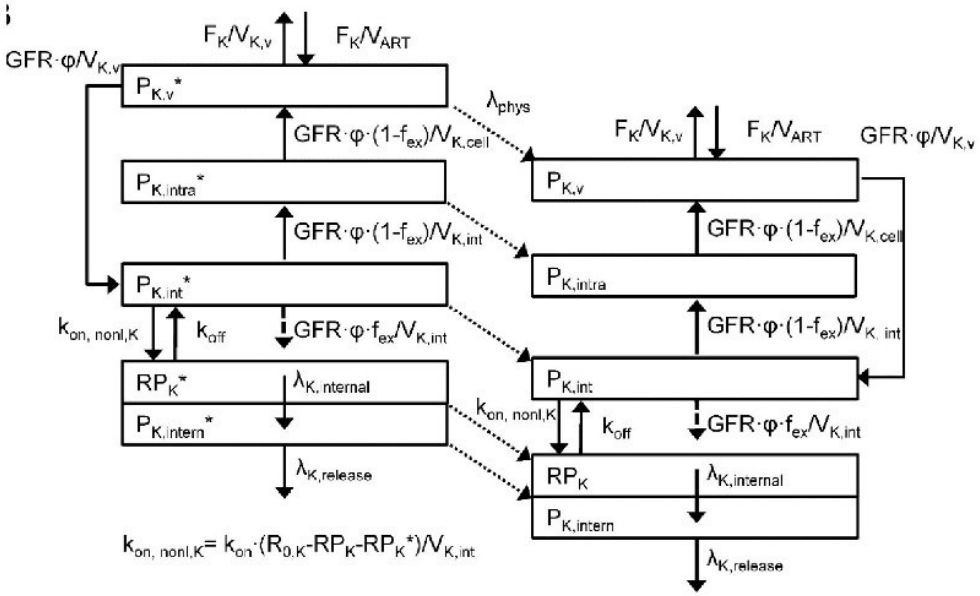

Supplemental Figure A4: Kidneys. The peptide is transported via serum flow to the vascular compartment and then filtrated into the interstitial part. Due to the administration of amino acids, the largest fraction (f_{ex} = 0.96) of peptide is excreted. All unspecific uptake mechanisms are modeled with flow $GFR\cdot\varphi\cdot(1-f_{ex})$ in and out of kidney cells. GFR was measured with Cr-51-EDTA.

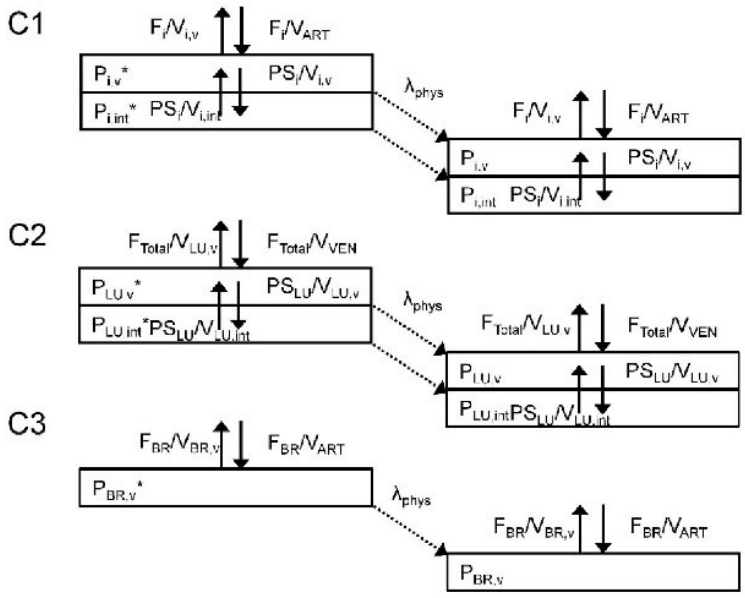

Supplemental Figure A5: PSMA-negative tissue and brain. For adipose, bone (other than red marrow), skin, heart (C1), and lung (C2), the model on the organ level simplifies to the transport of peptide via serum flow and transcapillary extravasation. For brain (C3), the model reduces to serum flow.

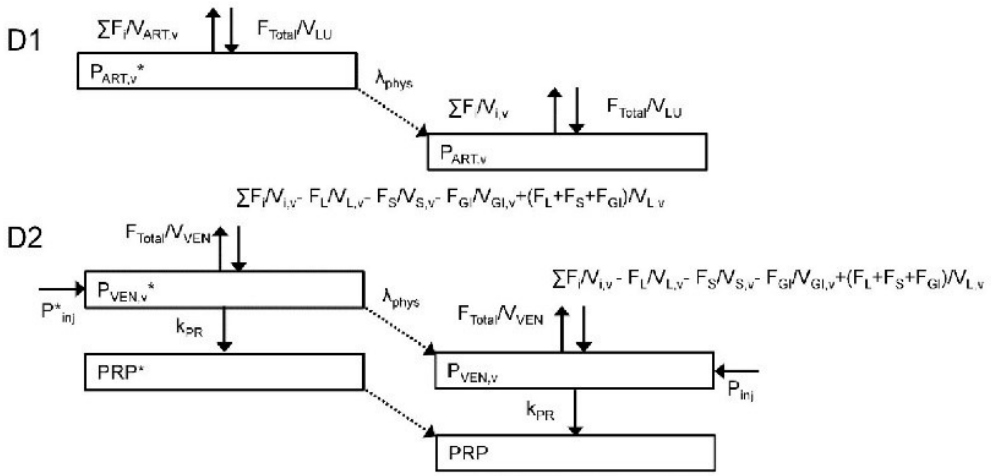

Supplemental Figure A6: Arteries and veins. As the fraction of bound peptide to proteins (PRP) is small compared to the total amount and to reduce complexity, only the "veins (D2)" were connected to PRP. The corresponding fraction for each specific organ is considered in the fitting process by assigning the data to the specific compartments.

References, Part A

1. Rippe B, Haraldsson B. *Fluid and protein fluxes across small and large pores in the microvasculature. Application of two-pore equations*. Acta Physiol Scand. 1987;131(3):411-28.
2. Winter G, Drescher A, Baur B, Solbach C, Reske SN, Beer AJ. *Comparative analysis of chelator-modified peptides for imaging of prostate carcinoma*. Annual Congress EANM. 2014(P200).
3. Leggett RW, Williams LR. *A proposed blood circulation model for reference man*. Health Phys. 1995;69(2):187-201.
4. Buchmann I, Kull T, Glatting G, Bunjes D, Hale G, Kotzerke J, et al. *A comparison of the biodistribution and biokinetics of ^{99}mTc-anti-CD66 mAb BW 250/183 and ^{99}mTc-anti-CD45 mAb YTH 24.5 with regard to suitability for myeloablative radioimmunotherapy*. European journal of nuclear medicine and molecular imaging. 2003;30(5):667-73.
5. Berges RR, Vukanovic J, Epstein JI, CarMichel M, Cisek L, Johnson DE, et al. *Implication of cell kinetic changes during the progression of human prostatic cancer.* Clinical cancer research : an official journal of the American Association for Cancer Research. 1995;1(5):473-80.
6. Buckley DL, Roberts C, Parker GJ, Logue JP, Hutchinson CE. *Prostate cancer: evaluation of vascular characteristics with dynamic contrast-enhanced T1-weighted MR imaging--initial experience*. Radiology. 2004;233(3):709-15.
7. Luczynska E, Heinze-Paluchowska S, Blecharz P, Jereczek-Fossa B, Petralia G, Bellomi M, et al. *Correlation between CT perfusion and clinico-pathological features in prostate cancer: a prospective study*. Medical science monitor : international medical journal of experimental and clinical research. 2015;21:153-62.
8. Franiel T, Lüdemann L, Rudolph B, Rehbein H, Stephan C, Taupitz M, et al. *Prostate MR imaging: tissue characterization with pharmacokinetic volume and blood flow parameters and correlation with histologic parameters*. Radiology. 2009;252(1):101-8.
9. Wang X, Ma D, Olson WC, Heston WD. *In vitro and in vivo responses of advanced prostate tumors to PSMA ADC, an auristatin-conjugated antibody to prostate-specific membrane antigen.* Molecular cancer therapeutics. 2011;10(9):1728-39.
10. Kletting P, Kull T, Maass C, Malik N, Luster M, Beer AJ, et al. *Optimized Peptide Amount and Activity for ^{90}Y-Labeled DOTATATE Therapy.* Journal of nuclear medicine : official publication, Society of Nuclear Medicine. 2016;57(4):503-8.

11. Stabin MG, Sparks RB, Crowe E. *OLINDA/EXM: The Second-Generation Personal Computer Software for Internal Dose Assessment in Nuclear Medicine*. J Nucl Med. 2005;46(6):1023-7.

12. Shah DK, Betts AM. *Towards a platform PBPK model to characterize the plasma and tissue disposition of monoclonal antibodies in preclinical species and human*. Journal of pharmacokinetics and pharmacodynamics. 2012;39(1):67-86.

13. Hollenberg NK, Adams DF, Solomon HS, Rashid A, Abrams HL, Merrill JP. Senescence and the renal vasculature in normal man. Circulation research. 1974;34(3):309-16.

14. Schmidt MM, Wittrup KD. A modeling analysis of the effects of molecular size and binding affinity on tumor targeting. Molecular cancer therapeutics. 2009;8(10):2861-71.

15. Fresco GF, DiGiorgio F, Curti GL. Simultaneous estimation of glomerular filtration rate and renal plasma flow. Journal of nuclear medicine : official publication, Society of Nuclear Medicine. 1995;36(9):1701-6.

16. Kletting P, Muller B, Erentok B, Schmaljohann J, Behrendt FF, Reske SN, et al. Differences in predicted and actually absorbed doses in peptide receptor radionuclide therapy. Medical physics. 2012;39(9):5708-17.

17. Groothuis DR. The blood-brain and blood-tumor barriers: a review of strategies for increasing drug delivery. Neuro-oncology. 2000;2(1):45-59.

18. O'Keefe DS, Bacich DJ, Heston WD. Comparative analysis of prostate-specific membrane antigen (PSMA) versus a prostate-specific membrane antigen-like gene. The Prostate. 2004;58(2):200-10.

19. Antunes P, Ginj M, Zhang H, Waser B, Baum RP, Reubi JC, et al. Are radiogallium-labelled DOTA-conjugated somatostatin analogues superior to those labelled with other radiometals? European journal of nuclear medicine and molecular imaging. 2007;34(7):982-93.

20. Velikyan I, Sundin A, Eriksson B, Lundqvist H, Sorensen J, Bergstrom M, et al. In vivo binding of [^{68}Ga]-DOTATOC to somatostatin receptors in neuroendocrine tumours--impact of peptide mass. Nucl Med Biol. 2010;37(3):265-75.

21. Snyder WS, Cook MJ, Nasset ES, Karhausen RS, Howells GP. Report of the Task Group on Reference Man. ICRP publication 23. Oxford: Elsevier; 1975.

22. Berggreen E, Wiig H. Lowering of interstitial fluid pressure in rat submandibular gland: a novel mechanism in saliva secretion. American journal of physiology Heart and circulatory physiology. 2006;290(4):H1460-8.

23. Kletting P, Schuchardt C, Kulkarni HR, Shahinfar M, Singh A, Glatting G, et al. Investigating the Effect of Ligand Amount and Injected Therapeutic Activity: A Simulation Study for ^{177}Lu-Labeled PSMA-Targeting Peptides. PloS one. 2016;11(9):e0162303.

24. Rumboldt Z, Al-Okaili R, Deveikis JP. Perfusion CT for head and neck tumors: pilot study. AJNR Am J Neuroradiol. 2005;26(5):1178-85.

25. Ben Jemaa A, Bouraoui Y, Sallami S, Banasr A, Ben Rais N, Ouertani L, et al. Co-expression and impact of prostate specific membrane antigen and prostate specific antigen in prostatic pathologies. J Exp Clin Cancer Res. 2010;29:171.

26. Weineisen M, Schottelius M, Simecek J, Baum RP, Yildiz A, Beykan S, et al. ^{68}Ga- and ^{177}Lu-Labeled PSMA I&T: Optimization of a PSMA-Targeted Theranostic Concept and First Proof-of-Concept Human Studies. Journal of nuclear medicine : official publication, Society of Nuclear Medicine. 2015;56(8):1169-76.

27. Eder M, Schafer M, Bauder-Wust U, Hull WE, Wangler C, Mier W, et al. ^{68}Ga-complex lipophilicity and the targeting property of a urea-based PSMA inhibitor for PET imaging. Bioconjugate chemistry. 2012;23(4):688-97.

28. Hobbs RF, Sgouros G. Calculation of the biological effective dose for piecewise defined dose-rate fits. Med Phys. 2009;36(3):904-7.

29. Stabin MG, Siegel JA. Physical models and dose factors for use in internal dose assessment. Health Phys. 2003;85(3):294-310.

30. Cremonesi M, Botta F, Di Dia A, Ferrari M, Bodei L, De Cicco C, et al. Dosimetry for treatment with radiolabelled somatostatin analogues. A review. Q J Nucl Med Mol Imaging. 2010;54(1):37-51.

31. Fowler J, Chappell R, Ritter M. Is alpha/beta for prostate tumors really low? International Journal of Radiation Oncology Biology Physics. 2001;50(4):1021-31.

32. Konijnenberg M. From imaging to dosimetry and biological effects. Q J Nucl Med Mol Imaging. 2011;55(1):44-56.

Part B: Background Corrections

Assigning tumor data from planar scintigraphy to model compartments

For fitting the model parameters to the data derived from the therapeutic planar images, the following equation was used to assign the tumor data to the compartments of the PBPK model:

$$a_{TU,Therapy}(t) = \frac{\left[P^*_{TU,v}(t)+P^*_{TU,int}(t)+RP^*_{TU}(t)+P^*_{TU,intern}(t)+\frac{(A_{ROI,TU}\cdot h_{PET,TU})}{(V_{MUS,total}+V_{ADI,total})}\cdot(P^*_{MUS,v}(t)+P^*_{MUS,int}(t)+P^*_{ADI,v}(t)+P^*_{ADI,int}(t))\right]}{amount_{injected,thera}\cdot f_{hot,thera}} \quad \text{(Eq. B1)}$$

where $a(t)$ is the fraction of administered activity of a specific tumor ROI, $amount_{injected}$ is the total injected therapy amount, f_{hot} is the fraction of labeled peptide, $A_{ROI,T}$ is the area of the drawn ROI in the planar image, $h_{PET,TU}$ is the patient thickness (minus tumor diameter) at the particular location of the tumor measured in the PET/CT image, $V_{MUS,total}$ and $V_{ADI,total}$ are the total muscle and adipose volume (part A of the supplemental materials), and $P^*_{TU,v}(t) + P^*_{TU,int}(t) + RP^*_{TU}(t) + P^*_{TU,intern}(t)$ are the amounts of labeled peptide in the vascular, interstitial, bound, and internalized tumor compartments, respectively. $P^*_{MUS,v}(t)$, $P^*_{MUS,int}(t)$, $P^*_{ADI,v}(t)$ and $P^*_{ADI,int}(t)$ describe the amounts of labeled peptide in the vascular and interstitial spaces of muscle and adipose tissue, respectively. For tumor dose calculation, only compartments pertaining to the tumor were used. The fraction of peptide bound to protein blood was neglected.

Assigning tumor data from PET/CT to model compartments

For fitting the model parameters to the data derived from the pretherapeutic PET/CT images, the following equation was used to assign the data to the compartments of the PBPK model:

$$a_{TU,PET}(t) = \frac{\left[P^*_{TU,v}(t)+P^*_{TU,int}(t)+RP^*_{TU}(t)+P^*_{TU,intern}(t)+\frac{(V_{VOI,TU,2}-V_{VOI,TU,1})}{(V_{MUS,total}+V_{ADI,total})}\left(P^*_{MUS,v}(t)+P^*_{MUS,int}(t)+P^*_{ADI,v}(t)+P^*_{ADI,int}(t)\right)\right]}{amount_{injected,PET}\cdot f_{hot,PET}} \quad \text{(Eq. B2)}$$

where $V_{VOI,TU,1}$ is the estimated volume using the pretherapeutic PET image with a threshold of 20%–50% so that the CT tumor volume and the PET match. $V_{VOI,TU,2}$ is the estimated volume using the pretherapeutic PET image with a threshold of 10%–20%, leading to a 5-mm-larger radius (i.e., one voxel) than for $V_{VOI,TU,2}$ to get all activity contained in the tumor. The activity derived using $V_{VOI,TU,2}$ was used as data point $a_{TU,PET}(t)$ and was indirectly background-corrected using the above described data assignment.

Assigning tumor REST data from PET/CT to model compartments

For tumor remainder (REST), the following equation was used in the fitting of model parameters to the data derived from the pretherapeutic PET/CT images:

$$a_{TU,Rest,PET}(t) = \frac{\left[P^*_{TU,Rest,v}(t)+P^*_{TU,Rest,int}(t)+RP^*_{TU,Rest}(t)+P^*_{TU,Rest,intern}(t)+\frac{V_{VOI,TU,Rest}\ (1-x_V)}{(V_{MUS,total}+V_{ADI,total})}\left(P^*_{MUS,v}(t)+P^*_{MUS,int}(t)+P^*_{ADI,v}(t)+P^*_{ADI,int}(t)\right)\right]}{amount_{injected,PET}\cdot f_{hot,PET}} \quad \text{(Eq. B3)}$$

where x_V is the correction factor to get the actual tumor volume (this information is implicitly contained in the total-body images during therapy). $a_{TU,Rest,PET}(t)$ was derived with a threshold of 15%–20%.

Assigning kidney data from PET/CT to model compartments

$$a_{K,PET}(t) = \frac{\left[P^{*}_{K,v}(t)+P^{*}_{K,int}(t)+RP^{*}_{K}(t)+P^{*}_{K,intern}(t)+P^{*}_{K,v}(t)+\frac{(V_{VOI,K}-V_{K,total})}{(V_{MUS,total}+V_{ADI,total})}\cdot(P^{*}_{MUS,v}(t)+P^{*}_{MUS,int}(t)+P^{*}_{ADI,v}(t)+P^{*}_{ADI,int}(t))\right]}{amount_{injected,PET}\cdot f_{hot,PET}} \quad \text{(Eq. B4)}$$

where $V_{VOI,K}$ is the volume used for activity quantification with a threshold of 10%–20%, leading to a 5-mm-larger radius (i.e., one voxel) than that of the kidney volume, $V_{K,total}$, estimated using the CT.

Supplemental Table B1: Patient data and measurement

Patient no.	Age	BSA [m²]	PSA [ng/ml]	Measured volumes [ml]						PET		Therapy		ΔT* [d]
				Kidneys	Submandibular glands	Parotid glands	Tumor lesion 1	Tumor lesion 2	Tumor REST	Activity [MBq]	Amount [nmol]	Activity [GBq]	Amount [nmol]	
P1	66	2.0	513	372	17	39	9.4	19	201	123	1.55	7155	87	20
P2	75	1.8	49	273	17	46	2.1	4.2	130	105	1.65	7019	85	21
P3	72	2.0	31	304	13	43	14	52	156	147	1.72	6471	80	13
P4	66	1.9	97	282	14	26	14	31	370	134	1.10	7170	87	21
P5	74	1.9	47	281	19	44	26	17	686	122	1.78	7510	92	18
P6	58	2.7	2905	400	13	36	81	92	5620	130	1.82	7700	94	8
P7	64	1.9	0.23	278	16	21	48	37	17	104	1.65	7780	95	35
P8	73	2.0	1193	233	18	45	5.7	19	429	116	1.45	7205	88	12
P9	77	1.8	2547	256	12	41	15	8.7	1481	117	1.68	7380	90	63
P10	63	2.0	2471	392	13	40	1.9	5.3	252	102	2.21	7552	93	15
P11	73	1.8	7	305	21	39	0.33	1.2	10	100	1.82	7200	92	20
P12	74	2.1	161	297	13	59	9.9	8.7	217	99	1.19	7562	97	21
P13	74	2.1	133	348	13	48	5.9	2.0	17	97	1.96	7464	96	19
Mean	70	2.0	781	309	15.2	40.6	18	23	737	115	1.66	7321	91	22
SD	6	0.1	1112	53	3.0	9.7	23	26	1519	16	0.30	344	5	14

*ΔT = time between PET and therapy.

Supplemental Table B2: Patient measurement time after injection

Patient no.	Measurement times (h)				
P1	1.1	22	44	70	166
P2	1.3	18		66	163
P3	0.5	18	46	68	165
P4	2.2	19	47	67	164
P5	0.3	23			160
P6	0.3	21			164
P7	2.1	25			163
P8	0.4	22			167
P9	0.6	20			165
P10	0.2	20			162
P11	0.3	18			162
P12	0.3	21			163
P13	0.2	17			161

Part C: Results

This part of the supplemental materials provides the fitting and simulation results. Supplemental Figure C1 shows an example of the fitted curves, Supplemental Table C1 contains the population parameters, Supplemental Table C2 contains the individual parameters after the fitting process, Supplemental Tables C3A and C3B contain all BEDs and absorbed doses for each volume and patient, Supplemental Table C4 contains the optimal combinations of activity and peptide amount for a kidney BED of 5 $Gy_{2.5}$, and Supplemental Table C5 contains the S values and radiobiological parameters for the calculation of the red marrow dose.

Supplemental Figure C1: Typical fit (P4)

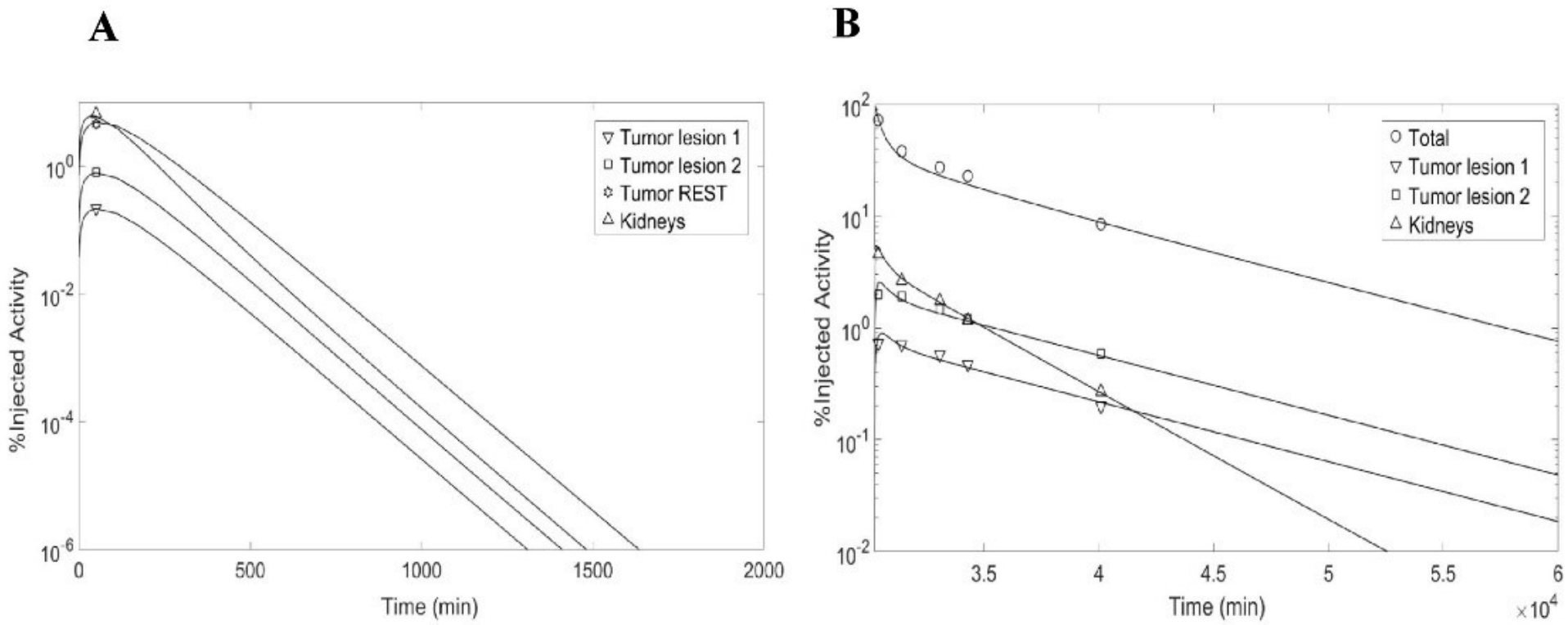

Simultaneous fit of PET (A) and planar imaging data (B). Different amounts of peptide, molecular sizes, and the pertaining binding rates are taken into account. The injection for PET/CT (A) starts at t = 0. Tumor growth is assumed between PET and therapeutic injection (B).

Supplemental Table C1: Population parameters

Quantity	Organ	Parameter	Unit	Mean	SD
PSMA receptor density	kidneys	$[R_{K,0}]$	$nmol \cdot l^{-1}$	18	2.9
	tumor lesion	$[R_{TU,0}]$		46	23
	tumor REST	$[R_{TU,REST,0}] = x_r \cdot ([R_{TU,1,0}] + [R_{TU,2,0}])/2$			
		x_r	unity	1.4	
Release rate	kidneys	$\lambda_{K,release}$	min^{-1}	$2.3 \cdot 10^{-4}$	$5.9 \cdot 10^{-5}$
	tumor	$\lambda_{TU,release}$	min^{-1}	$1.4 \cdot 10^{-4}$	$5.7 \cdot 10^{-5}$
Serum flow density	tumor lesion	$f_{TU,0}$	$ml \cdot min^{-1} \cdot g^{-1}$	0.20	0.32
	tumor REST	$f_{TU,REST} = x_f \cdot (f_{TU,1} + f_{TU,2})/2$	$ml \cdot min^{-1} \cdot g^{-1}$		
		x_f	unity	0.53	$7.0 \cdot 10^{-5}$
	kidneys	$f_K = f_{K,C} - 0.026 \cdot Age$	$ml \cdot min^{-1} \cdot g^{-1}$		
		$f_{K,C}$	$ml \cdot min^{-1} \cdot g^{-1}$	4.3	0.65
Volume tumor REST		$V_{TU,REST,total} = x_V \cdot V_{VOI,TU,REST}$	l		
		x_v	unity	0.64	0.26
Filtrated fraction of blood blow		x_k	unity	0.18	

Each patient model was fitted separately using an iterative fitting. After each iteration, the means and standard deviations were obtained and used as Bayesian information in the next step, until convergence. The population fit converged after 12 iterations. The information (number of receptors) about the remaining tumor is contained in the total-body scan, and only one PET measurement is available. Therefore, three coefficients (x_r, x_f, and x_v) were estimated for each patient and used as correction factors in the calculations. Values with no standard deviation were automatically fixed during the fitting process if the standard deviation became very small.

Supplemental Table C2: Final individual patient parameters

	PSMA receptor density [$R_{i,0}$]			Release rate $\lambda_{i,0,release}$		Serum flow density $f_{TU,0}$		Kidney blood flow $f_{K,C}$	Measured tumor REST volume
Unit	**nmol·l^{-1}**			**min^{-1}**		**ml·min^{-1}·g^{-1}**		**ml·min^{-1}·g^{-1}**	**l**
	Kidneys	**Tumor lesion 1**	**Tumor lesion 2**	**Kidneys**	**Tumor**	**Tumor lesion 1**	**Tumor lesion 2**		
P1	13	87	94	2.4×10^{-4}	1.6×10^{-4}	0.42	0.27	4.1	0.20
P2	17	73	52	2.1×10^{-4}	2.1×10^{-4}	0.32	0.57	5.1	0.13
P3	23	7.2	4.0	3.0×10^{-4}	2.3×10^{-4}	0.070	0.11	4.9	0.16
P4	20	78	87	1.9×10^{-4}	5.2×10^{-5}	0.13	0.26	4.4	0.37
P5	19	33	64	2.2×10^{-4}	1.0×10^{-4}	0.078	0.060	3.7	0.69
P6	14	46	27	1.2×10^{-4}	8.3×10^{-5}	0.051	0.046	2.9	5.6
P7	19	17	33	3.0×10^{-4}	1.3×10^{-4}	0.067	0.073	3.9	0.017
P8	17	60	43	1.7×10^{-4}	1.1×10^{-4}	0.12	0.13	3.6	0.43
P9	16	45	63	1.5×10^{-4}	7.2×10^{-5}	0.060	0.050	4.3	1.5
P10	15	68	21	2.8×10^{-4}	1.8×10^{-4}	0.21	0.095	4.3	0.25
P11	21	41	23	2.7×10^{-4}	2.0×10^{-4}	0.074	0.070	4.3	0.010
P12	19	10	18	1.9×10^{-4}	1.6×10^{-4}	0.037	0.045	4.8	0.2
P13	16	19	87	3.0×10^{-4}	1.9×10^{-4}	0.12	1.7	5.2	0.017

Starting values for receptor densities (1), release rates (1), and blood flow to tumor (2) and kidneys (3) were taken from the literature.

Supplemental Table C3A: Effect of total tumor volume on the BED

Patient no.	Tissue	BED for different total tumor volumes [$Gy_{1.49}$]				
		0.1 L	0.3 L	1 L	3 L	10 L
P1	kidneys	3.7	3.4	2.5	1.4	0.58
	1	35	32	23	12	4.6
	2	38	34	24	12	4.5
	REST	47	41	28	13	4.6
	submandibular	9.4	8.6	6.4	3.5	1.3
	parotid	9.5	8.7	6.4	3.5	1.3
P2	kidneys	5.2	5.0	4.0	2.3	0.91
	1	25	23	18	9.9	3.6
	2	17	16	13	7.5	2.9
	REST	29	27	21	11	3.8
	submandibular	9.8	9.3	7.3	4.1	1.5
	parotid	9.8	9.4	7.4	4.1	1.5
P3*	kidneys	5.4	5.4	5.4	5.2	4.2
	1	1.8	1.8	1.8	1.8	1.5
	2	1.0	1.0	1.0	1.0	0.85
	REST	1.9	1.9	1.9	1.8	1.5
	submandibular	8.4	8.4	8.3	7.9	6.2
	parotid	8.5	8.5	8.4	8.0	6.3
P4	kidneys	7.2	6.6	4.9	2.9	1.2
	1	52	47	34	18	6.9
	2	61	56	42	23	9.0
	REST	66	58	40	21	7.5
	submandibular	10	9.3	7.1	4.1	1.7
	parotid	10	9.3	7.1	4.2	1.7
P5	kidneys	10	9.5	7.4	4.6	2.1
	1	24	23	18	12	5.3
	2	46	42	32	19	7.5
	REST	38	35	26	15	5.7
	submandibular	16	15	12	7.4	3.4
	parotid	16	15	12	7.4	3.4
P6	kidneys	8.8	8.4	7.2	5.1	2.6
	1	31	30	25	17	8.2
	2	19	18	15	11	5.6
	REST	24	23	19	13	5.8
	submandibular	14	13	11	8.1	4.2
	parotid	14	13	11	8.2	4.2
P7	kidneys	7.5	7.2	6.4	4.7	2.3
	1	9.6	9.3	8.4	6.4	3.3
	2	19	19	17	12	6.0
	REST	18	17	15	11	4.9
	submandibular	14	13	12	9	4
	parotid	14	13	12	9	4
P8	kidneys	12	11	7.8	4.2	1.7
	1	52	46	33	17	6.4
	2	37	33	24	13	5.1
	REST	54	47	32	16	5.6
	submandibular	18	16	12	6.5	2.6
	parotid	18	16	12	6.6	2.6
P9	kidneys	7.8	7.4	6.1	4.2	2.1
	1	29	27	23	16	7.3
	2	37	34	28	18	8.1
	REST	29	27	22	14	6.1
	submandibular	12	11	9.5	6.7	3.4
	parotid	12	11	9.6	6.7	3.4
P10	kidneys	3.7	3.6	3.2	2.2	1.1

	1	23	22	19	13	5.8
	2	6.2	6.1	5.4	3.9	1.9
	REST	18	18	15	9.5	4.0
	submandibular	8.8	8.6	7.5	5.3	2.4
	parotid	8.9	8.6	7.6	5.3	2.5
P11	kidneys	7.4	7.1	6.3	4.5	2.2
	1	15	15	13	9.3	4.4
	2	8.2	8.0	7.1	5.3	2.7
	REST	15	14	12	8.1	3.5
	submandibular	11	11	9.8	7.2	3.6
	parotid	11	11	9.9	7.2	3.6
P12	kidneys	7.0	6.9	6.6	5.7	3.7
	1	3.9	3.9	3.7	3.3	2.2
	2	6.9	6.8	6.5	5.7	3.7
	REST	6.9	6.8	6.4	5.4	3.3
	submandibular	10	10	9.9	8.7	5.6
	parotid	11	10	10	8.8	5.7
P13	kidneys	3.3	3.3	2.9	1.9	0.8
	1	5.1	5.1	4.5	2.9	1.2
	2	26	26	23	14	5.5
	REST	21	21	18	11	4.2
	submandibular	7.9	7.7	6.7	4.0	1.5
	parotid	8.0	7.8	6.7	4.1	1.6
Mean±SD	kidney	6.9±2.6	6.5±2.3	5.4±1.8	3.7±1.4	2.0±1.1
	tumor	26±17	24±15	18±11	11±5.6	4.7±2.1
	submandibular	11±3.0	11±2.7	9.2±2.1	6.3±1.9	3.2±1.6
	parotid	12±3.1	11±2.7	9.2±2.1	6.4±1.9	3.3±1.6

Supplemental Table C3B: Effect of total tumor volume on the absorbed dose

Patient no.	Tissue	Absorbed dose for different total tumor volumes [Gy]				
		0.1 L	0.3 L	1 L	3 L	10 L
P1	kidneys	3.4	3.1	2.4	1.4	0.57
	1	29	27	20	11	4.4
	2	31	28	21	12	4.4
	REST	37	34	24	12	4.5
	submandibular	8.5	7.8	5.9	3.3	1.3
	parotid	8.5	7.9	6.0	3.4	1.3
P2	kidneys	4.6	4.5	3.6	2.2	0.89
	1	21	20	16	9.2	3.5
	2	15	14	12	7.1	2.8
	REST	24	23	18	9.9	3.7
	submandibular	8.8	8.4	6.8	3.9	1.5
	parotid	8.8	8.5	6.8	3.9	1.5
P3*	kidneys	4.6	4.6	4.6	4.5	3.7
	1	1.8	1.8	1.8	1.7	1.5
	2	1.0	1.0	1.0	1.0	0.85
	REST	1.8	1.8	1.8	1.8	1.5
	submandibular	7.6	7.6	7.5	7.3	5.8
	parotid	7.7	7.7	7.6	7.3	5.9
P4	kidneys	6.2	5.7	4.4	2.7	1.2
	1	44	40	30	17	6.7
	2	51	47	36	22	8.7
	REST	54	49	35	19	7.3
	submandibular	9.0	8.4	6.5	3.9	1.6
	parotid	9.1	8.4	6.6	4.0	1.6
P5	kidneys	8.4	7.9	6.4	4.1	2.0
	1	22	21	17	11	5.1
	2	38	35	28	17	7.3
	REST	33	30	23	14	5.5
	submandibular	14	13	10	6.8	3.3
	parotid	14	13	10	6.9	3.3
P6	kidneys	7.7	7.4	6.4	4.6	2.4
	1	28	26	23	16	7.9
	2	17	17	14	11	5.4
	REST	22	21	18	12	5.6
	submandibular	12	12	10	7.4	4.0
	parotid	12	12	10	7.5	4.0
P7	kidneys	6.2	6.0	5.4	4.1	2.2
	1	9.0	8.8	8.0	6.1	3.3
	2	17	17	15	11	5.8
	REST	16	16	14	10	4.7
	submandibular	12	12	11	8.1	4.2
	parotid	12	12	11	8.1	4.2
P8	kidneys	10	9.1	6.7	3.8	1.6
	1	42	38	28	16	6.2
	2	31	28	21	12	5.0
	REST	44	39	28	15	5.4
	submandibular	16	14	11	6.1	2.5
	parotid	16	14	11	6.1	2.5
P9	kidneys	6.8	6.5	5.5	3.9	2.0
	1	26	25	21	15	7.1
	2	32	30	25	17	7.9
	REST	26	25	20	13	5.9
	submandibular	11	10	8.6	6.2	3.3
	parotid	11	10	8.7	6.2	3.3
P10	kidneys	3.3	3.2	2.9	2.1	1.0
	1	19	19	17	12	5.5

	2	5.9	5.8	5.2	3.8	1.9
	REST	16	16	13	8.9	3.9
	submandibular	8.0	7.8	6.9	5.0	2.4
	parotid	8.0	7.8	7.0	5.0	2.4
P11	kidneys	6.1	6.0	5.4	4.0	2.1
	1	14	13	12	8.7	4.2
	2	7.7	7.5	6.7	5.1	2.6
	REST	14	13	11	7.6	3.5
	submandibular	10	9.9	8.9	6.7	3.5
	parotid	10	9.9	8.9	6.7	3.5
P12	kidneys	6.0	6.0	5.8	5.1	3.4
	1	3.8	3.8	3.6	3.2	2.2
	2	6.6	6.5	6.2	5.5	3.7
	REST	6.6	6.5	6.2	5.2	3.2
	submandibular	9.4	9.3	8.9	7.9	5.3
	parotid	9.5	9.4	9.0	8.0	5.4
P13	kidneys	3.0	3.0	2.7	1.8	0.75
	1	4.9	4.9	4.4	2.9	1.2
	2	22	22	19	13	5.2
	REST	18	18	16	10	4.1
	submandibular	7.2	7.1	6.2	3.9	1.5
	parotid	7.3	7.1	6.2	3.9	1.5
Mean±SD	kidney	5.9±2.1	5.6±1.9	4.8±1.5	3.4±1.2	1.8±1.0
	tumor	22±14	20±13	16±9	11±5.0	4.7±2.0
	submandibular	10±2.5	10±2.2	8.3±1.7	5.9±1.7	3.1±1.5
	parotid	10±2.5	10±2.2	8.4±1.7	5.9±1.7	3.1±1.5

Supplemental Table C3C: Effect of total tumor volume on the BED for a different (4) α/β but equal α

		BED for different total tumor volumes [$Gy_{1.8}$]				
Patient no.	**Tissue**	**0.1 L**	**0.3 L**	**1 L**	**3 L**	**10 L**
P1	kidneys	3.7	3.4	2.5	1.4	0.6
	1	34	31	23	12	5
	2	37	33	24	12	4
	REST	45	40	27	13	5
P2	kidneys	5.2	5.0	4.0	2.3	0.9
	1	24	23	18	9.8	3.6
	2	16	16	13	7.4	2.9
	REST	28	26	20	11	3.8
P3*	kidneys	5.4	5.4	5.4	5.2	4.2
	1	1.8	1.8	1.8	1.7	1.5
	2	1.0	1.0	1.0	1.0	0.9
	REST	1.9	1.9	1.9	1.8	1.5
P4	kidneys	7.2	6.6	4.9	2.9	1.2
	1	50	45	33	18	6.9
	2	59	54	41	23	8.9
	REST	64	57	39	20	7.4
P5	kidneys	10	9.5	7.4	4.6	2.1
	1	24	22	18	12	5.2
	2	44	41	31	19	7.5
	REST	37	34	25	14	5.7
P6	kidneys	8.8	8.4	7.2	5.1	2.6
	1	30	29	25	17	8.2
	2	19	18	15	11	5.5
	REST	24	23	19	13	5.8
P7	kidneys	7.5	7.2	6.4	4.7	2.3
	1	9.5	9.2	8.3	6.3	3.3
	2	19	18	16	12	6.0
	REST	18	17	15	11	4.8
P8	kidneys	12	11	7.8	4.2	1.7
	1	50	45	32	17	6.4
	2	36	32	23	13	5.1
	REST	52	46	31	16	5.5
P9	kidneys	7.8	7.4	6.1	4.2	2.1
	1	28	27	22	15	7.3
	2	36	33	27	18	8.1
	REST	29	27	22	14	6.0
P10	kidneys	3.7	3.6	3.2	2.2	1.1
	1	22	21	19	13	5.7
	2	6.2	6.0	5.4	3.9	1.9
	REST	18	17	15	9.4	4.0
P11	kidneys	7.4	7.1	6.3	4.5	2.2
	1	15	14	13	9.2	4.4
	2	8.1	7.9	7.1	5.2	2.7
	REST	15	14	12	8.0	3.5
P12	kidneys	7.0	6.9	6.6	5.7	3.7
	1	3.9	3.8	3.7	3.3	2.2
	2	6.8	6.7	6.5	5.7	3.7
	REST	6.8	6.7	6.4	5.4	3.3
P13	kidneys	3.3	3.3	2.9	1.9	0.8
	1	5.1	5.0	4.5	2.9	1.2
	2	25	25	22	14	5.4
	REST	20	20	17	11	4.2
Mean±SD	kidney	6.8±2.5	6.5±2.3	5.4±1.7	3.8±1.4	2.0±1.1
	tumor	25±16	22±15	18±10	11±5.4	4.9±2.0

Supplemental Table C4: Optimal activity and peptide amount

Patient no.	Actually administered		Tumor	Optimal for kidney BED 5 $Gy_{2.5}$					
	Amount (nmol)	Activity (MBq)		Amount (nmol)	Activity (MBq)	Tumor BED ($Gy_{1.49}$)	Submandibuar BED ($Gy_{4.5}$)	Parotid BED ($Gy_{4.5}$)	Red marrow BED (Gy_{15})
P1	87	7155	1	128	11659	48 (4)†	12.5	12.6	0.24
			2	128	11659	52 (3)	12.5	12.6	0.24
			REST	256	16468	69 (3)	12.1	12.2	0.30
P2	85	7019	1	64	6015	23 (7)	9.2	9.2	0.11
			2	32	4785	16 (10)	8.7	8.8	0.095
			REST	128	8280	27 (6)	9.2	9.2	0.15
P3*	80	6471	1	8192*	89777*	1.8 (84)	4.6	4.6	1.1
			2	8192*	89777*	1.4 (104)	4.6	4.6	1.1
			REST	8192*	89777*	1.8 (84)	4.6	4.6	1.1
P4	87	7170	1	256	9638	37 (5)	6.9	7.0	0.30
			2	128	6998	43 (4)	7.1	7.1	0.25
			REST	256	9638	53 (3)	6.9	7.0	0.30
P5	92	7510	1	128	5741	12 (13)	7.8	7.8	0.22
			2	256	7876	24 (7)	7.6	7.6	0.29
			REST	512	11569	23 (7)	7.3	7.4	0.38
P6	94	7700	1	256	14964	20 (8)	8.0	8.0	0.81
			2	256	14964	12 (13)	8.0	8.0	0.81
			REST	512	18680	19 (8)	7.7	7.8	0.97
P7	95	7780	1	64	4613	6.7 (23)	9.2	9.2	0.10
			2	128	6418	13 (12)	9.2	9.2	0.14
			REST	256	9525	13 (12)	8.9	9.0	0.20
P8	88	7205	1	128	4556	21 (8)	7.5	7.6	0.18
			2	128	4556	15 (10)	7.5	7.6	0.18

			REST	256	6325	24 (7)	7.4	7.4	0.24
P9	90	7380	1	256	12035	20 (8)	7.6	7.7	0.61
			2	256	12035	28 (6)	7.6	7.7	0.61
			REST	512	16138	30 (5)	7.3	7.4	0.75
P10	93	7552	1	128	11744	31 (5)	11.7	11.8	0.18
			2	64	8743	8.3 (19)	11.6	11.7	0.14
			REST	256	17010	26 (6)	11.4	11.5	0.24
P11	92	7200	1	128	6027	11 (14)	7.7	7.8	0.11
			2	64	4241	5.7 (27)	7.8	7.8	0.078
			REST	256	9102	11 (14)	7.6	7.6	0.16
P12	97	7562	1	128	6503	2.9 (52)	7.5	7.6	0.10
			2	128	6503	5.0 (30)	7.5	7.6	0.10
			REST	256	9624	5.3 (29)	7.3	7.4	0.14
P13	96	7464	1	64	8921	7.5 (20)	11.5	11.6	0.11
			2	64	8921	40 (4)	11.5	11.6	0.11
			REST	64	8921	32 (5)	11.5	11.6	0.11
Mean	91	7321		807	15660	22	8.5	8.6	0.35
Median	92	7380		128	9102	16 (8)	7.7	7.8	0.22
Range	80-97	6471-7780		32-8192	4241-89777	1.4-69	4.6-12.5	4.6-12.6	0.08-1.1
For patient with total tumor REST volume > 0.3 l									
Mean	90	7393			273	10381			
Median	6	90			256	9638			
Range	87-94	7170-7700			128-512	4556-18680			

*This can be regarded as purely theoretical result. The receptor density is very low in the tumor lesions. For this patient there is no favorable (>1) BED_{Tumor}/BED_{Kidney} ratio.
†The number of cycles required to reach a BED of 150 $Gy_{1.49}$, which is comparable to 156 $Gy_{1.8}$ reported by Dearnaley et. al [4] for an absorbed dose of 74 Gy.

BED red marrow

The calculation of the BED of the red marrow is challenging, especially for patients with highly advanced disease and possible red marrow infiltration. Based on currently available models, we have calculated a BED for the red marrow to identify whether the red marrow might be dose-limiting for the optimal combination of activity and peptide amount regarding BED_{Tumor}/BED_{Kidney}.

The BED of the red marrow was calculated using Eq. A18 and a dose rate of:

$$\dot{D}_{RM} = A_{RM}(t) \cdot S_{RM \leftarrow RM} + \sum_i A_i(t) \cdot S_{RM \leftarrow i} + A_{REM}(t) \cdot S_{RM \leftarrow REM} \qquad \text{(Eq. C1)}$$

with i = liver, spleen, kidney, lung, muscle, and bone. A_{REM} contains the activity of the tumor 1, tumor 2, and tumor remainder.

Supplemental Table C5: S values and radiobiological parameters for red marrow

Variable		Value	Unit	Source
$S_{RM \leftarrow RM}$	dose factor red marrow to red marrow phantom (are scaled using BW)	$7.1 \cdot 10^{-7}$	$Gy \cdot min^{-1} \cdot MBq^{-1}$	(5)
$S_{RM \leftarrow REM}$	dose factor remainder to red marrow corrected individually according to Hindorf et al.	$1.0 \cdot 10^{-8}$ 1.0 to $1.2 \cdot 10^{-8}$	$Gy \cdot min^{-1} \cdot MBq^{-1}$	(5, 6)
$S_{RM \leftarrow K}$	dose factor kidney to red marrow	$2.8\ 10^{-9}$	$Gy \cdot min^{-1} \cdot MBq^{-1}$	
$S_{RM \leftarrow L}$	dose factor liver to red marrow	$1.4 \cdot 10^{-9}$	$Gy \cdot min^{-1} \cdot MBq^{-1}$	
$S_{RM \leftarrow LU}$	dose factor lung to red marrow	$1.8 \cdot 10^{-9}$	$Gy \cdot min^{-1} \cdot MBq^{-1}$	
$S_{RM \leftarrow MUS}$	dose factor muscles to red marrow	$1.5 \cdot 10^{-9}$	$Gy \cdot min^{-1} \cdot MBq^{-1}$	
$S_{RM \leftarrow BONE}$	dose factor bone to red marrow	$1.0 \cdot 10^{-7}$	$Gy \cdot min^{-1} \cdot MBq^{-1}$	
$S_{RM \leftarrow S}$	dose factor spleen to red marrow	$1.4 \cdot 10^{-9}$	$Gy \cdot min^{-1} \cdot MBq^{-1}$	
α/β_{RM}	radiobiological parameters red marrow	15	Gy	(7)
μ_{RM}	repair rate red marrow	ln(2)/60/1.5	min^{-1}	(7)

References, Parts B and C

1. Kletting P, et al. *Investigating the Effect of Ligand Amount and Injected Therapeutic Activity: A Simulation Study for ^{177}Lu-Labeled PSMA-Targeting Peptides.* PLoS One. 2016;11(9): e0162303.
2. Schmidt MM, Wittrup KD. *A modeling analysis of the effects of molecular size and binding affinity on tumor targeting.* Mol Cancer Ther. 2009;8(10):2861-71.
3. Hollenberg NK, et al. *Senescence and the renal vasculature in normal man.* Circ Res. 1974;34(3):309-16.
4. Dearnaley D, et al. *Conventional versus hypofractionated high-dose intensity-modulated radiotherapy for prostate cancer: 5-year outcomes of the randomised, non-inferiority, phase 3 CHHiP trial.* Lancet Oncology. 2016;17(8):1047-1060.
5. Stabin MG, Sparks RB, Crowe E. *OLINDA/EXM: The Second-Generation Personal Computer Software for Internal Dose Assessment in Nuclear Medicine.* J Nucl Med. 2005;46(6):1023-1027.
6. Hindorf C, et al. *EANM Dosimetry Committee guidelines for bone marrow and whole-body dosimetry.* Eur J Nucl Med Mol Imaging. 2010;37(6):1238-1250.
7. Dale RG. *The application of the linear-quadratic dose-effect equation to fractionated and protracted radiotherapy.* Br J Radiol. 1985;58(6515-28.

A.2 Supplementary material 2

The supplementary material of the article "**Begum NJ,** Glatting G, Wester HJ, Eiber M, Beer AJ, Kletting P. The effect of ligand amount, affinity and internalization on PSMA-targeted imaging and therapy: A simulation study using a PBPK model. Sci Rep. 2019;9(1):20041. DOI: 10.1038/s41598-019-56603-8" [60] is published by Springer Nature under the terms of the Creative Commons Attribution CC BY 4.0 International license (http://creativecommons.org/licenses/by/4.0) and is copyright © 2019 by Begum NJ, Glatting G, Wester HJ, Eiber M, Beer AJ, Kletting P.

Supplemental results for manuscript:

The effect of ligand amount, affinity and internalization on PSMA-targeted imaging and therapy: A simulation study using a PBPK model

Nusrat Jihan Begum[1*], Gerhard Glatting[1,2], Hans-Jürgen Wester[3], Matthias Eiber[4], Ambros J. Beer[2], Peter Kletting[1,2]

[1]Medical Radiation Physics, Department of Nuclear Medicine, Ulm University, Ulm, Germany
[2]Department of Nuclear Medicine, Ulm University, Ulm, Germany
[3]Technical University of Munich, Pharmaceutical Radiochemistry, Munich, Germany
[4]Technical University of Munich, School of Medicine, Klinikum Rechts der Isar, Department of Nuclear Medicine, Munich, Germany

[*]**Corresponding author:**
Nusrat Jihan Begum
Medizinische Strahlenphysik, Klinik für Nuklearmedizin, Universität Ulm
D - 89081 Ulm, Germany
Tel.: +49 731 500 61372
E-mail: nusrat.begum@uni-ulm.de

Supplementary results

The effect of ligand amount, affinity and internalization on PSMA-targeted imaging and therapy: A simulation study using a PBPK model

Nusrat Jihan Begum[1*], Gerhard Glatting[1,2], Hans-Jürgen Wester[3], Matthias Eiber[4], Ambros J. Beer[2], Peter Kletting[1,2]

[1]*Medical Radiation Physics, Department of Nuclear Medicine, Ulm University, Ulm, Germany*

[2]*Department of Nuclear Medicine, Ulm University, Ulm, Germany*

[3]*Technical University of Munich, Pharmaceutical Radiochemistry, Munich, Germany*

[4]*Technical University of Munich, School of Medicine, Klinikum rechts der Isar, Department of Nuclear Medicine, Munich, Germany*

[*]**Corresponding author:**

Nusrat Jihan Begum

Medizinische Strahlenphysik, Klinik für Nuklearmedizin, Universität Ulm

D - 89081 Ulm, Germany

Tel.: +49 731 500 61372

e-mail: nusrat.begum@uni-ulm.de

K_D[a] [nM]	k_{off}[b] [1/min]	k_{on}[c] [L/nmol/min]	Amount [nmol]	λ_{int}[d]=0.01 min^{-1} Activity concentration of… [%Injected activity/l]			λ_{int}[d]=0.001 min^{-1} Activity concentration of… [%Injected activity/l]			λ_{int}[d]=0.0001 min^{-1} Activity concentration of… [%Injected activity/l]		
				Tumour 1	Tumour 2	Tumour REST	Tumour 1	Tumour 2	Tumour REST	Tumour 1	Tumour 2	Tumour REST
0.01	0.0001	0.01	1	16±10	19±15	7±5	16±10	19±15	7±5	16±10	19±15	7±5
			3	16±10	19±15	7±5	16±10	19±15	7±5	16±10	19±15	7±5
			10	16±10	19±15	7±5	16±10	19±15	7±5	16±10	19±15	7±5
			32	16±10	18±14	7±5	16±10	18±14	7±5	16±10	18±14	7±5
			100	15±10	17±12	7±5	15±9	16±12	7±5	15±9	16±12	7±5
			316	11±7	12±7	6±4	10±5	10±6	6±4	9±5	10±6	6±3
			1000	5±3	5±3	4±2	4±2	4±2	3±2	4±2	4±2	3±2
0.01	0.001	0.1	1	16±10	20±18	7±5	16±10	20±18	7±5	16±10	20±18	7±5
			3	16±11	21±18	7±6	17±11	21±18	7±6	17±11	21±18	7±6
			10	17±11	22±19	7±6	18±11	22±19	8±6	18±11	22±20	8±6
			32	19±12	23±21	8±6	19±12	23±21	8±6	19±12	23±21	8±6
			100	19±12	22±19	8±6	19±13	20±15	8±6	18±13	20±14	8±6
			316	13±8	13±9	7±4	10±6	10±6	6±4	10±5	10±6	6±4
			1000	5±3	6±3	4±2	4±2	4±2	3±2	4±2	4±2	3±2
0.1	0.001	0.01	1	16±10	19±15	7±5	16±10	19±15	7±5	16±10	19±15	7±5
			3	16±10	19±15	7±5	16±10	19±15	7±5	16±10	19±15	7±5
			10	16±10	18±15	7±5	16±10	18±15	7±5	16±10	18±15	7±5
			32	16±10	18±14	7±5	16±10	18±14	7±5	16±10	18±14	7±5
			100	15±10	17±12	7±5	15±9	16±11	7±5	15±9	16±11	7±5
			316	11±7	12±7	6±4	10±5	10±6	6±3	9±5	9±6	6±3
			1000	5±3	5±3	4±2	4±2	4±2	3±2	4±2	4±2	3±2
0.1	0.01	0.1	1	16±11	21±18	7±5	17±11	21±18	7±6	17±11	21±18	7±6
			3	17±11	21±18	7±6	17±11	21±19	7±6	17±11	21±19	7±6
			10	18±11	22±19	8±6	18±11	22±19	8±6	18±11	22±19	8±6
			32	19±12	23±20	8±6	19±12	23±20	8±6	19±12	23±20	8±6

			100	19±12	22±18	8±6	18±12	20±15	8±6	18±12	19±14	8±6
			316	13±8	13±8	7±4	10±6	10±6	6±4	10±5	10±6	6±4
			1000	5±3	6±3	4±2	4±2	4±2	3±2	4±2	4±2	3±2
1	0.01	0.01	1	15±10	18±14	7±5	15±10	17±13	7±5	15±10	17±13	7±5
			3	15±10	18±14	7±5	15±10	17±13	7±5	15±10	17±13	7±5
			10	15±10	17±13	7±5	15±9	17±13	7±5	15±9	17±13	7±5
			32	15±9	17±13	7±5	15±9	17±13	7±5	15±9	17±12	7±5
			100	14±9	16±11	7±5	14±9	15±10	7±4	14±8	15±10	7±4
			316	11±6	11±7	6±4	9±5	9±5	6±3	9±5	9±5	6±3
			1000	5±2	5±3	4±2	4±2	4±2	3±2	4±2	4±2	3±2
1	0.1	0.1	1	17±11	21±18	8±6	17±11	21±18	8±6	17±11	21±17	8±6
			3	17±11	21±18	8±6	17±11	21±18	8±6	17±11	21±17	8±6
			10	18±11	21±18	8±6	17±11	21±17	8±6	17±11	21±17	8±6
			32	18±11	21±18	8±6	17±11	20±17	8±6	17±11	20±17	8±6
			100	17±11	19±15	8±6	16±10	17±12	8±5	16±10	17±12	7±5
			316	12±7	12±8	7±4	9±5	9±5	6±4	9±5	9±5	6±4
			1000	5±3	5±3	4±2	4±2	4±2	3±2	4±2	4±2	3±2

Table S1. The average of tumour activity concentrations of ^{68}Ga-labeled PSMA-specific ligands (1 h p.i.) considering the different K_D, k_{on}, k_{off}, λ_{int} and ligand amounts. [a]K_D=Dissociation constant (K_D=k_{off}/k_{on}); [b]k_{off}=Dissociation rate; [c]k_{on}=Association rate; [d]λ_{int}=Internalization rate.

K_D[a] [nM]	k_{off}[b] [1/min]	k_{on}[c] [L/nmol/min]	Amount [nmol]	λ_{int}[d]=0.01 min^{-1} Activity concentration of… [%Injected activity/l]			λ_{int}[d]=0.001 min^{-1} Activity concentration of… [%Injected activity/l]			λ_{int}[d]=0.0001 min^{-1} Activity concentration of… [%Injected activity/l]		
				Kidneys	Liver	Red Marrow	Kidneys	Liver	Red Marrow	Kidneys	Liver	Red Marrow
0.01	0.0001	0.01	1	15±3	1.4±0.2	1.1±0.2	15±3	1.4±0.2	1.1±0.2	15±3	1.4±0.2	1.1±0.2
			3	15±3	1.4±0.2	1.1±0.2	15±3	1.4±0.2	1.1±0.2	15±3	1.4±0.2	1.1±0.2
			10	15±3	1.3±0.2	1.1±0.2	15±3	1.3±0.2	1.1±0.2	15±3	1.3±0.2	1.1±0.2
			32	14±3	1.2±0.2	1.1±0.2	13±3	1.1±0.2	1.1±0.2	13±3	1.1±0.2	1.1±0.2
			100	10±2	0.9±0.1	1.1±0.2	9±2	0.9±0.1	1.2±0.2	9±2	0.8±0.1	1.2±0.2
			316	5±1	0.7±0.1	1.2±0.2	4±1	0.7±0.1	1.2±0.2	4±1	0.7±0.1	1.2±0.2
			1000	2.6±0.4	0.7±0.1	1.2±0.2	2.2±0.3	0.6±0.1	1.2±0.2	2.2±0.3	0.6±0.1	1.2±0.2
0.01	0.001	0.1	1	24±5	6.2±0.7	0.7±0.1	24±5	6.1±0.7	0.8±0.1	24±5	6.1±0.7	0.8±0.1
			3	25±6	5.5±0.6	0.8±0.1	25±6	5.2±0.5	0.8±0.1	25±6	5.2±0.5	0.8±0.1
			10	26±6	3.7±0.3	0.9±0.2	26±6	3.2±0.2	0.9±0.2	26±6	3.1±0.2	1.0±0.2
			32	26±6	1.8±0.1	1.0±0.2	25±5	1.5±0.1	1.1±0.2	25±5	1.4±0.1	1.1±0.2
			100	15±2	1.0±0.1	1.1±0.2	11±2	0.9±0.1	1.1±0.2	11±2	0.9±0.1	1.1±0.2
			316	6±1	0.7±0.1	1.2±0.2	4±1	0.7±0.1	1.2±0.2	4±1	0.7±0.1	1.2±0.2
			1000	2.7±0.4	0.7±0.1	1.2±0.2	2.2±0.3	0.6±0.1	1.2±0.2	2.1±0.3	0.6±0.1	1.2±0.2
0.1	0.001	0.01	1	15±3	1.4±0.2	1.1±0.2	15±3	1.4±0.2	1.1±0.2	15±3	1.4±0.2	1.1±0.2
			3	15±3	1.4±0.2	1.1±0.2	15±3	1.4±0.2	1.1±0.2	15±3	1.4±0.2	1.1±0.2
			10	15±3	1.3±0.2	1.1±0.2	15±3	1.3±0.2	1.1±0.2	15±3	1.3±0.2	1.1±0.2
			32	14±3	1.2±0.2	1.1±0.2	13±3	1.1±0.2	1.1±0.2	13±3	1.1±0.2	1.1±0.2
			100	10±2	0.9±0.1	1.1±0.2	9±2	0.9±0.1	1.2±0.2	9±2	0.8±0.1	1.2±0.2
			316	5±1	0.7±0.1	1.2±0.2	4±1	0.7±0.1	1.2±0.2	4±1	0.7±0.1	1.2±0.2
			1000	2.6±0.4	0.7±0.1	1.2±0.2	2.2±0.3	0.6±0.1	1.2±0.2	2.1±0.3	0.6±0.1	1.2±0.2
0.1	0.01	0.1	1	24±5	5.2±0.6	0.8±0.1	24±5	4.9±0.6	0.8±0.1	24±5	4.9±0.6	0.8±0.1
			3	25±5	4.7±0.5	0.9±0.1	25±5	4.3±0.5	0.9±0.1	25±5	4.2±0.5	0.9±0.1
			10	26±6	3.3±0.3	0.9±0.2	26±6	2.8±0.2	1.0±0.2	26±6	2.7±0.2	1.0±0.2
			32	25±5	1.7±0.1	1.1±0.2	24±5	1.4±0.1	1.1±0.2	23±5	1.4±0.1	1.1±0.2
			100	14±2	1.0±0.1	1.1±0.2	11±2	0.9±0.1	1.1±0.2	10±2	0.8±0.1	1.1±0.2

			316	6±1	0.7±0.1	1.2±0.2	4±1	0.7±0.1	1.2±0.2	4±1	0.7±0.1	1.2±0.2
			1000	2.7±0.4	0.7±0.1	1.2±0.2	2.2±0.3	0.6±0.1	1.2±0.2	2.1±0.3	0.6±0.1	1.2±0.2
1	0.01	0.01	1	13±3	1.2±0.2	1.1±0.2	13±3	1.2±0.2	1.1±0.2	13±3	1.2±0.2	1.1±0.2
			3	13±3	1.2±0.2	1.1±0.2	13±3	1.2±0.2	1.1±0.2	13±3	1.2±0.2	1.1±0.2
			10	13±3	1.2±0.2	1.1±0.2	12±3	1.1±0.2	1.1±0.2	12±3	1.1±0.2	1.1±0.2
			32	12±3	1.1±0.2	1.1±0.2	11±2	1.0±0.2	1.1±0.2	11±2	1.0±0.2	1.1±0.2
			100	9±2	0.9±0.1	1.2±0.2	8±2	0.8±0.1	1.2±0.2	8±1	0.8±0.1	1.2±0.2
			316	5±1	0.7±0.1	1.2±0.2	4±1	0.7±0.1	1.2±0.2	4±1	0.7±0.1	1.2±0.2
			1000	2.6±0.4	0.7±0.1	1.2±0.2	2.2±0.3	0.6±0.1	1.3±0.2	2.1±0.3	0.6±0.1	1.3±0.2
1	0.1	0.1	1	21±4	2.1±0.3	1.0±0.2	20±4	1.7±0.3	1.1±0.2	20±4	1.6±0.3	1.1±0.2
			3	21±4	2.0±0.3	1.1±0.2	20±4	1.6±0.3	1.1±0.2	20±4	1.5±0.3	1.1±0.2
			10	20±4	1.7±0.2	1.1±0.2	19±4	1.4±0.2	1.1±0.2	19±4	1.3±0.2	1.1±0.2
			32	18±4	1.3±0.2	1.1±0.2	16±3	1.1±0.2	1.1±0.2	15±3	1.1±0.2	1.1±0.2
			100	12±2	0.9±0.1	1.1±0.2	9±2	0.8±0.1	1.1±0.2	8±2	0.8±0.1	1.2±0.2
			316	5±1	0.7±0.1	1.2±0.2	4±1	0.7±0.1	1.2±0.2	4±1	0.7±0.1	1.2±0.2
			1000	2.6±0.4	0.7±0.1	1.2±0.2	2.2±0.3	0.6±0.1	1.2±0.2	2.1±0.3	0.6±0.1	1.2±0.2

Table S2. The average of kidneys, liver and red marrow activity concentrations of ^{68}Ga-labeled PSMA-specific ligands (1 h p.i.) considering the different K_D, k_{on}, k_{off}, λ_{int} and ligand amounts. [a]K_D=Dissociation constant ($K_D=k_{off}/k_{on}$); [b]k_{off} =Dissociation rate; [c]k_{on}=Association rate; [d]λ_{int}=Internalization rate.

K_D[a] [nM]	k_{off}[b] [1/min]	k_{on}[c] [L/nmol /min]	Amount [nmol]	λ_{int}[d]=0.01 min^{-1} Activity concentration of… [%Injected activity/l]			λ_{int}[d]=0.001 min^{-1} Activity concentration of… [%Injected activity/l]			λ_{int}[d]=0.0001 min^{-1} Activity concentration of… [%Injected activity/l]		
				Background	GI	Lung	Background	GI	Lung	Background	GI	Lung
0.01	0.0001	0.01	1	0.28±0.04	2.8±0.4	4±1	0.28±0.04	2.8±0.4	4±1	0.28±0.04	2.8±0.4	4±1
			3	0.28±0.04	2.8±0.4	4±1	0.28±0.04	2.8±0.4	4±1	0.28±0.04	2.8±0.4	4±1
			10	0.28±0.04	2.8±0.4	4±1	0.28±0.04	2.8±0.4	4±1	0.28±0.04	2.8±0.4	4±1
			32	0.28±0.04	2.8±0.4	4±1	0.28±0.04	2.8±0.4	4±1	0.28±0.04	2.8±0.4	4±1
			100	0.29±0.05	2.8±0.4	4±1	0.29±0.05	2.8±0.4	4±1	0.29±0.05	2.8±0.4	4±1
			316	0.30±0.05	2.9±0.4	5±1	0.30±0.05	2.9±0.4	5±1	0.30±0.05	2.9±0.4	5±1
			1000	0.31±0.05	2.9±0.4	5±1	0.31±0.05	2.9±0.4	5±1	0.31±0.05	2.9±0.4	5±1
0.01	0.001	0.1	1	0.20±0.03	2.5±0.3	2.8±0.4	0.20±0.03	2.5±0.3	2.8±0.4	0.20±0.03	2.5±0.3	2.8±0.4
			3	0.21±0.03	2.6±0.3	3.0±0.5	0.21±0.03	2.6±0.3	3.0±0.5	0.21±0.03	2.6±0.3	3±1
			10	0.23±0.04	2.7±0.4	3±1	0.24±0.04	2.8±0.4	4±1	0.24±0.04	2.8±0.4	4±1
			32	0.26±0.04	2.9±0.4	4±1	0.27±0.04	2.9±0.4	4±1	0.27±0.04	2.9±0.4	4±1
			100	0.28±0.05	2.9±0.4	4±1	0.28±0.05	2.9±0.4	4±1	0.28±0.05	2.9±0.4	4±1
			316	0.29±0.05	2.9±0.4	4±1	0.30±0.05	2.9±0.4	5±1	0.30±0.05	2.9±0.4	5±1
			1000	0.30±0.05	2.9±0.4	5±1	0.31±0.05	2.9±0.4	5±1	0.31±0.05	2.9±0.4	5±1
0.1	0.001	0.01	1	0.28±0.04	2.8±0.4	4±1	0.28±0.04	2.8±0.4	4±1	0.28±0.04	2.8±0.4	4±1
			3	0.28±0.04	2.8±0.4	4±1	0.28±0.04	2.8±0.4	4±1	0.28±0.04	2.8±0.4	4±1
			10	0.28±0.04	2.8±0.4	4±1	0.28±0.04	2.8±0.4	4±1	0.28±0.04	2.8±0.4	4±1
			32	0.28±0.04	2.8±0.4	4±1	0.28±0.04	2.8±0.4	4±1	0.28±0.04	2.8±0.4	4±1
			100	0.29±0.05	2.8±0.4	4±1	0.29±0.05	2.8±0.4	4±1	0.29±0.05	2.8±0.4	4±1
			316	0.30±0.05	2.9±0.4	5±1	0.30±0.05	2.9±0.4	5±1	0.30±0.05	2.9±0.4	5±1
			1000	0.31±0.05	2.9±0.4	5±1	0.31±0.05	2.9±0.4	5±1	0.31±0.05	2.9±0.4	5±1
0.1	0.01	0.1	1	0.21±0.03	2.6±0.3	3.1±0.5	0.22±0.03	2.6±0.3	3.2±0.5	0.22±0.03	2.6±0.3	3.2±0.5
			3	0.22±0.03	2.6±0.4	3±1	0.23±0.03	2.6±0.4	3±1	0.23±0.03	2.6±0.4	3±1
			10	0.24±0.04	2.7±0.4	4±1	0.25±0.04	2.8±0.4	4±1	0.25±0.04	2.8±0.4	4±1
			32	0.27±0.04	2.9±0.4	4±1	0.27±0.04	2.9±0.4	4±1	0.27±0.04	2.9±0.4	4±1
			100	0.28±0.05	2.9±0.4	4±1	0.28±0.05	2.9±0.4	4±1	0.28±0.05	2.9±0.4	4±1
			316	0.29±0.05	2.9±0.4	4±1	0.30±0.05	2.9±0.4	5±1	0.30±0.05	2.9±0.4	5±1

			1000	0.30±0.05	2.9±0.4	5±1	0.31±0.05	2.9±0.4	5±1	0.31±0.05	2.9±0.4	5±1
1	0.01	0.01	1	0.28±0.04	2.8±0.4	4±1	0.28±0.04	2.8±0.4	4±1	0.28±0.04	2.8±0.4	4±1
			3	0.28±0.04	2.8±0.4	4±1	0.28±0.04	2.8±0.4	4±1	0.28±0.04	2.8±0.4	4±1
			10	0.28±0.04	2.8±0.4	4±1	0.28±0.04	2.8±0.4	4±1	0.28±0.04	2.8±0.4	4±1
			32	0.29±0.04	2.8±0.4	4±1	0.29±0.04	2.8±0.4	4±1	0.29±0.04	2.8±0.4	4±1
			100	0.29±0.05	2.8±0.4	4±1	0.29±0.05	2.8±0.4	4±1	0.29±0.05	2.8±0.4	4±1
			316	0.30±0.05	2.9±0.4	5±1	0.30±0.05	2.9±0.4	5±1	0.30±0.05	2.9±0.4	5±1
			1000	0.31±0.05	2.9±0.4	5±1	0.31±0.05	2.9±0.4	5±1	0.31±0.05	2.9±0.4	5±1
1	0.1	0.1	1	0.26±0.04	2.7±0.4	4±1	0.27±0.04	2.8±0.4	4±1	0.27±0.04	2.8±0.4	4±1
			3	0.27±0.04	2.8±0.4	4±1	0.27±0.04	2.8±0.4	4±1	0.27±0.04	2.8±0.4	4±1
			10	0.27±0.04	2.8±0.4	4±1	0.28±0.04	2.8±0.4	4±1	0.28±0.04	2.8±0.4	4±1
			32	0.28±0.04	2.8±0.4	4±1	0.28±0.04	2.8±0.4	4±1	0.28±0.04	2.8±0.4	4±1
			100	0.28±0.05	2.8±0.4	4±1	0.29±0.05	2.8±0.4	4±1	0.29±0.05	2.8±0.4	4±1
			316	0.29±0.05	2.9±0.4	5±1	0.30±0.05	2.9±0.4	5±1	0.30±0.05	2.9±0.4	5±1
			1000	0.31±0.05	2.9±0.4	5±1	0.31±0.05	2.9±0.4	5±1	0.31±0.05	2.9±0.4	5±1

Table S3. The average of background, gastro intestinal (GI) and lung activity concentrations of ^{68}Ga-labeled PSMA-specific ligands (1 h p.i.) considering the different K_D, k_{on}, k_{off}, λ_{int} and ligand amounts. [a]K_D=Dissociation constant (K_D=k_{off}/k_{on}); [b]k_{off}=Dissociation rate; [c]k_{on}=Association rate; [d]λ_{int}=Internalization rate.

Decreasing K_D[a] from… [nM]	k_{off}[b] [min^{-1}]	k_{on}[c] [L/nmol/min]	Amount [nmol]	The ratio of the normalized activity concentrations of…	
				Tumour 1 and 2	Tumour REST
1 to 0.1	0.1 to 0.01	fixed (0.1)	3	1.0±0.1	0.94±0.04
			10	1.0±0.1	0.98±0.04
			32	1.1±0.1	1.0±0.1
1 to 0.01	0.1 to 0.001	fixed (0.1)	3	1.0±0.1	0.92±0.04
			10	1.0±0.1	0.97±0.05
			32	1.1±0.1	1.0±0.1
1 to 0.1	0.01 to 0.001	fixed (0.01)	3	1.06±0.03	1.03±0.03
			10	1.06±0.03	1.03±0.03
			32	1.06±0.04	1.03±0.03
1 to 0.01	0.01 to 0.0001	fixed (0.01)	3	1.06±0.04	1.03±0.03
			10	1.07±0.04	1.03±0.03
			32	1.07±0.04	1.04±0.03
1 to 0.1	fixed (0.01)	0.01 to 0.1	3	1.2±0.3	1.0±0.1
			10	1.2±0.3	1.1±0.1
			32	1.3±0.2	1.1±0.2
0.1 to 0.01	fixed (0.001)	0.01 to 0.1	3	1.1±0.2	1.0±0.1
			10	1.2±0.3	1.0±0.1
			32	1.2±0.2	1.1±0.1

Table S4. The ratio of the normalized activity concentrations in tumour by decreasing K_D by changing k_{off} or k_{on}. [a]K_D=Dissociation constant ($K_D=k_{off}/k_{on}$); [b]k_{off}=Dissociation rate; [c]k_{on}=Association rate.

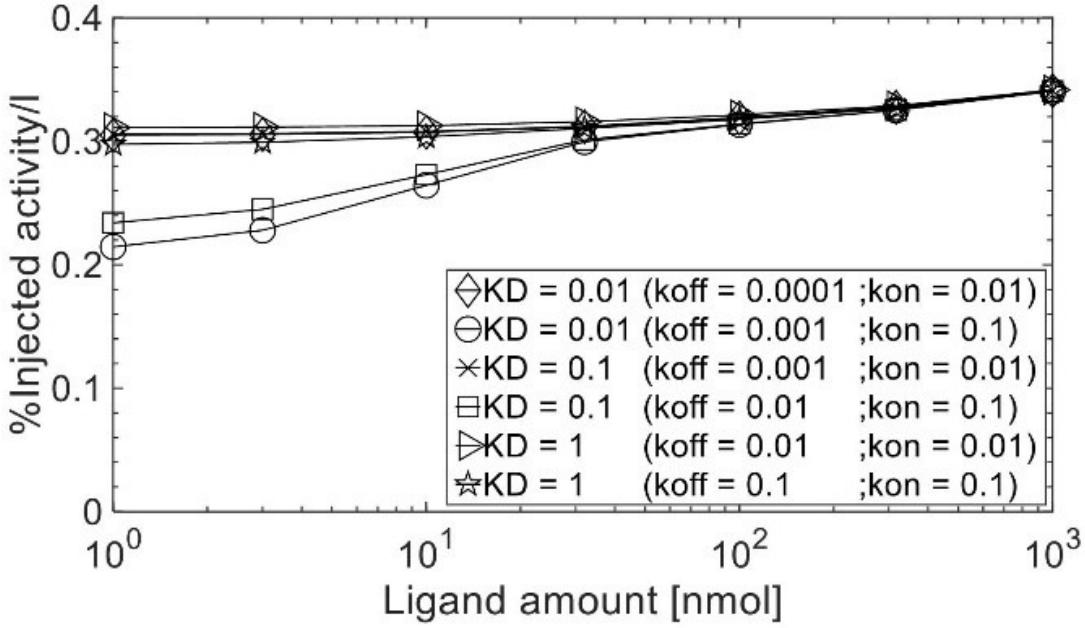

Figure S1. Normalized activity concentrations for ^{68}Ga-labeled (1 h p.i.) PSMA-specific ligands for background (muscle and fat) of patient 5.

K_D[a] [nM]	k_{off}[b] [1/min]	k_{on}[c] [L/nmol /min]	Amount [nmol]	λ_{int}[d]=0.01 min^{-1} Absorbed dose of… [Gy]			λ_{int}[d]=0.001 min^{-1} Absorbed dose of… [Gy]			λ_{int}[d]=0.0001 min^{-1} Absorbed dose of… [Gy]		
				Tumour 1	Tumour 2	Tumour REST	Tumour 1	Tumour 2	Tumour REST	Tumour 1	Tumour 2	Tumour REST
0.01	0.0001	0.01	1	37±20	44±32	29±20	42±23	50±35	34±23	65±37	74±52	55±37
			3	37±20	44±32	29±20	43±23	50±35	34±23	65±37	74±51	55±37
			10	38±20	44±32	30±20	43±23	50±35	35±23	64±37	72±49	55±37
			32	38±21	45±32	30±20	42±24	47±32	35±22	57±35	61±40	54±33
			100	38±21	43±30	31±20	31±19	33±23	32±19	33±21	34±23	40±24
			316	30±18	33±22	29±17	15±10	16±11	19±12	13±8	13±9	17±10
			1000	17±11	19±13	20±13	6±4	7±5	8±5	4±3	5±3	6±3
0.01	0.001	0.1	1	30±16	38±30	22±17	45±23	55±42	33±25	75±42	89±67	60±45
			3	31±17	39±31	23±18	46±24	56±43	34±25	76±42	89±66	61±45
			10	34±18	43±33	25±19	49±25	59±45	37±27	75±43	85±60	61±44
			32	39±20	48±38	29±22	49±28	56±40	39±27	63±41	64±43	58±36
			100	43±23	50±37	33±23	34±22	37±26	35±20	32±21	34±22	40±25
			316	34±20	38±26	32±19	16±10	17±12	20±13	12±8	13±8	17±10
			1000	19±12	21±14	22±13	6±4	7±5	8±5	4±3	5±3	6±3
0.1	0.001	0.01	1	37±20	44±32	29±20	40±22	45±31	33±21	41±25	44±27	41±24
			3	37±20	44±32	29±20	40±22	45±31	33±21	41±24	44±27	41±24
			10	38±20	44±32	30±20	39±22	44±30	33±21	39±24	41±25	40±23
			32	38±21	44±31	30±20	37±22	41±27	33±20	33±21	34±21	37±21
			100	37±21	42±29	31±20	27±17	29±20	29±17	19±13	20±14	26±16
			316	30±18	32±22	29±17	14±9	15±10	17±11	8±5	9±6	12±7
			1000	17±11	19±13	20±12	6±4	6±4	8±5	3±2	3±2	4±3
0.1	0.01	0.1	1	33±18	41±32	25±19	44±24	51±37	35±24	44±26	47±29	43±25
			3	34±18	42±33	25±19	44±24	51±36	35±24	43±26	46±28	43±25
			10	36±19	45±35	27±20	44±24	51±36	36±24	41±25	43±26	42±24
			32	40±21	49±37	30±22	42±24	45±31	36±22	33±21	33±22	38±22

			100	43±23	49±36	33±23	29±19	31±21	31±19	19±13	19±14	26±17
			316	34±20	37±26	31±19	14±9	15±10	18±12	8±5	8±6	12±7
			1000	19±12	21±14	21±13	6±4	6±4	8±5	3±2	3±2	4±3
1	0.01	0.01	1	35±19	41±28	29±19	22±14	24±15	23±13	10±6	11±7	13±7
			3	35±19	41±28	29±19	22±13	23±15	23±13	10±6	11±7	13±7
			10	35±19	40±28	29±19	21±13	23±15	22±13	10±6	10±6	13±7
			32	35±19	40±27	29±18	20±12	21±14	22±13	9±6	9±6	11±7
			100	33±19	37±25	29±18	15±10	16±11	19±12	6±4	7±4	9±5
			316	27±16	29±20	27±16	9±6	10±7	12±8	3±2	4±2	5±3
			1000	16±11	18±12	19±12	4±3	5±3	6±4	2±1	2±1	2±1
1	0.1	0.1	1	37±20	44±32	30±20	23±14	25±16	24±14	10±6	11±7	13±7
			3	37±20	44±32	30±20	23±14	25±16	24±14	10±6	11±7	13±7
			10	38±20	44±32	30±20	22±14	24±15	23±14	10±6	10±6	13±7
			32	38±21	44±32	31±20	20±13	22±14	22±13	9±6	9±6	11±7
			100	37±21	42±29	31±19	15±10	16±11	19±12	6±4	6±4	9±5
			316	29±18	32±22	29±17	9±6	10±7	12±8	3±2	4±2	5±3
			1000	17±11	19±13	20±12	4±3	5±3	6±4	1±1	2±1	2±1

Table S5. The average of tumour absorbed doses of ^{177}Lu-labeled PSMA-specific ligands considering the different K_D, k_{off}, k_{on}, λ_{int} and ligand amounts. [a]K_D=Dissociation constant (K_D=k_{off}/k_{on}); [b]k_{off}=Dissociation rate; [c]k_{on}=Association rate; [d]λ_{int}=Internalization rate.

K_D[a] [nM]	k_{off}[b] [1/min]	k_{on}[c] [L/nmol/min]	Amount [nmol]	λ_{int}[d]=0.01 min^{-1} Absorbed dose of… [Gy]		λ_{int}[d]=0.001 min^{-1} Absorbed dose of… [Gy]		λ_{int}[d]=0.0001 min^{-1} Absorbed dose of… [Gy]	
				Kidneys	Red Marrow	Kidneys	Red Marrow	Kidneys	Red Marrow
0.01	0.0001	0.01	1	28±7	0.13±0.04	31±8	0.14±0.05	48±14	0.19±0.06
			3	28±7	0.13±0.04	30±8	0.14±0.05	46±14	0.19±0.06
			10	27±7	0.13±0.04	28±7	0.14±0.05	41±11	0.18±0.06
			32	26±7	0.13±0.04	21±5	0.14±0.05	26±5	0.17±0.07
			100	20±6	0.13±0.05	11±2	0.13±0.05	11±2	0.15±0.07
			316	12±3	0.12±0.05	5±1	0.12±0.05	4±1	0.13±0.07
			1000	6.0±1.8	0.12±0.05	2.0±0.5	0.11±0.04	1.6±0.3	0.11±0.05
0.01	0.001	0.1	1	35±8	0.12±0.04	49±12	0.15±0.04	63±17	0.20±0.06
			3	36±8	0.12±0.04	48±12	0.15±0.04	58±15	0.20±0.06
			10	39±9	0.12±0.04	43±10	0.15±0.04	43±10	0.19±0.06
			32	40±9	0.13±0.04	26±6	0.14±0.05	23±5	0.17±0.07
			100	28±7	0.13±0.04	12±3	0.13±0.05	10±2	0.15±0.07
			316	15±4	0.13±0.05	5±1	0.12±0.05	4±1	0.13±0.07
			1000	7.1±2.0	0.12±0.05	2±1	0.11±0.05	1.5±0.3	0.11±0.05
0.1	0.001	0.01	1	27±7	0.13±0.04	24±7	0.14±0.05	19±6	0.16±0.07
			3	27±7	0.13±0.04	23±7	0.14±0.05	18±6	0.16±0.07
			10	27±7	0.13±0.04	21±6	0.13±0.05	16±5	0.16±0.07
			32	25±7	0.13±0.04	16±4	0.13±0.05	11±3	0.15±0.07
			100	19±6	0.13±0.05	9±2	0.13±0.05	6±2	0.14±0.07
			316	12±3	0.12±0.05	4±1	0.12±0.05	3±1	0.12±0.07
			1000	6.0±1.8	0.12±0.05	1.8±0.5	0.11±0.04	1.0±0.3	0.11±0.04
0.1	0.01	0.1	1	36±8	0.12±0.04	30±9	0.14±0.05	19±6	0.16±0.07
			3	37±8	0.12±0.04	29±8	0.14±0.05	18±6	0.16±0.07
			10	38±9	0.13±0.04	25±7	0.14±0.05	15±5	0.16±0.07
			32	37±9	0.13±0.04	17±5	0.13±0.05	10±3	0.15±0.07
			100	27±7	0.13±0.04	9±2	0.13±0.05	5±2	0.14±0.07
			316	14±4	0.13±0.05	4±1	0.12±0.05	2±1	0.12±0.07

			1000	6.9±2.0	0.12±0.05	2±1	0.11±0.04	1.0±0.3	0.11±0.04
1	0.01	0.01	1	21±6	0.13±0.05	8±3	0.12±0.05	4±1	0.12±0.05
			3	21±6	0.13±0.05	8±3	0.12±0.05	3±1	0.12±0.05
			10	20±6	0.13±0.05	7±3	0.12±0.05	3±1	0.12±0.05
			32	19±6	0.13±0.05	6±2	0.12±0.05	3±1	0.12±0.05
			100	16±5	0.13±0.05	5±1	0.12±0.05	2±1	0.11±0.05
			316	10±3	0.12±0.05	3±1	0.11±0.05	1.1±0.4	0.11±0.05
			1000	5.4±1.7	0.12±0.05	1.3±0.4	0.11±0.04	0.6±0.2	0.10±0.04
1	0.1	0.1	1	27±7	0.13±0.04	8±3	0.12±0.05	4±1	0.12±0.05
			3	27±7	0.13±0.04	8±3	0.12±0.05	3±1	0.12±0.05
			10	26±7	0.13±0.04	8±3	0.12±0.05	3±1	0.12±0.05
			32	24±7	0.13±0.04	6±2	0.12±0.05	3±1	0.12±0.05
			100	19±6	0.13±0.05	5±1	0.12±0.05	2±1	0.11±0.05
			316	11±3	0.12±0.05	3±1	0.11±0.05	1.1±0.4	0.11±0.05
			1000	5.8±1.8	0.12±0.05	1.3±0.4	0.11±0.04	0.6±0.2	0.10±0.04

Table S6. The average of kidneys and red marrow absorbed doses of ^{177}Lu-labeled PSMA-specific ligands considering the different K_D, k_{off}, k_{on}, λ_{int} and ligand amounts. [a]K_D=Dissociation constant (K_D=k_{off}/k_{on}); [b]k_{off}=Dissociation rate; [c]k_{on}=Association rate; [d]λ_{int}=Internalization rate.

K_D[a] [nM]	k_{off}[b] [1/min]	k_{on}[c] [L/nmol/min]	Amount [nmol]	λ_{int}[d]=0.01 min^{-1} Ratio of absorbed dose of…			λ_{int}[d]=0.001 min^{-1} Ratio of absorbed dose of…			λ_{int}[d]=0.0001 min^{-1} Ratio of absorbed dose of…		
				Tumour 1 /Kidneys	Tumour 2 /Kidneys	Tumour REST /Kidneys	Tumour 1 /Kidneys	Tumour 2 /Kidneys	Tumour REST /Kidneys	Tumour 1 /Kidneys	Tumour 2 /Kidneys	Tumour REST /Kidneys
0.01	0.0001	0.01	1	1.4±1.0	1.7±1.3	1.1±0.9	1.5±1.0	1.7±1.4	1.2±0.9	1.5±1.0	1.7±1.3	1.2±1.0
			3	1.4±1.0	1.7±1.4	1.1±0.9	1.5±1.0	1.8±1.4	1.2±1.0	1.5±1.1	1.7±1.3	1.3±1.0
			10	1.5±1.0	1.7±1.4	1.2±0.9	1.6±1.1	1.9±1.5	1.3±1.1	1.7±1.2	1.9±1.5	1.5±1.1
			32	1.6±1.1	1.9±1.5	1.3±1.0	2.1±1.5	2.4±1.9	1.8±1.4	2.4±1.7	2.5±1.9	2.2±1.6
			100	2.1±1.5	2.3±1.9	1.7±1.4	3.0±2.2	3.2±2.5	3.1±2.2	3.0±2.1	3.2±2.3	3.7±2.6
			316	2.7±1.9	3.0±2.3	2.7±2.0	3.3±2.3	3.6±2.6	4.2±2.8	3.1±2.1	3.3±2.3	4.2±2.6
			1000	3.1±2.2	3.4±2.5	3.6±2.5	3.3±2.2	3.5±2.6	4.3±2.8	2.9±1.9	3.1±2.2	4.0±2.5
0.01	0.001	0.1	1	0.9±0.5	1.1±0.8	0.6±0.5	1.0±0.6	1.2±0.9	0.7±0.6	1.3±0.9	1.5±1.3	1.0±0.9
			3	0.9±0.5	1.1±0.8	0.6±0.5	1.0±0.6	1.2±1.0	0.7±0.6	1.4±1.0	1.7±1.4	1.1±1.0
			10	0.9±0.6	1.1±0.9	0.7±0.5	1.2±0.8	1.5±1.3	0.9±0.8	1.9±1.4	2.2±1.8	1.6±1.4
			32	1.0±0.7	1.3±1.0	0.8±0.6	2.0±1.5	2.3±1.9	1.6±1.4	3.0±2.4	3.0±2.4	2.7±2.1
			100	1.7±1.2	1.9±1.6	1.3±1.1	3.0±2.2	3.2±2.6	3.1±2.2	3.4±2.3	3.5±2.6	4.2±3.0
			316	2.5±1.7	2.7±2.1	2.3±1.7	3.3±2.3	3.5±2.6	4.1±2.8	3.3±2.2	3.5±2.5	4.6±2.9
			1000	2.9±2.0	3.2±2.4	3.3±2.3	3.2±2.2	3.5±2.5	4.3±2.7	3.1±2.1	3.2±2.3	4.3±2.7
0.1	0.001	0.01	1	1.5±1.0	1.7±1.4	1.2±0.9	1.8±1.3	2.1±1.6	1.6±1.2	2.4±1.7	2.6±1.9	2.4±1.7
			3	1.5±1.0	1.7±1.4	1.2±0.9	1.9±1.3	2.1±1.7	1.6±1.2	2.5±1.7	2.7±1.9	2.5±1.8
			10	1.5±1.0	1.8±1.4	1.2±1.0	2.0±1.4	2.3±1.8	1.7±1.3	2.7±1.9	2.8±2.1	2.8±1.9
			32	1.7±1.1	1.9±1.6	1.4±1.1	2.5±1.8	2.7±2.1	2.3±1.7	3.2±2.2	3.3±2.4	3.6±2.4
			100	2.1±1.5	2.3±1.9	1.8±1.4	3.3±2.3	3.5±2.7	3.5±2.5	3.5±2.4	3.6±2.6	4.7±3.1
			316	2.8±1.9	3.0±2.3	2.7±2.0	3.5±2.4	3.8±2.8	4.5±3.0	3.3±2.2	3.5±2.5	4.8±3.0
			1000	3.1±2.2	3.4±2.5	3.6±2.5	3.4±2.3	3.6±2.6	4.5±2.9	3.0±2.0	3.2±2.2	4.4±2.7
0.1	0.01	0.1	1	1.0±0.6	1.2±0.9	0.7±0.5	1.6±1.1	1.8±1.5	1.3±1.0	2.6±1.9	2.8±2.1	2.6±1.9
			3	1.0±0.6	1.2±0.9	0.7±0.6	1.6±1.1	1.9±1.6	1.3±1.1	2.7±1.9	2.9±2.2	2.7±2.0
			10	1.0±0.6	1.2±0.9	0.7±0.6	1.9±1.4	2.2±1.8	1.6±1.3	3.1±2.2	3.2±2.4	3.2±2.3

			32	1.1±0.7	1.4±1.1	0.9±0.7	2.7±2.0	2.9±2.3	2.3±1.8	3.6±2.6	3.7±2.8	4.2±2.9
			100	1.7±1.2	2.0±1.7	1.4±1.2	3.4±2.5	3.6±2.8	3.7±2.7	3.7±2.5	3.8±2.8	5.1±3.3
			316	2.5±1.8	2.8±2.2	2.4±1.8	3.6±2.5	3.8±2.8	4.6±3.1	3.4±2.3	3.5±2.5	5.0±3.1
			1000	3.0±2.0	3.2±2.4	3.4±2.3	3.4±2.3	3.7±2.7	4.6±3.0	3.1±2.0	3.2±2.2	4.5±2.7
1	0.01	0.01	1	1.8±1.3	2.1±1.7	1.5±1.2	3.0±2.1	3.2±2.4	3.1±2.2	3.1±2.1	3.3±2.3	3.9±2.5
			3	1.8±1.3	2.1±1.7	1.5±1.2	3.0±2.1	3.3±2.4	3.2±2.2	3.1±2.1	3.3±2.3	4.0±2.5
			10	1.9±1.3	2.1±1.7	1.6±1.2	3.1±2.1	3.3±2.5	3.3±2.3	3.2±2.1	3.3±2.3	4.1±2.5
			32	2.0±1.4	2.3±1.8	1.7±1.3	3.3±2.3	3.5±2.6	3.7±2.5	3.2±2.2	3.4±2.4	4.3±2.7
			100	2.4±1.7	2.6±2.1	2.1±1.6	3.6±2.5	3.8±2.8	4.4±3.0	3.2±2.2	3.4±2.4	4.6±2.9
			316	2.9±2.0	3.2±2.4	3.0±2.1	3.6±2.5	3.9±2.8	4.9±3.2	3.0±2.0	3.2±2.2	4.4±2.7
			1000	3.3±2.3	3.5±2.6	3.8±2.6	3.4±2.3	3.7±2.6	4.7±3.0	2.6±1.6	2.7±1.8	3.7±2.2
1	0.1	0.1	1	1.5±1.0	1.7±1.4	1.2±0.9	3.0±2.1	3.2±2.4	3.1±2.2	3.1±2.1	3.3±2.3	4.0±2.5
			3	1.5±1.0	1.7±1.4	1.2±0.9	3.0±2.1	3.3±2.5	3.2±2.2	3.1±2.1	3.3±2.3	4.0±2.5
			10	1.6±1.1	1.8±1.5	1.2±1.0	3.1±2.2	3.4±2.5	3.3±2.3	3.2±2.2	3.4±2.4	4.2±2.6
			32	1.7±1.2	2.0±1.6	1.4±1.1	3.4±2.3	3.6±2.7	3.7±2.6	3.3±2.2	3.4±2.4	4.4±2.8
			100	2.2±1.6	2.4±2.0	1.9±1.5	3.6±2.5	3.9±2.9	4.5±3.1	3.3±2.2	3.4±2.4	4.7±2.9
			316	2.8±2.0	3.1±2.4	2.8±2.0	3.6±2.5	3.9±2.9	4.9±3.2	3.0±2.0	3.2±2.2	4.4±2.7
			1000	3.2±2.2	3.5±2.6	3.7±2.5	3.4±2.3	3.7±2.7	4.7±3.0	2.6±1.6	2.7±1.8	3.7±2.2

Table S7. The average of tumour-to-kidneys absorbed doses of ^{177}Lu-labeled PSMA-specific ligands considering the different K_D, k_{off}, k_{on}, λ_{int} and ligand amounts. [a]K_D=Dissociation constant (K_D=k_{off}/k_{on}); [b]k_{off}=Dissociation rate; [c]k_{on}=Association rate; [d]λ_{int}=Internalization rate.

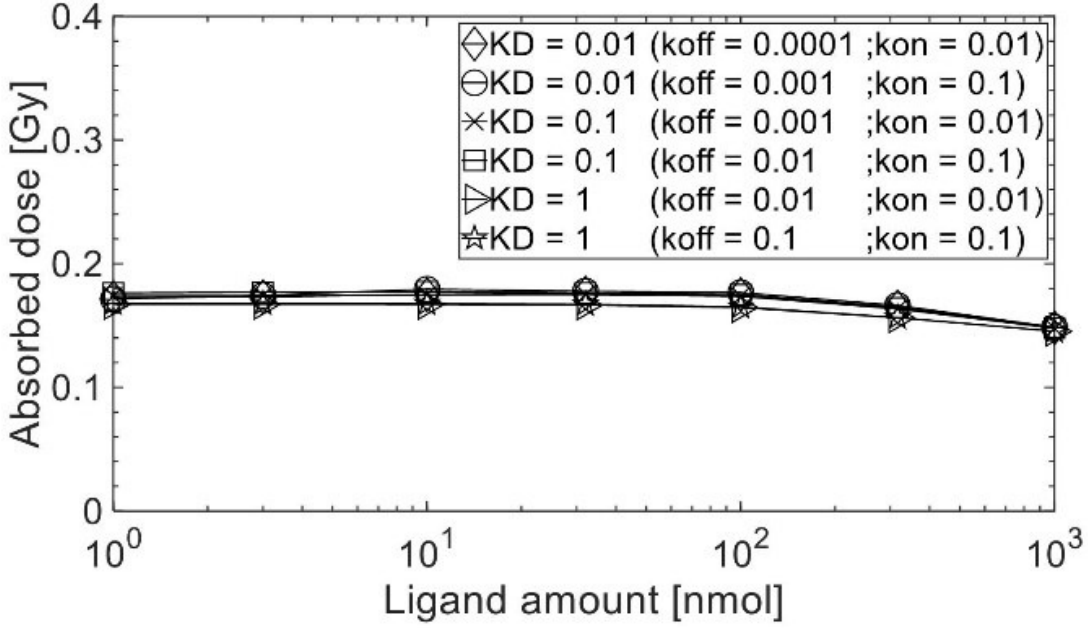

Figure S2. The absorbed dose for ^{177}Lu 7.3 GBq in red marrow (no PSMA expression) of patient 5.

Acknowledgments

The content of this page has been removed for privacy reasons.

Curriculum Vitae

The content of this page has been removed for privacy reasons.